Advanced Techniques for Rapid High-Resolution First-Pass CMR Perfusion with Whole-Heart Coverage

---

A

Thesis

Presented to

the faculty of the School of Engineering and Applied Science

University of Virginia

---

in partial fulfillment

of the requirements for the degree

Doctor of Philosophy

by

Junyu Wang

December 2022

APPROVAL SHEET

This

Thesis

is submitted in partial fulfillment of the requirements
for the degree of

Doctor of Philosophy

Author: Junyu Wang

This Thesis has been read and approved by the examing committee:

Advisor: Michael Salerno

Advisor:

Committee Member: Craig H. Meyer

Committee Member: Frederick H. Epstein

Committee Member: John P. Mugler III

Committee Member: Christopher M. Kramer

Committee Member:

Committee Member:

Accepted for the School of Engineering and Applied Science:

Jennifer L. West, School of Engineering and Applied Science

December 2022

Dedicated to the ones I love, who have unconditionally supported me throughout my graduate studies

My parents - Chenglong Wang & Liqin Wu

My sister - Danyu Wang

Abstract

Coronary artery disease (CAD) is a major public health concern. According to a report from the AHA in 2020, an estimated 18.2 million adult Americans have CAD[1]. CAD is responsible for 1 in every 7 deaths in the United States[2]. Cardiac magnetic resonance (CMR) quantitative myocardial first-pass perfusion imaging is a non-invasive and non-ionizing technique for diagnosing CAD which provides an accurate assessment of myocardial ischemia and a comprehensive evaluation of myocardial function and infarction[3–6].

Despite multiple potential advantages of CMR perfusion imaging, current clinically available techniques have limited in-plane spatial resolution (~2-3 mm) and incomplete heart coverage, which impede the assessment of transmural perfusion differences and underestimate the extent of ischemia. Furthermore, motion-induced dark-rim artifacts can significantly reduce image quality and limit evaluation of the sub-endocardium, which is most sensitive to myocardial ischemia[7]. Recently, studies from our lab have demonstrated CMR quantitative spiral perfusion techniques for both interleaved single-slice (SS) and simultaneous multi-slice (SMS) acquisitions enabling whole-heart coverage (6-8 slices) with high spatial resolution (2×2 mm^2)[8,9]. Our lab has developed novel motion-compensated compressed-sensing (CS) L1-SPIRiT reconstruction techniques, that correct for breathing motion and enable free-breathing acquisition[8]. Sampling efficiency can also be improved by using outer-volume suppression (OVS) technique to achieve a reduced field-of-view (rFOV) so that the sampling in k-space can be coarser[10]. We have previously applied an OVS technique for single-shot spiral perfusion imaging and demonstrated that it produced superior image quality as compared with full-FOV acquisitions[11]. We have also developed a quantification pipeline for spiral perfusion imaging to quantify myocardial blood flow and myocardial perfusion reserve (MPR). High diagnostic accuracy of the proposed techniques has been demonstrated[12–14].

With higher spatial resolution, there is an increased ability to detect transmural perfusion differences between the epicardium and the endocardium, which could improve the ability to detecting obstructive CAD as demonstrated in prior studies[15–18]. Additionally, one significant barrier to clinical translation of these techniques is the need for off-line reconstruction and quantification which currently takes hours to complete, and thus cannot provide data to physician in a clinically acceptable time frame. Considering that greater than 10 million stress

tests are performed in the US alone, improvements in the accuracy of non-invasive assessment of CAD could significantly reduce health care costs resulting from incorrect diagnoses. In this dissertation, we propose to develop advanced rapid and high-resolution imaging techniques for first-pass myocardial perfusion with whole-heart coverage.

Specific Aim #1 is to develop high spatial resolution spiral first-pass myocardial perfusion imaging with whole-heart coverage at 3 T. (a) Optimize spiral perfusion pulse sequences for both SS and SMS acquisitions with or without OVS to address the higher undersampling factors required to achieve 1.25×1.25 mm^2 spatial resolution with high temporal resolution and whole-heart coverage. (b) Optimize the motion-compensated L1-SPIRiT image reconstruction technique and develop the motion-compensated SMS-Slice-L1-SPIRiT reconstruction technique that incorporates through-plane kernels for spiral SMS imaging that could reduce the slice leakage and improve image quality. (c) Evaluate image quality of the proposed technique in both healthy volunteers and patients undergoing clinically ordered CMR studies.

Specific Aim #2 is to develop DEep learning-based rapid Spiral Image REconstruction (DESIRE) for high-resolution spiral first-pass myocardial perfusion imaging for both 3 T and 1.5 T. (a) Develop a DEep learning-based rapid Spiral Image REconstruction technique (DESIRE) for high-resolution spiral first-pass myocardial perfusion imaging for both SS and SMS MB=2 acquisitions with whole-heart coverage. (b) Assess the image reconstruction network performance with varying factors including data type, convolutional units, etc. (c) Validate the proposed technique in both healthy volunteers and patients as compared to the CS-based L1-SPIRiT reconstructions.

Specific Aim #3 is to develop quantitative perfusion imaging with Cartesian acquisition and compare it to spiral perfusion imaging. (a) Develop the 2D and SMS Cartesian perfusion sequence with Poisson-disc acquisition pattern along k-t dimension. (b) Apply the k-t based image reconstruction technique for this Cartesian acquisition. (c) Develop the deep learning-based rapid image reconstruction techniques for Cartesian 2D and SMS perfusion imaging. (d) Validate the proposed technique in both healthy volunteers and patients.

Acknowledgement

The completion of this thesis is not possible without the support and assistance of lovely people. I would like to start with a summary for my PhD journey and acknowledge people around me who make this happen.

Everything started from the spring of 2016, before which I had barely thought to start my PhD study. The second semester of my junior year in college, I went to UC San Diego as an exchange student, and that was the first time I went abroad and the first time I came to the US. Except busy with coursework, I was lucky to be one of the visiting students at Prof. Thomas Liu's functional MRI lab, where I firstly got a closer look at a researcher's life and found it was interesting to solve problems using learned knowledge. While I was transferring at San Francisco, I visited the beautiful campus of Stanford University. Seeing the wonderful life of doing research at US and impressed by the beauty of California, I aspired to come back one year later to attend graduate schools in the US. Although that spring was just four-month long, it did change my life path.

After heading back to China, I worked as an undergraduate research student with Prof. Huijun Chen at Center for Biomedical Imaging Research in Tsinghua University, where I started to embark on the research of MRI. The project I worked on was reconstruction for liver dynamic contrast-enhanced imaging. This work was accepted by ISMRM 2017. I still remember how excited I was when I went to Honolulu to present my work, which was also the first time I attended an academic conference. I really appreciate the time at Tsinghua, where open-minded research environment, great professors and students impacted me a lot.

After the application season, I decided to go to UVA and join Dr. Michael Salerno's lab for my graduate study with the research focus on cardiac MR imaging. I arrived at Charlottesville on July 28th, 2017, a rainy and peaceful day. However, the start of the study was not excited as what I thought. As an international student, I tried to adapt to the life of graduate school in the US. For the first two years, I was busy with coursework and trying to figure out my research projects. Seeing too many obstacles, I felt probably I was not suitable for PhD study. Throughout that hard time, the support and encouragement from my family, advisor, lab members and friends made me decide to do one more thing and try it for another time. Luckily, with hard work and insistence, it seemed that everything suddenly worked out in the spring of 2019. At the end of the summer, on August 15th, 2019, I succeeded to pass my PhD candidacy exam. Through the end of 2019, I continuously worked on my

research projects with the guidance of my advisor, and conference proceedings were accepted by SCMR and ISMRM. The moment I did oral presentations at the conference, I felt everything finally paid off.

2020 was a tough year with the influence of COVID-19 pandemic. I was working from home and trying to come up with research ideas every afternoon when I was jogging in the parking a lot of a church that was near my home. I also remember that I sat on the stairs in front of my home having numerous phone calls with my advisor to discuss research projects and exchange opinions. Finally, at the end of that summer, Aug 15th, 2020, one year after my candidacy exam, I submitted my first journal paper manuscript. It took much longer than I thought to put a journal paper from the scratch. From 2020 to 2021, intrigued by the deep learning techniques, I took the computer vision course and extended the course project to my research focus, which was the fundamental of the DESIRE project as shown in Chapter 4:. With more experience, I feel I am much more confident than the time I was admitted to graduate school in 2017. Furthermore, the Cartesian perfusion imaging with deep learning-based rapid imaging reconstruction is being developed since 2021.

After summarizing this journey that I have gone through, I want to thank people who have accompanied with me along this trip in the past several years.

I am grateful to have the opportunity working with my advisor - Dr. Michael Salerno over the past several years. There were endless of days having research conversations and discussions with Michael. Whenever I have a question, he is always there answering every single detail of my question. There were also endless moments I had troubles in my research projects, and Michael was always patient and guided me through. Though being a doctor is especially difficult during the pandemic, Michael has been doing regular online meetings with me and our group. What's more, he not only teaches knowledge without any reservation, but also shows enthusiasm towards research and kindness to people around him, which has been motivating me to be a nice and kind person like him. I have also learned a lot from our discussions, not just on MRI research, but on many aspects of life. The life of doing research at UVA is the most meaningful time in my life so far, and all of this makes me decide to continue working as a researcher after graduation. Besides, Michael, and his family's care towards me makes me feel warm at a land that is thousands of miles away from home. I also want to express my gratitude to Michael's family-his wonderful wife, lovely sons who also gave me the first experience of rock

climbing and kayaking. There is a saying in Chinese – *'一日为师，终身为父'*, which means *'Even if someone is your teacher for only a day, you should regard him like your father for the rest of your life'*. Michael, I am forever in debt to you.

I have also been fortunate to be a trainee of the MRI group at UVA. Prof. Craig Meyer has been kindly serving as my committee chair. It was from Prof. Meyer's MRI course that I learned a lot about MRI. Three years ago, when I passed my candidacy exam, he said *'Doing PhD study is hard, and I wish you could still continue loving the research you do and working hard on it'*. Over the years, I realize that motivation and persistence are of importance for PhD study and research career. Prof. Meyer, thanks for your encouragement! Prof. Frederick Epstein is also very supportive of my study. Though serving as our department chair might make his schedule busy, he has been actively joining a lot of research discussions and he brought up a lot of interesting ideas on my research projects especially for the SMS project. I am also grateful to Dr. Christopher Kramer, who has been providing the prompt clinical support of our work. As a trainee, I am astonished by his time management and efficiency. Prof. John Mugler, who is also serving in my committee, is still actively doing MRI research by himself. The discussion with him gives me lot in-depth understanding of MRI. Except for the people in my committee, I also want to acknowledge Dr. Daniel Weller, who is currently working at KLA semiconductor. While he was an assistant professor at UVA, his insights about MR image reconstruction and deep learning made me grab a better understanding of signal and image processing. It was also a pleasure to take Dr. Weller's engineering courses, through which I learned a lot about signal processing. I also want to acknowledge Prof. Wilson Miller who taught the *advanced MRI* course and hands-on lectures about MRI coils, which strengthened my understanding about MRI. Through working with great faculties around me, their enthusiasm on research and the love towards life has been influencing me and make me want to grow to be a person like them.

I also would like to acknowledge my fantastic lab members. Dr. Yang Yang, who was Dr. Salerno's first student, did a lot of pioneering works on spiral perfusion imaging. Actually, this dissertation is mostly based on his previous works. Except for research, Yang and his wife have been supporting me a lot in life. I also want to thank Dr. Ruixi Zhou for her help and support over the past several years. My amazing lab members and friends Dr. Matthew Van Houten, Xitong Wang and Marina Award are also an essential part of my life. I would

like to acknowledge our cardiology fellows Dr. Patricia Rodriguez Lozano, Dr. Austin Robinson, and Dr. Jonathan Pan as well, who has been supporting our perfusion studies for many years. I am also extremely grateful to our clinical coordinators - Caroline Flournoy, Sara Prince and Jayne Missel and clinical technicians - Jamie Lynn Weathersbee, and Jose M. Reyes. I also want to thank Joe Di Maria for the technical support. It is their support and professionalism that make this dissertation happen!

UVA Biomedical Engineering Department's faculties and staff are also an integral part of my study. I would like to thank our graduate program director - Prof. Shayn Peirce-Cottler, who is a wonderful woman and always support our studies. I would also like to acknowledge our graduate student coordinator - Kimberly Fitzhugh-Higgins, who is super nice and professional to answer any questions I have.

Since moving to Stanford University as a visiting graduate student in the December of 2021, I have been lucky to have nice faculties and staff around me. I want to acknowledge Prof. Kawin Setsompop for the wonderful research discussion with him. I would like to thank Prof. Daniel Ennis for his support on my study. I also would like to acknowledge Brooke Gazzoli, Kathleen M. Gallagher, Julie Hutchinson, Jean Sullivan, and Aya H Golan who make my move much easier and life at Stanford much enjoyable.

I am also lucky to have a wonderful summer internship at HeartVista, Inc. As a machine learning engineer intern, it was great work with Okai Addy, Jason He, Arun Seetharaman, and other wonderful colleagues.

I am super grateful to have a group of wonderful friends around me. I want to thank my close friend - Zhixing Wang, who is a graduate student in Prof. Meyer's lab, for his support and help over years. Zhixing has been a close companion whenever I need help. Except for this, his passion about life has been motivating me. Also, I have been fortunate to take courses and discuss questions with Quan Dou and Zhixing. Every discussion of MRI questions and homework problems with you benefited me a lot. I am also grateful to have Sheng Chen, Kang Yan, Yanjun Xie, Tiantian Xu, Jiayong Li, Yuxing Xu, Xiang Guo as my friends. It is truly a pleasure that we not only do research together, but also hang out together. I will miss the time playing tennis, fishing, swimming, and skiing with you guys! We will graduate one day in the future, but our friendship will not end here. At Stanford, it is so great to have Dr. Congyu Liao, Dr. Xiaozhi Cao, Dr. Erpeng Dai and Dr. Xue Zhang as my friends, whose support and help mean a lot to me.

Specifically, I would like to express my appreciation for Miss Xuan Liu, who has been such an essential part of my life. I thank her for her unconditional love, support, and encouragement that keep me growing to be a person I would like to be. Xuan is also an excellent researcher and passionate about life. To be honest, she is my wonderful life partner I could ever imagine. Xuan, I am looking forward to every single day with you in the future!

Finally, I would like to express my thanks to my family. I grew up at a small city - Xiaoyi in Shanxi Province, China. The lovely people there and family members shaped my personalities and characters. My father Chenglong Wang and my mother Liqin Wu have been supporting me without any reservation. Over many years, they have been working hard to provide me and my sister a good life. Their genuine love towards life and the attitude of always kindly treating people around them have been motivating me to be a person like them. They not only give me life, but also are my first teacher of life. Due to the pandemic, we haven't sees each other for three years. Mom and dad, I wish I could go home and visit you very soon! Except for my parents, my younger sister - Danyu has been caring about my study and life at US. I wish you all the best for your graduate studies at US! My grandmother (my mother's mother), uncle and aunt are also supportive of my studies and career development. The care from my family always relieves me every time when I meet difficulties. I wish I could take you to visit my school at US after the pandemic. It was a great pity to see my grandmother (my father's mother) and my grand grandmother (my mother's grandmother) who raised me up pass away in 2021. Although they didn't get educated, their love to me gave me the best childhood life and shaped my characters. Their wish was seeing me graduate and form a new family with someone I love. Yes, I am making progress and please rest in peace. In a word, it is my greatest fortune to grow in this family and have you as my family members.

I would like to end with a quote from Steve Jobs' commencement address at Stanford University in 2005, which has been motivating me through years - *'stay hungry, stay foolish'*.

University of Virginia Junyu Wang

June 22, 2022

Table of Contents

List of Figures

List of Tables

Chapter 1: Introduction

Magnetic resonance imaging (MRI) is a non-invasive medical imaging modality that provides excellent soft tissue contrast without using ionizing radiation. MRI can also be sensitive to many specific biological parameters, and it has been widely applied on many areas including measuring brain oxygen saturation level changes due to neurological activity, measuring the blood flow velocities, and measuring the temperature and metabolism activities.

Since its invention more than forty years ago, significant research has been focused on improving its imaging speed and quality. Over the decades, fast imaging techniques such as non-Cartesian imaging, simultaneous multi-slice (SMS) imaging, accelerated imaging techniques such as parallel imaging (PI) and compressed sensing (CS) have been developed. Recently, deep learning techniques are also being developed to advance the image reconstruction and post processing of MRI.

Coronary artery disease (CAD) is the presence of atherosclerotic plaques in the coronary arteries, and it is the most common type of heart disease in the United States (US). As the main death cause in the US, it is responsible for 1 in 7 deaths[2]. MRI, which is non-invasive and non-ionizing, can be utilized to diagnose CAD. Specifically, cardiac magnetic resonance (CMR) quantitative myocardial first-pass perfusion imaging is an emerging valuable tool to diagnose CAD.

With the development of research over decades, the CMR perfusion imaging technique is able to provide an accurate assessment of myocardial ischemia and a comprehensive evaluation of myocardial function and infarction[3–6]. However, current clinically available techniques have limited in-plane spatial resolution (~2-3 mm) and incomplete heart coverage, which impede the assessment of transmural perfusion differences and underestimate the extent of ischemia. Furthermore, motion-induced dark-rim artifacts can significantly reduce image quality and limit evaluation of the sub-endocardium, which is most sensitive to myocardial ischemia[7]. Recent studies from our lab have demonstrated CMR quantitative spiral perfusion techniques for both single-slice (SS) and SMS acquisitions enabling whole-heart coverage (6-8 slices) with high spatial resolution (2×2 mm^2)[8,9]. Also, our lab has developed novel motion-compensated CS L1-SPIRiT reconstruction techniques, that

correct for breathing motion and enable free-breathing acquisition[8]. Sampling efficiency can also be improved by using outer-volume suppression (OVS) technique to achieve a reduced field-of-view (rFOV) so that the sampling in k-space can be coarser[10]. We have previously applied an OVS technique for single-shot spiral perfusion imaging and demonstrated that it produced superior image quality as compared with full-FOV acquisitions[11]. We have also developed a quantification pipeline for spiral perfusion imaging to quantify myocardial blood flow and myocardial perfusion reserve (MPR). High diagnostic accuracy of the proposed techniques has been demonstrated[12–14].

With higher spatial resolution, there is an increased ability to detect transmural perfusion differences between the epicardium and the endocardium, which could improve the ability to detecting obstructive CAD as demonstrated in prior studies[15–18]. Additionally, one significant barrier to clinical translation of these techniques is the need for off-line reconstruction and quantification which currently takes hours to complete, and thus cannot provide data to physician in a clinically acceptable time frame. Considering that greater than 10 million stress tests are performed in the US alone, improvements in the accuracy of non-invasive assessment of CAD could significantly reduce health care costs resulting from incorrect diagnoses.

This thesis aims to develop fast and high-resolution imaging techniques for CMR first-pass myocardial perfusion with whole-heart coverage, and it is organized as follows:

Chapter 2: provides a background of MRI, CAD, imaging modalities used to diagnose CAD, and how CMR first-pass myocardial perfusion imaging can be utilized to diagnose CAD. Specifically, spiral imaging, accelerated imaging techniques including PI and CS, SMS imaging, CMR imaging protocols, CAD and its diagnosis will be covered. Additionally, to motivate Chapter 4, deep learning-based image reconstruction is also illustrated.

In Chapter 3:, the high-resolution spiral perfusion imaging technique at 3 T is described. The proposed method utilized fast imaging techniques including SMS and/or OVS to provide high-resolution (1.25×1.25 mm^2) imaging with adequate signal-to-noise (SNR). Detailed descriptions of pulse sequences, reconstruction methods

and post processing are illustrated. Specifically, for SMS imaging, a newly proposed CS-based image reconstruction method (i.e., spiral SMS-Slice-L1-SPIRiT) is described.

In Chapter 4:, a DEep learning-based technique for Spiral perfusion Image Reconstruction (DESIRE) is described. The proposed technique aims to overcome the long off-line reconstruction times and provide a clinically acceptable rapid image reconstruction time (<1s inference time for a dynamic image series at each slice location) for both SS and SMS spiral perfusion imaging. The proposed technique was applied to high resolution spiral perfusion imaging at 3 T and extended to spiral perfusion imaging at 1.5 T as well.

In Chapter 6:, a high-resolution Cartesian perfusion imaging at 3 T with deep learning-based rapid image reconstruction technique is proposed. As Cartesian perfusion techniques are most commonly deployed clinically, we also sought to evaluate the proposed CS, SMS, and deep-learning techniques for Cartesian high-resolution perfusion imaging for both single slice and SMS acquisitions with an MB factor of 2 using a 2D Poisson-Disc incoherent sampling pattern along temporal dimension.

Chapter 6: summarizes the work of this dissertation and discusses several potential future directions including the deep learning-based rapid quantification analysis for spiral perfusion imaging, deep learning-based rapid spiral cine image reconstruction and analysis, T_1 mapping with deep learning-based reconstruction and an on-line implementation of the proposed deep learning techniques, etc.

Chapter 2: Background

The chapter aims to provide the readers with the relevant background about this thesis. Firstly, a brief introduction to MRI hardware and image acquisition will be described. To motivate following chapters, spiral imaging, accelerated imaging techniques including PI and CS, SMS imaging, and deep learning-based image reconstruction will be illustrated. CAD and the CMR quantitative myocardial first-pass perfusion imaging will be described to understand how MRI can be utilized to diagnose CAD. To better understand the innovation of this thesis, a brief overview of our lab's previous work on spiral perfusion imaging is also covered.

2.1 Magnetic Resonance Imaging

Medical imaging modalities, such as X-ray, Ultrasound, CT, MRI, Positron Emission Tomography (PET) and Single Proton Emission Computed Tomography (SPECT), are non-invasive and able to detect anatomical or functional information from the human body. This information can help doctors determine a specific diagnosis and determine an appropriate treatment plan.

Unlike other medical imaging modalities, MRI provides images with superior soft tissue contrast without ionizing radiation. Additionally, flexible imaging planes provided by MRI improves visualization of certain structures. Most importantly, MRI can be made to be sensitive to various physical and physiological related tissue properties, which could potentially be more sensitive and specific to the disease status, providing the possibilities of quantitative diagnosis[19]. Since its invention in 1973, MRI has become an important clinical diagnostic tool targeting many prevalent human diseases including stroke, cardiovascular disease, cancer, liver diseases, arthritis, etc.

2.1.1 Imaging Hardware

The key components of MRI are the interactions of the magnetization with three types of magnetic fields and the ability to measure these interactions. As noted by its name, magnetic fields are of importance for MRI. There are three types of magnetic fields utilized in MRI.

The Static B_0 Field

Atoms with an odd number of protons or neutrons possess a nuclear spin angular momentum. Qualitatively, these nuclei can be visualized as spinning, charged spheres that give rise to a small magnetic moment. In the human body, which consists largely of water, hydrogen nuclei possess this spin behavior, and are the signal sources for conventional MR imaging. For different parts of body, hydrogen concentration and the local water environment differ. For example, the gray and white matter in the brain have different hydrogen concentration and local water environment, providing tremendously valuable soft tissue contrast for imaging[20].

In the absence of an external magnetic field, magnetic moments in the body are randomly oriented. In MRI, a static main magnetic field, denoted as B_0, is always applied. There are two notable effects after applying a strong static magnetic field - B_0. Firstly, a small fraction of the magnetic moments will align with the applied field. Secondly, once excited, the magnetic moments will process at the Larmor frequency. This frequency, ω, is proportional to the applied field strength, i.e., $\omega = \gamma B_0$, where γ is the gyromagnetic ratio which is a constant for a given nucleus. For ${}^1_1H$ which is the main signal source in human body, the γ is 42.58 MHz/T, which leads to a ω of 127.74 MHz and 63.87 MHz for 3 T and 1.5 T magnetic fields, respectively.

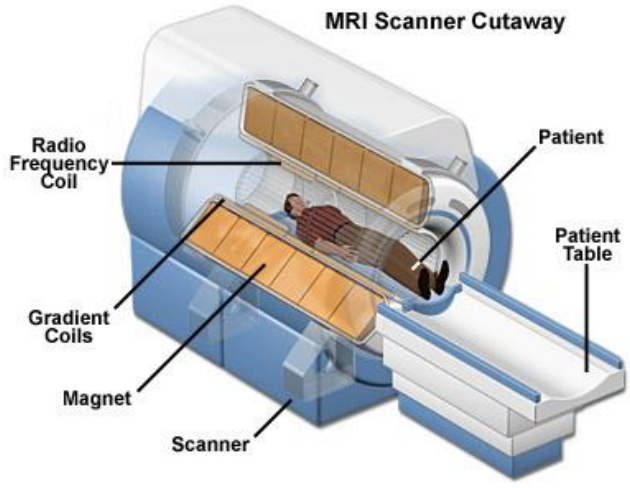

Figure 2-1. The layout of the magnetic fields in MRI. Adapted from nationalmaglab.org.

This static field points along the longitudinal direction and its strength determines the net magnetization and the resonance frequency as described above. Also, it is worth noting that the field homogeneity is very

important for MR imaging. Inhomogeneity often results in image distortion artifacts. In most clinical scanners the field is generated using a superconducting magnet though some systems use permanent magnets or electromagnets. Across the MR industry, most scanners are 1.5 T or 3 T, however there are varying strengths below 1.5 T and more recently, up to 7 T. For CMR imaging, it is usually conducted at 1.5 T and 3 T scanners. Recently, research regarding low field imaging at 0.55 T is becoming popular due to their favorable physical properties, reduced costs, and increased accessibility to patients with implants[21].

Transverse Radiofrequency B_1 Field

MRI can be considered as a two-phase experiment – excitation phase and acquisition phase. The excitation phase involves exciting magnetic moments away from their minimum energy state, and a B_1 field is used to excite the magnetization from equilibrium by tipping it from the longitudinal direction to the transverse plane to produce a detectable signal. During the subsequent acquisition phase, the signal is detected via induction, encoded, and collected as the spins relax back to the minimum energy state[20].

During the excitation phase, a radiofrequency (RF) magnetic pulse B_1, produced by coils tuned to the resonant frequency of the magnetic moment (i.e., Larmor frequency), is applied in the x-y (transverse) plane[22]. This pulse will create a torque that rotates the magnetic moments away from their minimum energy state. More importantly, this pulse is programmable, and engineers can modify the pulse sequences to manipulate the states of spins, resulting in different imaging possibilities such as images with different contrast.

During the acquisition phase, for 2D imaging, Faraday's law of induction predicts the generation of an electromotive force (EMF) in properly oriented RF receiver coils because the spinning of the magnetic moments exists in transverse plane (i.e., x-y plane). Thus, it is only the transverse component of the magnetization that contributes to the signal acquired[23]. In this way, this voltage is indeed the MR signal that is used for imaging, and the received signal is the cumulative contribution from all excited magnetization in the volume. It is also worth noting that, for many applications, the same set of coils are employed for both RF pulse transmission and data collection[20].

Spatial Encoding Gradients

With only the homogeneous B_0 field present, the system does not contain any spatial information. The spatial distribution information comes from three additional fields that vary spatially, which is shown in the signal equation in the next section.

Three gradient coils, G_x, G_y and G_z create a linear variation in the longitudinal magnetic field strength as a function of spatial position. For example, when G_x is applied, the magnetic field will vary with position x: $B(x) = B_0 + G_x x$. As a result, the resonance frequency of the magnetization will vary proportional to the gradient field.

2.1.2 Image Acquisition

The design of MRI acquisition methods is mainly about the development of the gradient waveforms that drive the MR system. These waveforms, along with the associated RF pulses used to produce the magnetization, are called a pulse sequence, which determine the way that MR scanner acquires images[24].

For 2D imaging, since the spatial localization is required only in the x and y directions, the received time signal from an excited plane can be expressed as[23]:

$$s(t) = \int_x \int_y m(x,y) e^{-i2\pi[k_x(t)x + k_y(t)y]}\, dxdy \qquad \textbf{[2-1]}$$

where $k_x(t) = \frac{\gamma}{2\pi}\int_0^t G_x(\tau)d\tau$ and $k_y(t) = \frac{\gamma}{2\pi}\int_0^t G_y(\tau)d\tau$ are the time integrals of the gradient waveforms, and $m(x,y)$ is the transvers nuclear magnetization distribution of interest. Ultimately, we wish to reconstruct an image $I(x,y)$ that most closely approximates $m(x,y)$. In general, $m(x,y)$ is a function of the nuclear magnetic resonance parameters $\rho(x,y)$ (density), $T_1(x,y)$ (also known as the spin-lattice relaxation time, is a measure of how quickly the net magnetization vector recovers to its ground state in the direction of B_0) and $T_2(x,y)$ (also known as spin-spin relaxation time, refers to the progressive dephasing of spinning dipoles resulting in decay in the magnetization in the transverse plane).

Unlike optical imaging, the raw data collected by MRI scanner is the spatial frequency information rather than the image itself. The acquired MR signal fits the nature of Fourier transform (FT), and a Fourier transform relationship exists between the image space and the MR data space, usually referred to as k-space as illustrated in Figure 2-2. If the k-space data is collected following the Nyquist-Shannon sampling rule, the acquisition is referred to as a "fully-sampled" acquisition. In the fully sampled case, specified by the desired spatial resolution and the size of the field of view (FOV), a certain amount of data is distributed in the k-space with a certain density. If higher spatial resolution or larger FOV is desired without compromising the other imaging protocols, more k-space data must be collected, which leads to an increased acquisition time.

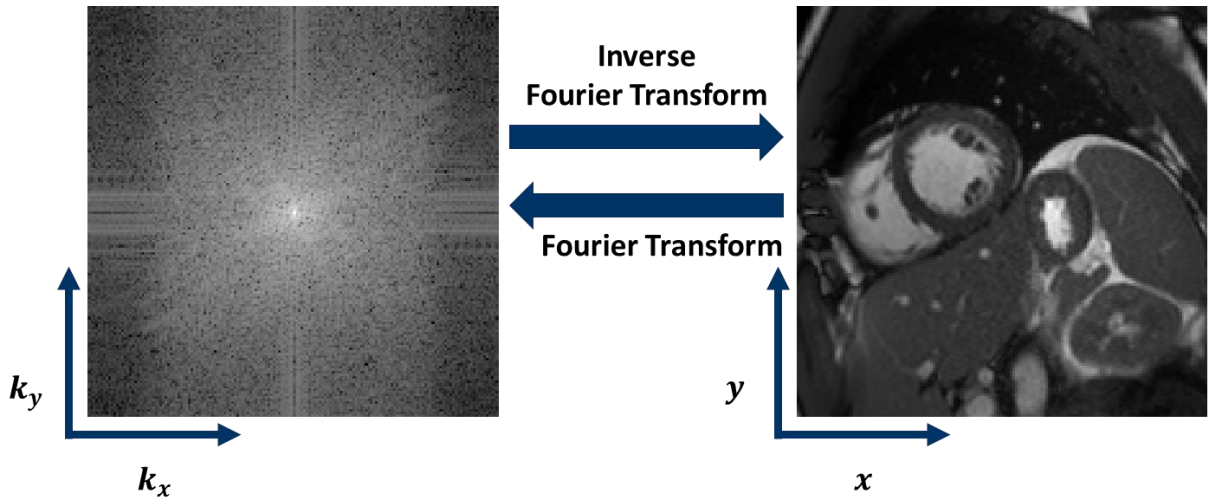

Figure 2-2. The Fourier relationship between k-space and MR image. Example shows a short-axis cardiac image.

In principle, a complete MR image can be reconstructed from a single acquisition by inverse Fourier transform using the k-space trajectory that covers the whole region of k-space. This is commonly done in applications such as brain imaging. However, for most applications like CMR imaging, this results in inadequate image resolution and excessive image artifacts since the data acquisition window is usually limited in each heartbeat. Also, the gradient system performance limitation such as the maximum gradient amplitude and the maximum slew rate (defined as the rate of change of the gradient) of the scanner, physiological constraints such as peripheral nerve stimulation (PNS) and specific absorption rate (SAR) from the patients limit the speed at which k-space can be traversed[25]. These effects could limit the total number of samples per acquisition. As a

result, most MR imaging methods use a sequence of acquisitions to acquire different segments of k-space. The data from this sequence of acquisitions is then used to reconstruct an image.

2.1.3 k-space Sampling

Before generation of the MR signal, k-space is just an array of blank cells awaiting the arrival of data. Although there is no direct correspondence between the location of a cell in k-space and location of a pixel in the image, different parts of k-space do correspond topologically to spatial frequencies in the MR image. Data near the center of k-space, where the energy of an image is mostly concentrated, corresponds to low spatial frequencies (i.e., general shapes and contours) while the data from the periphery corresponds to high-spatial frequencies (i.e., edges, details)[25].

As shown in equation [5-1[5-1, the integral of the $G_x(t)$ and $G_y(t)$ gradient waveforms are $k_x(t)$ and $k_y(t)$ that determine which k-space point to fill in at each time point, resulting the trajectory in k-space. The encoding direction along $G_x(t)$ is usually called the frequency encoding direction, while the encoding direction along $G_y(t)$ is usually called the phase encoding direction. There is considerable freedom in designing the k-space trajectory for each acquisition. Common 2D sampling trajectories are illustrated in Figure 2-3.

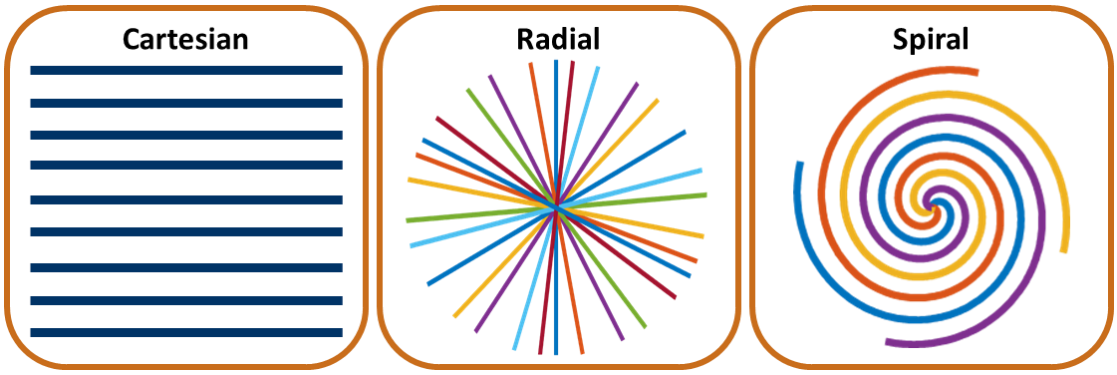

Figure 2-3. Common 2D sampling trajectories. From left to right: Cartesian 2D, radial, and spiral.

The classic way to sample the k-space is to acquire data using straight lines from a Cartesian grid, which is termed as 'Cartesian sampling'. Most pulse sequences used in clinical imaging today are Cartesian sampling. With the Fourier transform relationship between k-space and image space, the reconstruction from Cartesian acquisitions is simply the inverse Fourier Transform. More importantly, Cartesian sampling can be robust to

many sources of system imperfections such as gradient imperfections[19,25]. Furthermore, when acquiring data at each line, the current hardware techniques allow the scanner to perform oversampling in the direction of phase encoding without affecting the total acquisition time. This oversampling in one direction can prevent the aliasing if the object is larger than FOV in that sampling direction.

The sampling of k-space can also be conducted using a non-Cartesian approach. Since the energy of an image is mostly concentrated around the k-space center, non-Cartesian trajectories can be designed as variable density, where the center of the k-space is sampled more often than the outer part of the k-space. This variable density sampling maintains a relatively high sampling efficiency and makes the dataset more robust against motion/flow artifacts and undersampling artifacts[19]. Among all the non-Cartesian trajectories that have been used in MR imaging, radial and spiral trajectories are the two most common trajectories.

The radial trajectory can be considered as rotated Cartesian lines, and it is inherently variable density because each line samples the center of the k-space. The first MR imaging proposed in 1973 utilized the radial sampling trajectory and Fourier central slice theorem to reconstruct the image[26]. This sampling pattern is valuable for clinical applications that require high temporal resolution such as cardiac imaging, time-resolved angiography, and perfusion imaging[19].

Compared to the radial trajectory, the spiral trajectory has a higher sampling efficiency and a larger flexibility in designing variable sampling density in k-space. The variable density is commonly designed as a linearly or quadratically decreasing function of the radius of the spiral arms. The first spiral images were published by Ahn et al[27]. Then, the spiral trajectory was proposed to increase the spatial and/or temporal resolution of coronary artery imaging and fluoroscopy[28,29]. It has also been used to reduce spatial side lobes in chemical shift imaging[30] and to improve the spatial-temporal resolution for cardiac imaging such as cine imaging[31], T_1 mapping[32] and perfusion imaging[8,9,11,33,34].

Non-Cartesian sampling approaches have many advantages over Cartesian acquisition methods such as reduced acquisition time, insensitivity to motion artifacts and undersampling artifacts. More importantly, the variable-density-sampled non-Cartesian trajectory can be designed in a way that can give rise to relatively

incoherent undersampling artifacts[19], which is one of the three requirements for the compressed sensing algorithm introduced later. For this reason, the variable density sampling trajectory such as radial and spiral trajectory facilitates the application of compressed sensing in MR imaging to significantly reduce the scan time.

However, non-Cartesian sampling also has disadvantages. Firstly, additional data gridding and density compensation are usually required to reconstruct images, which makes reconstruction more challenging and time consuming. Moreover, non-Cartesian trajectories are also sensitive to magnetic field inhomogeneity, gradient delays, signal decay and other source of the imperfections[19]. In Chapter 3:, a CS-based image reconstruction algorithm for spiral perfusion imaging is presented, which takes around an hour for an image series with fifty dynamic images at a slice location.

There are other non-Cartesian trajectories such as the PROPELLER trajectory[35] , rosette trajectory[36], 3D cone imaging[37], FLORET[38], Yarnball[39], Seiffert spirals[40], SPARKLING[41], etc. Each non-Cartesian trajectory has specific properties that can be exploited to improve certain imaging applications.

2.1.4 Accelerated Imaging Techniques

Since the invention of MRI more than 40 years ago, the speed of MRI has improved dramatically while achieving high image quality. Specifically, for CMR imaging, fast imaging techniques are required to capture the relevant physiological changes such as cardiac motion, blood flow, or perfusion.

In addition to improved MRI hardware systems, much of the speed is due to the application of efficient sampling strategies and data can be undersampled even below the Nyquist limit and un-sampled data could be recovered using the relationships brought by coil redundancy. This technique, termed as “parallel imaging (PI)”, can be conducted either at k-space or the reconstructed image space. Since the late 1990s, PI techniques such as SMASH[42], SENSE[43], GRAPPA[44] and SPIRiT[45] have been proposed to accelerate the imaging speed. Over the past three decades, parallel MRI has evolved rapidly, and it is implemented on most clinical MR scanners in use today.

Compressed sensing (CS), unlike PI, implicitly compresses the data within the data acquisition process by obtaining fewer incoherent measurements. Images can be accurately reconstructed from these measurements

using non-linear reconstruction algorithms. The way data are acquired in MRI is compatible with the CS theory. The practical result of CS in the context of MRI is that MR images require much less data for reconstruction.

Parallel Imaging

Parallel imaging and conventional non-accelerated imaging share the common features of multiple receiver coils but process the received signal in a different way. In conventional MRI, we can combine data from each surface coil to produce a composite image of the brain at full FOV. This arrangement may provide improved SNR and spatial resolution compared to that obtainable from a single large head coil but produces no gain in speed.

To shorten the imaging time, the number of phase encoding lines in PI is reduced. For speed to be doubled at constant resolution, only half of the lines of k-space are acquired. This strategy, however, violates the Nyquist sampling theorem and results in an insufficient number of spatial frequencies collected to adequately represent the imaged object, which leads to a reduced FOV, and aliasing ("wrapping-around" artifacts) is seen in the reconstructed image. The fundamental of PI is to "unfold" this "wrapping-around" artifacts using spatial information about the coils, and this can be conducted in both image space and k-space[25].

Parallel imaging techniques generally fall into two categories: those were reconstruction takes place in the image domain requiring an unfolding or inversion procedure and those that take place in k-space where calculation of missing data is performed prior to reconstruction.

The typical PI conducted in the image domain is SENSitivity Encoding (SENSE)[43]. As shown in Figure 2-4, during the pre-scan calibration step the scanner has calculated point-by-point sensitivities for each surface coil. For an MR signal arising from point A in the patient, the sensitivities of coils 1 and 2 for detecting that signal will be denoted S_{1A} and S_{2A}, respectively[25]. Similarly, the coil sensitivities for any other point B are also known and will be denoted S_{1B} and S_{2B}.

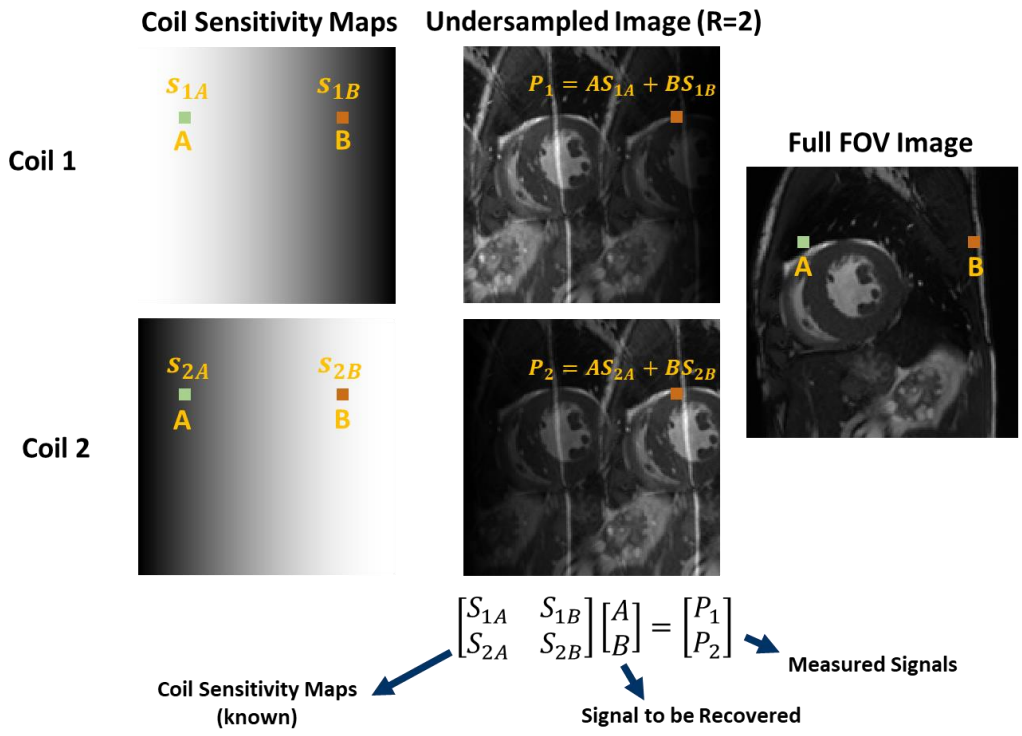

Figure 2-4. Illustration of the SENSE reconstruction method for a cardiac short-axis image with an undersampling factor of 2.

When the data from each coil are reconstructed into images, "wrapping-around" artifact is present. Due to the insufficient sampling in the k-space. Each pixel (P) in the $\frac{1}{2}$-FOV images has a signal that is the sum of contributions from two points (A and B) in the subject. Denoting these pixel values from coils 1 and 2 by P_1 and P_2, we have:

$$\begin{cases} P_1 = AS_{1A} + BS_{1B} \\ P_2 = AS_{2A} + BS_{2B} \end{cases} \quad \textbf{[2-2]}$$

Since the P_1, P_2 and S_1, S_2 are all known, the true signals (A and B) can be calculated by simple algebraic methods for solving 2 simultaneous equations with 2 unknowns. In the MR scanner, a similar process is performed for all data points in the image using a matrix inversion technique, but the idea is the same.

On the other hand, k-space PI techniques operate on signal data within the complex frequency domain before it has been transformed into an image. The typical k-space based PI method is GeneRalized Autocalibrating Partially Parallel Acquisitions (GRAPPA)[44]. As shown in Figure 2-5, known data from the

autocalibration region (fully sampled k-space center) are used to calculate weighting factors for each coil. These weighting factors reflect how each coil distorts, smears, and displaces spatial frequencies within the full FOV k-space data. Missing k-space points are estimated in an iterative fashion using these global weighting factors combined with local known data for each small region (usually referred to a kernel). Note that weighting factors and known data from all coils are used to estimate missing data for each coil.

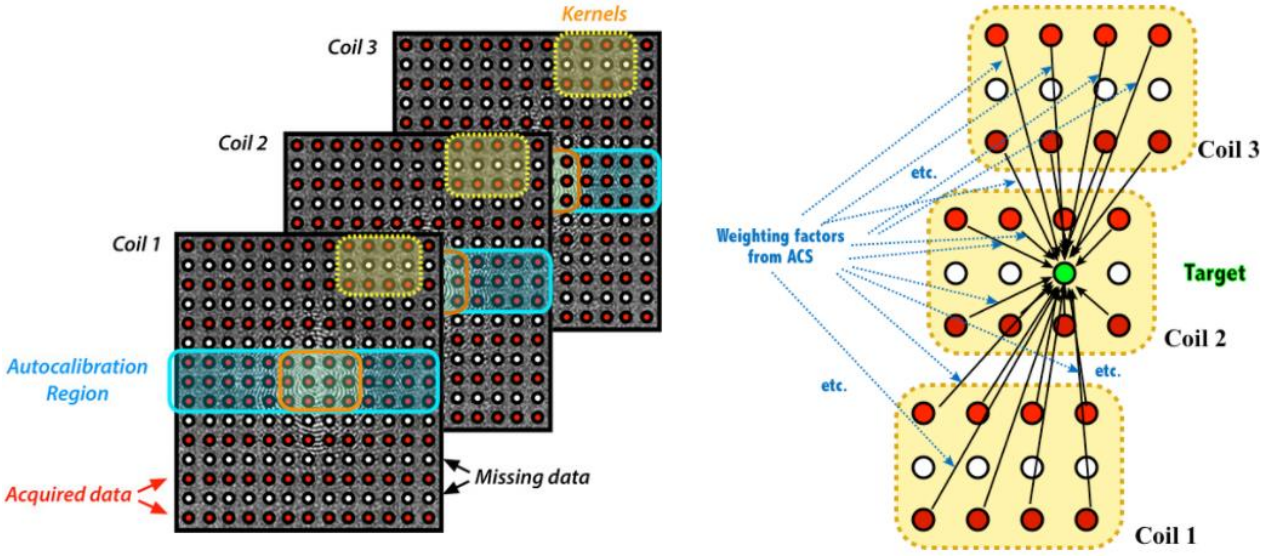

Figure 2-5. Illustration of the GRAPPA. Adapted from Questions and Answers in MRI Website.

Notwithstanding these subtle distinctions, SENSE and GRAPPA are largely interchangeable for nearly all applications. The PI technique can also be applied on non-Cartesian imaging by tailoring the kernel shape for non-Cartesian GRAPPA[46] or formulating the reconstruction problem as a general inverse problem with self-consistency and/or data consistency[45,47].

Kernel-based iterative reconstruction method-SPIRiT[45] could further extend the reconstruction to a more generalized fashion not limited to Cartesian acquisition:

$$\underset{x}{argmin}||Ax - y||_2^2 + \lambda||(G - I)x||_2^2 \qquad \textbf{[2-3]}$$

where x is the image(s) to be reconstructed, y is the acquired k-space data, A is the operator that maps the image data to the k-space data which can be Fourier transform or NUFFT[48] operator for non-Cartesian acquisitions, G

is the SPIRiT operator matrix obtained from the calibration, and λ is the parameter balances the data fidelity term (first term) and self-consistency term (second term). The beauty in this formulation is that the calibration consistency is always applied to a Cartesian space, even though the acquired data may be non-Cartesian. The treatment of non-Cartesian sampling appears only in the data consistency term. This algorithm could be solved efficiently by iterative descent methods such as steepest descent or the much more efficient conjugate gradient algorithm. It is also worth noting that the SPIRiT operator could be performed on both image space and k-space, and the algorithm could be further extended with the sparsity term as described in the following section.

Compressed Sensing

Compressed sensing (CS) refers to a group of methods for accelerated MR data acquisition based on semi-random, incomplete sampling of k-space. The CS theory was introduced to MR imaging around 2007 by Lustig et al[49] and has had a high impact to the field since then. To date, it is the most cited paper in the leading MRI technical journal Magnetic Resonance in Medicine (MRM). Using CS, unlike the other conventional fast imaging techniques such as parallel imaging, a high acceleration rate can be achieved with little or no cost of image quality.

The CS theory is based on the fact that most natural images, including medical images, present redundant information which can be utilized to decrease the number of measurements without sacrificing the reconstruction quality. The CS approach requires that: (a) the desired image have a sparse representation in a known transform domain (i.e., is compressible), (b) the aliasing artifacts due to k-space undersampling be incoherent (noise like) in that transform domain, (c) a nonlinear reconstruction be used to enforce both sparsity of the image representation and consistency with the acquired data[24]. The data redundancy is represented as the concept of "sparsity" in the CS theory, which defines that a sparse data has a small amount of non-zero-value entries. A transform of the data can be used to "sparsify" the data, namely that transforming the data into certain domain, referred as the "sparsity domain", where it presents sparsity. The transform is referred as the "sparsity transform". The image reconstruction process to generate a final image is an iterative optimization process, and

it can be considered as a "denoising" process[49]. However, the utilization of CS-based reconstruction algorithm usually requires a relatively long reconstruction time and sometimes requires off-line processing.

A CS-based general reconstruction problem can be formulated as:

$$\underset{x}{argmin}||Ax - y||_2^2 + \lambda||\Psi x||_1 \quad \textbf{[2-4]}$$

where x is the image(s) to be reconstructed, y is the acquired k-space data, A is the operator that maps the image data to the k-space data, Ψ is the sparsifying operator on the image space, and λ is the parameter balances the data fidelity term (first term) and sparsity transform term (second term).

Both the PI and CS reconstruction can be written as the optimization problem, providing the opportunity to combine these two techniques together to achieve higher acceleration for perfusion imaging by exploring the sparsity of dynamic images from multiple coils. For image-space PI, the coil sensitivity information can be incorporated into A, while for k-space PI a separate term can be incorporated denoting the self-consistency, leading to the development of L1-SPIRiT[50]. In this dissertation, we will reconstruct images using the L1-SPIRiT technique which is a combination of PI and CS.

2.1.5 Deep learning-based MR Image Reconstruction

Image acquisition can be significantly shortened with fast and advanced imaging techniques such as PI, CS and SMS. However, these advanced image reconstruction techniques rely on iterative algorithms such as non-linear conjugate gradient to recover the images which is time-consuming. As such, these reconstructions are typically performed off-line and do not provide rapid feedback to CMR technicians and physicians. Moreover, for the CS-based image reconstruction algorithm, the need for parameter tuning can be problematic.

Thus, a faster image reconstruction technique instead of an iterative reconstruction, is essential to facilitate clinical translation especially for non-Cartesian imaging. Recently, convolutional neural networks (CNN) have been playing an important role for image denoising tasks in computer vision field. As for advanced CS-based MR image reconstruction, the reconstruction process could be considered as a denoising process where

non-linear iterative process is involved. CNN, which has the non-linear mapping property, could be inherently deployed for CS-based MR image reconstruction.

As shown in Figure 2-6, with a pre-trained network, image reconstruction process is the feedforwarding process, which can be usually accomplished within a second, so that immediate feedbacks could be provided to doctors. Moreover, using deep CNN for CMR image reconstruction not only boosts reconstruction speed and simplifies parameter tuning, but also maintains high image quality. For non-Cartesian image reconstruction such as spiral imaging where the gridding processing is involved that further slows the reconstruction, the demand of fast reconstruction is more demanding. To date, recent advances in CMR image reconstruction using CNN[51–64] have been proposed, but most of the works were based on Cartesian imaging and the application of deep learning reconstruction for CMR spiral imaging and SMS imaging have been limited.

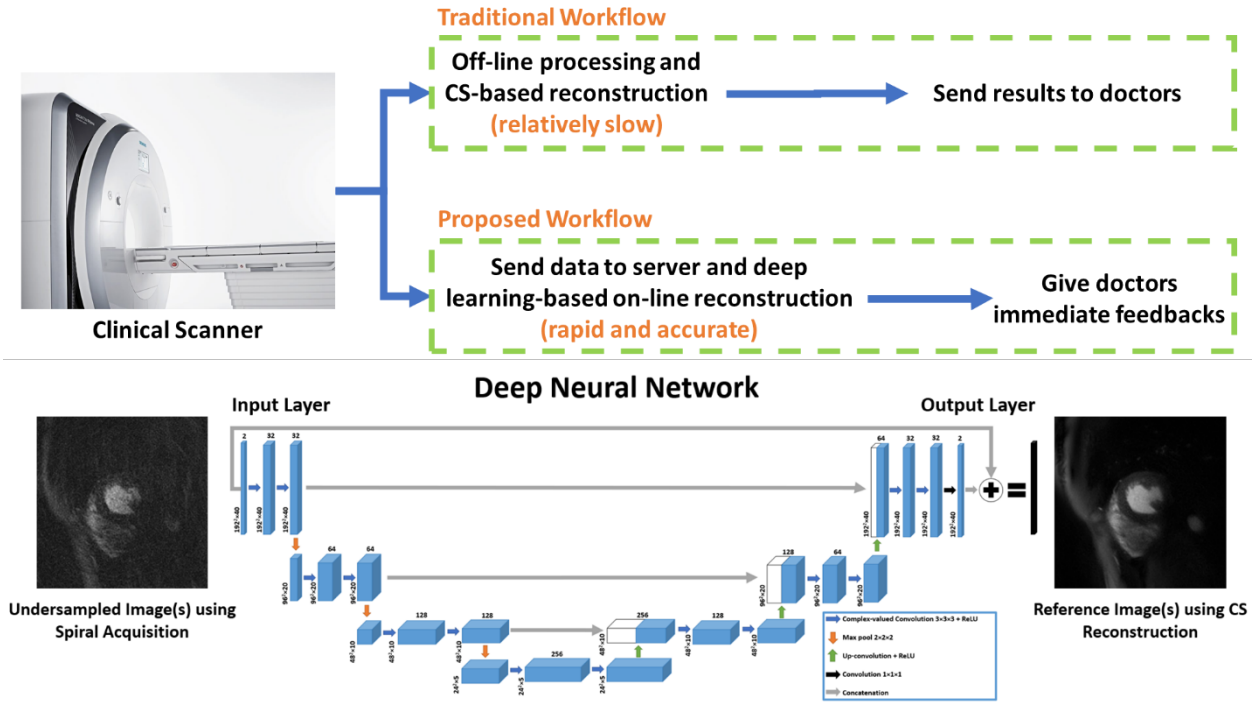

Figure 2-6. The deep learning-based image reconstruction and processing workflow. A 3D U-Net based image reconstruction network is shown.

The training for MR image reconstruction network can happen in image space and/or k-space. A straightforward data-driven network training process in image space is shown in Figure 2-6, which is supervised

learning, and the reference images are the CS-based image reconstructions. During the training process, the network parameters are updated with chain rule, to learn the mapping function from the undersampled images to the CS reconstructions. Ultimately, the network aims to generate results as close as the reference which could be reconstructions using CS or fully sampled images if possible. Therefore, this training can be considered as a regression process by minimizing the loss between network outputs and reference images.

Alternatively, unrolled networks[55,58,65–67] which decompose the iterative denoising and optimization process involved in CS reconstruction, take data fidelity as show in in Equation [2-4] into consideration, leading to the development of physics-driven image reconstruction. However, enforcing data fidelity is time consuming and memory consuming, which could be more severe for non-Cartesian imaging. The network could also be pre-trained and data fidelity is enforced only in the inference stage instead of the training stage[68].

Except for training a large denoising network, the efficacy of nonlinearity for CNN could be utilized to calibrate the GRAPPA kernels, resulting in a better image reconstruction performance[69]. This GRAPPA-based kernels could be further extended to calibrate through-plane kernels for SMS imaging[70].

2.1.6 Simultaneous Multi-slice Imaging

Simultaneous Multi-Slice (SMS) imaging employs complex RF-pulses together with parallel imaging coil arrays to acquire several sections along the z axis simultaneously, leading to a significant reduction in image acquisition time. To take advantage of parallel imaging acceleration, SMS imaging uses coil encoding together with either gradient or RF encoding to resolve data along the slice-select (z) axis.

A slice selective complex RF pulse can be described as the product of two functions[71]:

$$RF(t) = A(t) \times P(t) \quad \textbf{[2-5]}$$

where $A(t)$ is the standard complex RF waveform that in conjunction with the slice selective gradient determines the slice profile (e.g., a $sinc$ or hyperbolic secant), and $P(t)$ is an additional phase modulation function that determines the slice position ($\Delta\omega$) and its phase (ϕ) at TE=0 according to:

$$P(t) = e^{i\Delta\omega t+\phi} \quad \textbf{[2-6]}$$

The simplest way to obtain SMS excitation is to sum multiple RF waveforms with different $P(t)$ resulting in a multiband pulse that excites the desired slices in the presence of a common slice selective gradient. N arbitrary waveforms at arbitrary slice positions can be added up by complex summation to form a multiband pulse, as long as each pulse individually is consistent with the chosen slice selection gradient:

$$RF_{MB}(t) = A(t) \times \sum_{N} e^{i\Delta\omega_n t+\phi_n} \quad \textbf{[2-7]}$$

Design of SMS imaging pulses can also be challenging. As the number of simultaneous slices increases, the peak amplitude of the RF amplifier may be exceeded, and total pulse power may surpass specific absorption rate (SAR) limitations[71].

As shown in Figure 2-7, with single-slice acquisition, it is hard to achieve whole-heart coverage acquisition when the R-R interval in each heartbeat is short due to the increased heart rate. However, two or more slices could be acquired simultaneously by applying the phase modulation on the specific spiral interleaves used in SMS imaging. Typical phase modulation patterns are Hadamard[72] and CAIPIRINHA[73].

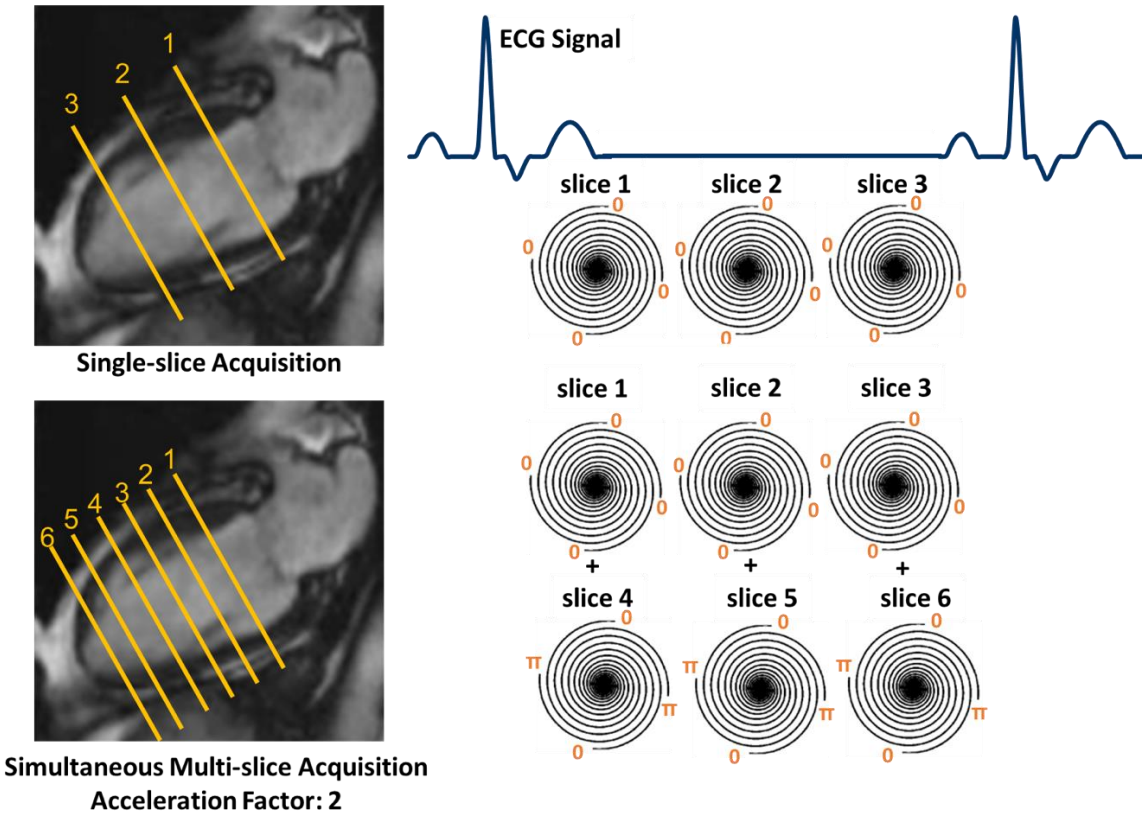

Figure 2-7. The single-slice and SMS acquisition. The Hadamard phase modulation pattern is applied on the specific spiral arms for SMS imaging with an acceleration factor of 2.

Unlike standard PI acceleration techniques, SMS acceleration results in little to no penalty in SNR. This is because neither the echo train length, number of phase-encoding steps, nor number of k-space samples has been reduced as occurs in conventional PI acceleration methods. Eddy currents due to rapid gradient switching may still create Nyquist-like ghosts that affect SMS images. Another artifact resulting in decreased imaging quality in SMS imaging is known as residual aliasing or slice leakage.

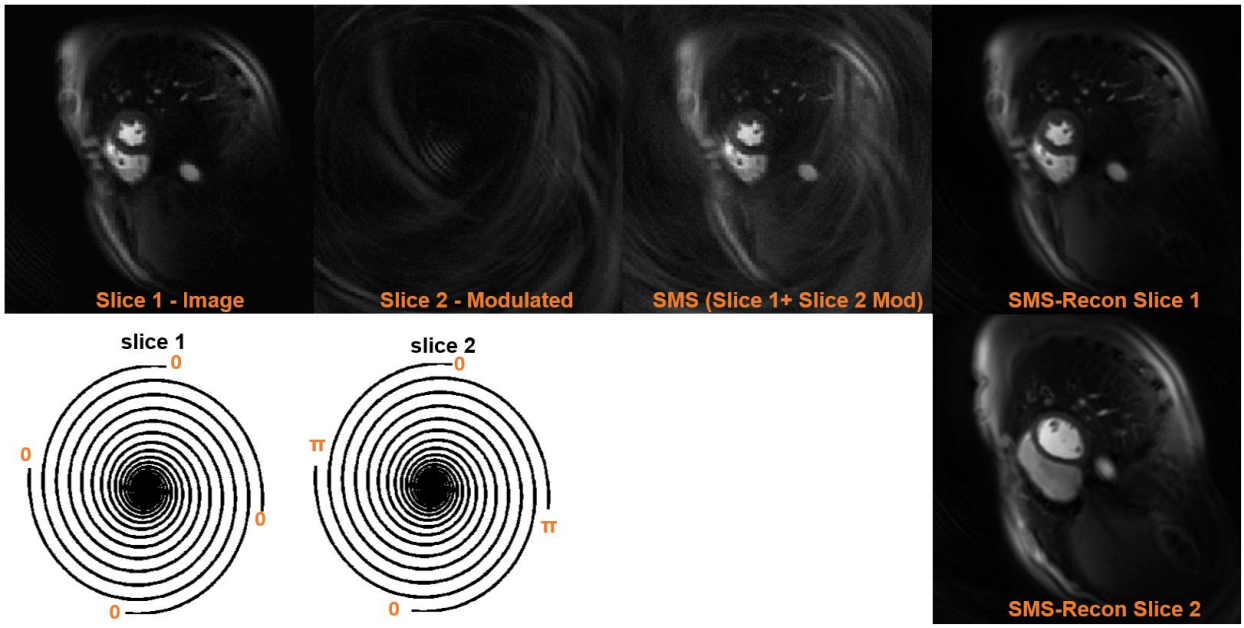

Figure 2-8. The SMS spiral perfusion imaging with an acceleration factor of 2 (i.e., two slices are acquired at the same time).

To recover image content at each slice location, phase demodulation and blocking the slice leakage from the interfering slice are necessary[74]. As illustrated in Figure 2-8, the phase-modulated image is the acquired data, and the image reconstruction is to recover the image content at each slice location with the slice leakage from the interfering slice as little as possible. However, with large amount of data rapidly acquired for cardiac dynamic imaging such as perfusion imaging, computation demand is high and image reconstruction time could be long.

2.1.7 Cardiac Magnetic Resonance Imaging Techniques

MRI provides excellent soft tissue contrast with no ionizing radiation exposure, which makes it well suited for cardiac imaging. Tremendous efforts have been made and have proven that CMR imaging can provide accurate assessment of cardiac morphology, function, perfusion, and myocardial viability.

Anatomic images of the heart and great vessels are a standard part of nearly every CMR examination. Such views are essential in patients with complex congenital malformations. In addition to conventional (axial, coronal, or sagittal views), several special oblique planes of imaging are routinely obtained for most cardiac studies. These may include long axis, short axis, and views of the valves, coronary arteries, and great vessels.

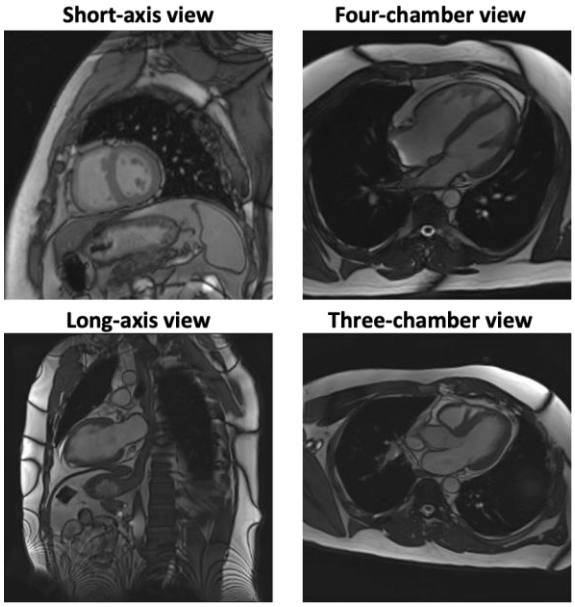

Figure 2-9. Different views for cardiac MR images.

Two types of sequences are commonly used for morphologic imaging - dark blood and bright blood. Both are typically performed at multiple slice locations during diastole, producing a stack of images covering the relevant anatomy in 5-6 mm sections. Dark blood sequences utilize inversion recovery (IR) preparation pulses to null the signal from blood alone or from both blood and fat. Bright blood sequences are typically based on balanced Steady-State Free Precession (bSSFP) methods, which reflect the relatively high T_2/T_1 ratio of blood[25].

SSFP-based bright-blood images of the beating heart are essential for displaying cardiac function. The motion of the ventricular walls during systole and diastole is of interest, which can be assessed qualitatively and quantitatively. Additional information about valve function is also possible. The turbulence created by valvular stenosis or insufficiency creates loss of signal in the bright blood which is related to its severity[25].

Cine studies are obtained by repeatedly imaging the heart at a single slice location throughout the cardiac cycle. Between 16 and 32 cardiac phases are usually sampled and displayed in a movie loop. Data collection takes place over multiple cardiac cycles using retrospective ECG-gating and breath-holding. In sick or uncooperative patients who have incapability of breath-holding, real-time cine images may be obtained in just a few seconds without breath-holding but suffer from decreased spatial and temporal resolution.

A typical left ventricular (LV) function study begins with single-slice cine images in two-chamber, three-chamber, and four-chamber views (Figure 2-9). This is followed by a stack of short-axis cine of eight to twelve slices perpendicular to the long axis of the LV spanning from the mitral valve to the apex throughout the cardiac cycle. These are usually obtained in multiple breath-holds with retrospective gating.

Total LV volumes are calculated by multiplying the cross-sectional areas in each short-axis slice by the slice thickness plus inter-slice gap (Simpson's rule). Global ventricular functional parameters generated by this process include[75]:

- End diastolic volume (EDV), largest volume of ventricular cavity during diastole (relaxation)
- End systolic volume (ESV), smallest volume of ventricular cavity during contraction (systole)
- Stroke volume (SV) = EDV−ESV, volume of blood displaced in a single heartbeat
- Ejection fraction (EF) = SV/EDV, percentage of blood displaced in a single heartbeat
- Cardiac output (CO) = SV × heart rate (beats per minute), total volume of blood displaced in a minute
- Cardiac index (CI) = CO / body surface area, cardiac output normalized to body surface area

Myocardial viability is assessed using gadolinium-enhanced imaging. The standard methods utilize segmented, T_1-weighted, inversion-prepared fast gradient echo sequences. The inversion time (TI) is chosen to null signal from myocardium, typically in the range of 300-350 ms at 1.5 T 8-10 minutes after contrast injection. Delayed enhancement, also called late gadolinium-enhanced imaging (LGE), is characteristic of subacute myocardial infarction, but also several other diseases[75].

Measurement of myocardial T_1 times (T_1 mapping) with Look-locker inversion recovery–prepared sequences may depict diffuse myocardial fibrosis and has good correlation with ex-vivo fibrosis content. T_1 mapping calculates myocardial T_1 relaxation times with image-based signal intensities and may be performed with standard cardiac MR imagers and radiologic workstations. The most two common T_1 mapping techniques are MOLLI[76] and SASHA[77]. Myocardium with diffuse fibrosis has greater retention of contrast material, resulting in T_1 times that are shorter than those in normal myocardium. Estimation of the extracellular volume

(ECV), which is a marker of myocardial tissue remodeling and provides a physiologically intuitive unit of measurement, requires measurement of myocardial and blood T_1 before and after administration of contrast agents as well as the patient's haematocrit value according to the formula[75]:

$$ECV = (1 - \text{haematocrit}) \frac{\frac{1}{post\ contrast\ myo\ T_1} - \frac{1}{native\ myo\ T_1}}{\frac{1}{post\ contrast\ blood\ T_1} - \frac{1}{native\ blood\ T_1}} \quad \textbf{[2-8]}$$

2.2 Coronary Artery Disease

Coronary arteries are the blood vessels that supply oxygen-rich blood to the heart muscle to keep it pumping[75]. The coronary arteries are on the epicardial surface of the heart. Myocardial blood flow is tightly coupled to oxygen demand. In non-diseased coronary vessels, whenever cardiac activity and oxygen consumption increases, there is an increase in blood flow that is nearly proportionate to the increase in oxygen consumption[75].

Coronary artery disease (CAD) is a narrowing or blockage of the coronary arteries usually caused by the buildup of fatty material called plaque in the wall of the vessel[75]. CAD is the most common type of heart Plaque is made up of cholesterol deposits. As shown in Figure 2-10, plaque buildup causes the inside of the arteries to narrow over time. This process is called atherosclerosis.

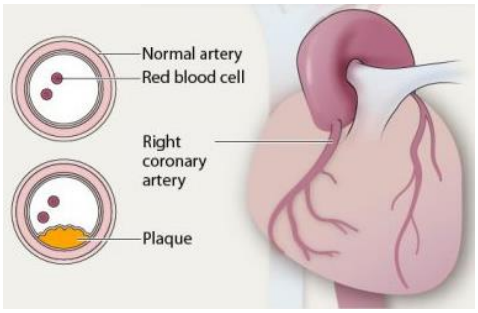

Figure 2-10. Coronary artery disease. Adapted from CDC website.

Obesity, physical inactivity, unhealthy eating, and smoking tobacco are risk factors for CAD. A family history of heart disease also increases the risk for CAD, especially a family history of having heart disease at an early age (50 or younger)[75].

In the US alone, CAD is responsible for 1 in every 7 deaths[2]. It is estimated that in the U.S. 18.2 million people have CAD[1] and 8.2 million suffer from angina pectoris with an expected 18% increase in the prevalence of CAD by 2030[2]. In terms of the economic impact, CAD was one of 10 most expensive hospital discharge diagnoses, accounting for over $10 billion in direct expenditures with a projected increase in cost of 100% by 2030[78]. Improvements in the accuracy of non-invasive functional assessment of CAD could significantly reduce health care costs resulting from unnecessary and expensive invasive procedures and revascularization. Thus, determination of the underlying cause of a patient's CAD syndrome and assessment of the myocardial blood flow and presence of myocardial scar in a fast and non-invasive way has important diagnostic, therapeutic and prognostic implications.

2.3 Diagnosis of Coronary Artery Disease

The CAD can be diagnosed by several ways[79], the details are shown below.

Test	What it Does
ECG or EKG (electrocardiogram)	Measures the electrical activity, rate, and regularity of your heartbeat.
Echocardiogram	Uses ultrasound (special sound wave) to create a picture of the heart.
Exercise stress test	Measures your heart rate while you walk on a treadmill. This helps to determine how well your heart is working when it has to pump more blood.
Chest X-ray	Uses x-rays to create a picture of the heart, lungs, and other organs in the chest.
Cardiac catheterization	Checks the inside of your arteries for blockage by inserting a thin, flexible tube through an artery in the groin, arm, or neck to reach the heart. Health care professionals can measure blood pressure within the heart and the strength of blood flow through the heart's chambers as well as collect blood samples from the heart or inject dye into the arteries of the heart (coronary arteries).
Coronary angiogram	Monitors blockage and flow of blood through the coronary arteries. Uses X-rays to detect dye injected via cardiac catheterization.
Coronary artery calcium scan	A computed tomography (CT) scan that looks in the coronary arteries for calcium buildup and plaque.

Table 2-1. Common methods of diagnosing CAD.

Currently, cardiac catheterization is the gold standard for defining obstructive CAD. Notably, a retrospective analysis of the National Cardiovascular Data Registry demonstrated that nearly 40% of the 398,987

patients without known CAD who underwent coronary angiography did not have significant CAD[80]. This implies that current strategies which are used to inform decisions regarding invasive angiography need to be substantially improved to increase the diagnostic yield of cardiac catheterization in routine clinical practice. This procedure is not only invasive but is also expensive.

Besides the invasive methods, non-invasive techniques including single-photon emission tomography (SPECT), positron emission tomography (PET), myocardial contrast echocardiography (MCE), cardiac MRI and cardiac computed tomography (CT) have been used to non-invasively assess myocardial perfusion in patients with known or suspected CAD. Each imaging modality has its own advantages and limitations. For example, SPECT myocardial perfusion imaging (MPI) is the most common stress test performed in the US, accounting for over 80% of the stress tests performed. The technique is based on the flow or metabolism dependent selective uptake of a radioactive tracer by functional myocardial tissue. SPECT MPI has been extensively studied and validated, and its advantages include compatibility with multiple stress modalities, and a relatively high SNR with longer data collecting time[81]. However, it also has several limitations including the use of ionizing radiation, poor spatial resolution, and sensitivity to motion and attenuation artifacts. Furthermore, conventional SPECT MPI techniques only detect obstructive CAD by identifying regional differences in relative myocardial perfusion. Due to the poor spatial resolution, SPECT cannot reliably detect the diffuse perfusion abnormalities in microvascular disease (MVD). Of note, PET and CMR have higher accuracy for detecting CAD than SPECT[82].

Fractional flow reserve (FFR), an index of the physiological significance of a coronary stenosis, is defined as the ratio of maximal blood flow in a stenotic artery to normal maximal flow[75]. CMR contrast enhanced first-pass myocardial perfusion imaging is highly accurate for diagnosing CAD as compared to the invasive functional gold standard of FFR. In fact, in a recent randomized clinical trial, a CMR perfusion guided strategy was non-inferior to an invasive-FFR guided approach for revascularization with similar rates of adverse cardiac outcomes[83]. Thus, CMR has become an important tool for diagnosing CAD.

2.4 Evaluation of CAD using Quantitative CMR Myocardial First-pass Perfusion Imaging

CMR myocardial first-pass perfusion imaging is based on the first pass of a bolus of gadolinium-DTPA contrast agents to assess myocardial perfusion. CMR has the advantages of non-ionizing radiation, flexible imaging plane orientation, excellent soft tissue contrast and higher spatial resolution. The higher spatial resolution can resolve transmural differences in myocardial perfusion which could potentially help differentiate MVD from obstructive CAD[84].

Because perfusion is affected early in the ischemic cascade, assessments of coronary perfusion reserve under stress has a higher sensitivity in detecting flow limiting stenosis than analysis of stress-induced wall motion abnormalities. Quantification of myocardial perfusion using CMR has been an active research area in the past two decades, and it is performed both at stress and rest to calculate absolute myocardial blood flow (ml/min/g) and myocardial perfusion reserve which is the ratio of the stress flow and rest flow that inversely correlates with stenosis severity provides an assessment of the functional impact of increasing stenosis severity[75].

The underlying principle of first-pass myocardial perfusion MR imaging is that differences in blood flow to the myocardium can be tracked by the direct visualization of enhancement with gadolinium contrast agents. The diagnosis of myocardial ischemia or infarction is based on its lower blood flow, recognized by slower rates of both uptake and washout of contrast material during the first pass through the myocardial circulation[75]. Most cardiac perfusion sequences are T_1-weighted fast gradient echo sequences or echo planar sequences performed with magnetization preparation to improve image contrast. A typical perfusion procedure is depicted in Figure 2-11.

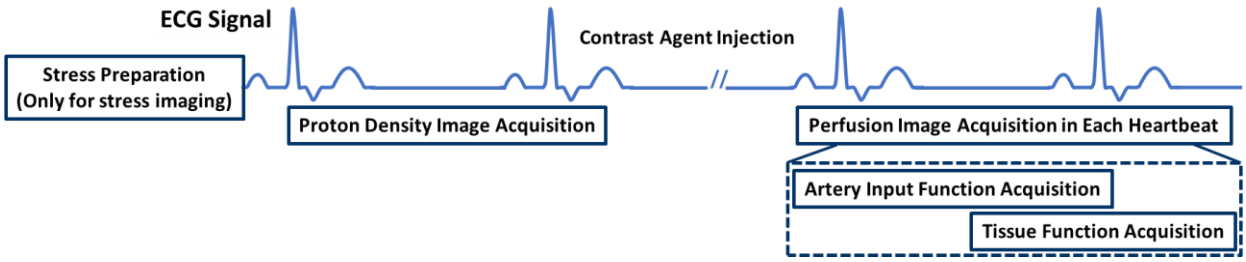

Figure 2-11. A typical quantitative perfusion imaging procedure.

For analysis of first-pass myocardial perfusion images, the muscle and cavity of the left ventricle can be divided into a variable number of segments. Based on autopsy data, the American Heart Association recommends a division into 17 segments[85] for the regional analysis of left ventricular function or myocardial perfusion (Figure 2-12). Interpretation is based on the expected coronary artery distributions for the segments. Analysis of perfusion imaging could be qualitative, semiquantitative, and fully quantitative (Figure 2-13).

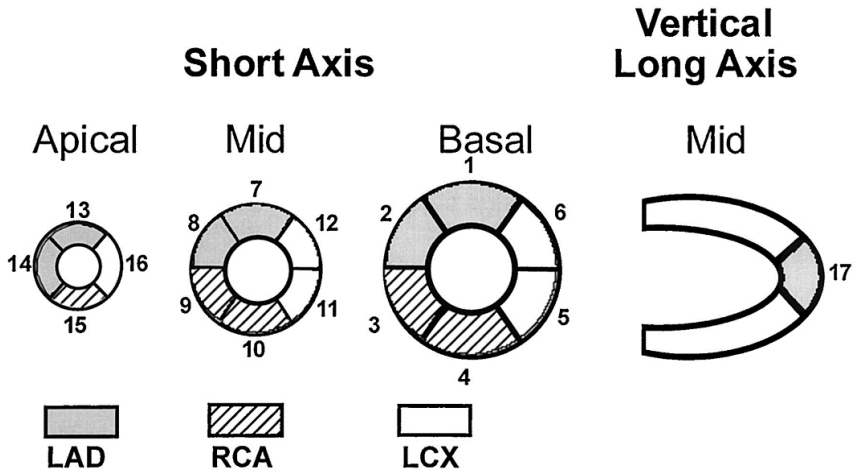

Figure 2-12. AHA 17-segment model. LAD: left anterior descending; RCA: right coronary artery; LCX: left circumflex.

The simplest form of analysis is a visual assessment of perfusion defects. Localized coronary artery disease first manifests as subendocardial hypoperfusion, as shown in Figure 2-14. Qualitative and semi-quantitative methods of interpretation rely on the differentiation of normally perfused areas from hypoperfused regions to diagnose ischemic heart disease based on compartmental models and established tracer kinetic techniques[86,87]. Challenges to these approaches include the derivation of gadolinium contrast concentrations from signal intensity measurements (Figure 2-15) and the stability of computational algorithms such as deconvolution. Nonetheless, quantitative measurements have the potential of improved sensitivity for the detection of changes in perfusion, particularly in the setting of global hypoperfusion. Quantitative perfusion measurements may prove useful markers for studying the effects of therapeutic interventions. To perform quantification of myocardial perfusion, an accurate measurement of the arterial input function (AIF), which can

be derived from the signal intensity-time curve in the left ventricular (LV) cavity, showing the variation of signal intensity in the blood pool is necessary[87].

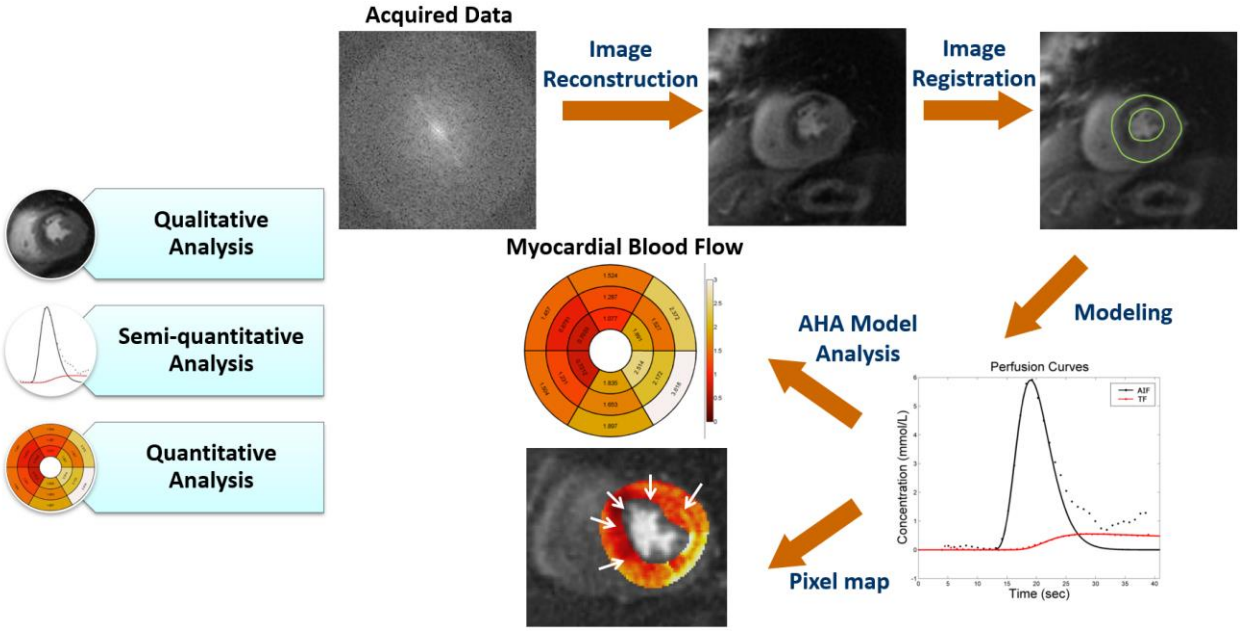

Figure 2-13. The perfusion imaging analysis pipeline.

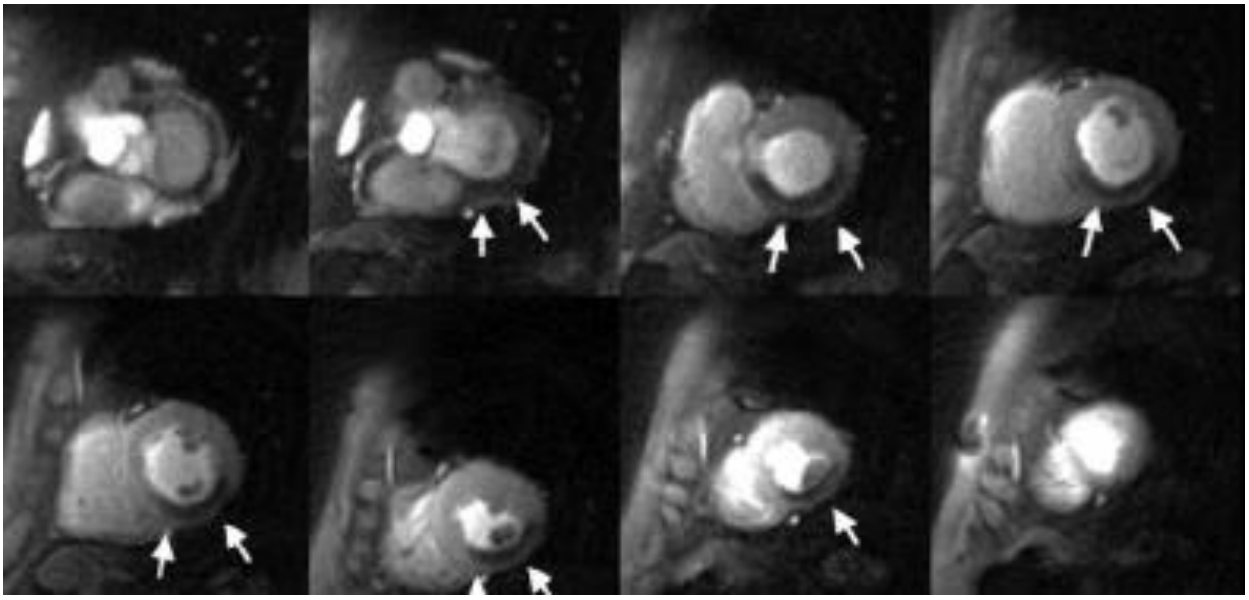

Figure 2-14. Spiral stress perfusion images demonstrate a subendocardial perfusion defect (arrows) in the inferior wall[14].

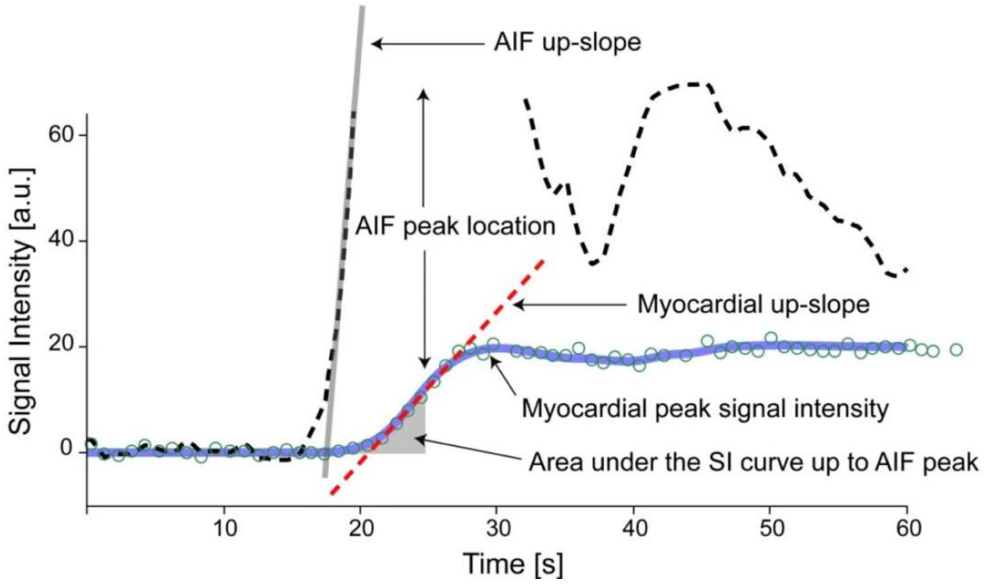

Figure 2-15. The characteristics of myocardial contrast enhancement[87].

Qualitative stress myocardial perfusion imaging using CMR has been demonstrated robust diagnostic and prognostic performance in several studies[88,89]. High resolution quantification of MBF with whole-heart coverage has the potential to provide unique information to improve the diagnosis of three-vessel disease and microvascular disease in comparison to simple qualitative evaluation[90–92]. A direct comparison of quantitative versus qualitative CMR perfusion was conducted by Patel et al in patients with suspected myocardial ischemia using quantitative coronary angiography as the comparative standard[93]. Although overall there was no significant difference in accuracy for the diagnosis of CAD, the quantitative method differentiated single-vessel disease from multivessel disease which has important implications for assessment of prognosis and therapeutic decision making.

2.5 Quantitative CMR Spiral Perfusion Imaging with whole-heart Coverage

It is essential to improve the spatial-temporal resolution of myocardial first-pass perfusion imaging. However, current clinically available techniques have limited in-plane spatial resolution (~2-2.5 mm) and incomplete heart coverage, which impede the assessment of transmural perfusion differences and underestimate the extent of ischemia. Furthermore, motion-induced dark-rim artifacts can significantly reduce image quality and limit evaluation of the sub-endocardium, which is most sensitive to myocardial ischemia[7].

Spiral acquisitions, which are fast and robust to motion artifacts, provide advantages for myocardial first-pass perfusion imaging. Spiral trajectories may also be less sensitive to dark-rim artifacts that are caused, at least in part, by cardiac motion.

By careful consideration of the spiral trajectory readout duration, flip angle strategy, and image reconstruction strategy, spiral artifacts could be mitigated to create high-quality first-pass myocardial perfusion images with high SNR, Salerno et al designed interleaved spiral pulse sequences for first-pass myocardial perfusion imaging and to evaluate them clinically for image quality and the presence of dark-rim, blurring, and dropout artifacts[94]. Furthermore, Salerno et al developed and evaluated variable-density spiral first-pass perfusion pulse sequences for improved efficiency and off-resonance performance and to demonstrate the utility of an apodizing density compensation function (DCF) to improve SNR and reduce dark-rim artifact caused by cardiac motion and Gibbs Ringing[95]. Subsequently, Yang et al developed CMR quantitative spiral perfusion techniques for both single-slice (SS) and simultaneous multi-slice (SMS) acquisitions enabling whole-heart coverage (6-8 slices) with high spatial resolution (2×2 mm^2)[8,9]. Our lab has developed novel motion-compensated CS-based L1-SPIRiT reconstruction techniques, that correct for breathing motion and enable free-breathing acquisition[8]. Sampling efficiency could also be improved by using outer-volume suppression (OVS) technique to achieve a reduced field-of-view (rFOV) so that the sampling in k-space can be coarser[10]. Yang et al applied an OVS technique for single-shot spiral perfusion imaging and demonstrated that it produced superior image quality as compared with full-FOV acquisitions[11]. To conduct quantitative analysis for perfusion imaging, our lab has also developed a quantification pipeline for spiral perfusion imaging to quantify myocardial blood flow and myocardial perfusion reserve (MPR). High diagnostic accuracy of the proposed techniques has been demonstrated as well[12–14].

However, achieving high resolution comes at the cost of a significant SNR penalty. To overcome the SNR limitation imposed by the higher spatial resolution, in this dissertation, we developed and implemented spiral perfusion techniques at 3 T. Additionally, one significant barrier to clinical translation of these techniques is the need for off-line reconstruction and quantification which currently takes hours to complete, and thus can't provide data to physician in a clinically acceptable time frame. To overcome this, a deep learning-based rapid

and accurate image reconstruction technique is also proposed. In order to further advance the clinical adoption of myocardial first-pass perfusion imaging, high-resolution Cartesian perfusion imaging with deep learning-based image reconstruction is also proposed.

Chapter 3: High Spatial Resolution Spiral Perfusion Imaging at 3 T

3.1 Introduction

First-pass contrast-enhanced cardiac magnetic resonance (CMR) perfusion imaging has proven to be a valuable tool for evaluating patients with known or suspected CAD[3–6]. However, current CMR perfusion imaging techniques still have limited spatial-temporal resolution and ventricular coverage. Over the past few years, developments in fast imaging techniques including non-Cartesian imaging[8,9,11,94–97], parallel imaging[43–45] and compressed sensing[49] have improved spatial-temporal resolution and enabled whole-heart imaging. 3D perfusion imaging techniques[34,98] have also been successfully applied. However, most still have either limited spatial-temporal resolution or spatial coverage.

Recently, we have developed a rapid interleaved single-slice (SS) spiral perfusion pulse sequence using a motion-compensated L1-SPIRiT reconstruction with 2×2 mm^2 in-plane resolution at 1.5 Tesla (T) [8]. To achieve whole-heart coverage and minimize motion artifacts, the acquisition window for each group of 2 slices following a saturation recovery RF pulse is short (<50 ms), limiting the maximum possible signal-to-noise ratio (SNR) that can be achieved at a given spatial resolution. We have also proposed utilizing simultaneous multi-slice (SMS) excitation to increase the acquisition time per slice and have developed a motion-compensated spiral SMS-L1-SPIRiT reconstruction technique at 1.5 T[9]. Sampling efficiency can also be improved by using outer-volume suppression (OVS) technique to achieve a reduced field-of-view (rFOV) so that the sampling in k-space can be coarser[10]. We have previously applied an OVS technique for single-shot spiral perfusion imaging and demonstrated that it produced superior image quality as compared with full-FOV acquisitions[11]. Overall, whole-heart coverage with an in-plane spatial resolution of 2×2 mm^2 were achieved at 1.5 T scanners using the aforementioned spiral perfusion techniques. Recent radial and Cartesian perfusion studies at 3 T have utilized an in-plane resolution of around 1.5-2 mm[99–103]. However, with higher spatial resolution there is increased ability to detect transmural perfusion differences between the epicardium and the endocardium, which could improve the ability to detecting obstructive CAD as demonstrated in prior studies[15–18]. Recent advance in high-resolution SMS Cartesian perfusion imaging utilizing bSSFP provides another possibility for high-resolution perfusion

imaging[104]. However, bSSFP could have significant banding artifacts at 3 T without using frequency scouts and requires a special phase cycling compatible with both bSSFP and SMS.

With a high in-plane spatial resolution of 1.25×1.25 mm^2, the sensitivity to detect perfusion differences between the endocardium and epicardium may be improved as compared to techniques with lower spatial resolution. Also, dark-rim artifacts which mimic subendocardial perfusion defects can be reduced by reduced Gibbs-ringing at higher spatial resolution[105]. However, achieving this high resolution comes at the cost of a significant SNR penalty. In this study, we sought to design a spiral acquisition technique to achieve a spatial resolution of 1.25×1.25 mm^2 with whole-heart coverage. To overcome the SNR limitation imposed by the higher spatial resolution, we developed and implemented spiral perfusion techniques at 3 T.

We further optimized the spiral perfusion pulse sequences and corresponding reconstruction techniques for both SS and SMS acquisitions with or without OVS to address the higher undersampling factors required to achieve this spatial resolution with high temporal resolution and whole-heart coverage. Particularly, for SMS acquisitions, we developed the motion-compensated SMS-Slice-L1-SPIRiT reconstruction technique which incorporates split-slice-GRAPPA-like kernels[106] for spiral imaging that could reduce the slice leakage and improve image quality[107,108]. The proposed techniques were evaluated in volunteers and patients undergoing clinically ordered CMR studies.

3.2 Methods

3.2.1 SNR Considerations

Achieving high resolution intrinsically limits the achievable SNR. For gradient-echo based spiral perfusion sequences, the SNR expressed in terms of the field strength, spatial resolution, readout duration, flip angle (FA) and the effect of saturation recovery (SR) time can be expressed as:

$$SNR \propto \eta \times B_0 \times \delta_{xyz} \times \sqrt{T_{total}} \times (1 - E_s) \times sin(\theta_c) \times C \quad \textbf{[3-1]}$$

where η is the SNR efficiency of variable-density spiral trajectory, B_0 is the static magnetic field strength, δ_{xyz} is the voxel volume, T_{total} is the total readout time per slice, E_s is e^{-TS/T_1} that characterizes the SR effects

where TS is the saturation time, θ_c is the FA that drives constant transverse magnetization during each spiral acquisition[94], and C is a constant that depends on the proton density, relaxation times (T_1 and T_2^*), and the other sequence parameters.

Increasing the in-plane resolution from 2×2 mm^2 to 1.25×1.25 mm^2 would result in a ~60% loss of SNR without changing any other acquisition parameters. Hence, we aimed to optimize other sequence parameters so that the SNR of the 1.25×1.25 mm^2 resolution technique at 3 T would be comparable to the SNR of the 2×2 mm^2 resolution technique at 1.5 T for which we have previously successfully implemented and validated for spiral stress perfusion imaging[8,9].

As we have demonstrated previously, the constant FA that balances the loss in magnetization from each excitation RF pulse[94], assuming an ideal slice profile, for a given TR, TS, and T_1 to ensure the transverse magnetization evolution is the same for each spiral arm can be expressed as:

$$\theta_c = cos^{-1}\left(\frac{E_1 - E_s}{E_1(1 - E_s)}\right) \quad \textbf{[3-2]}$$

where $E_1 = e^{-TR/T_1}$ and $E_s = e^{-TS/T_1}$.

Assuming a pre-contrast T_1 is 1160 ms[109], and a gadolinium concentration of 1 mmol/L with a relaxivity[110] of 3.6 L×mmol^{-1}×s^{-1}, the post-contrast T_1 would be roughly 224 ms. With TS = 120 ms, TR = 8 ms, the optimal FA would be 18° for a standard SR and SMS acquisitions. Alternatively, as we have shown previously, a slice-interleaved approach for SS perfusion imaging can be used which results in an effective TR of 2 TR for each slice[8]. In this case the effective TR would be 16 ms, resulting in an optimal FA of 26° (Figure 3-1).

The SNR should roughly double with the increase of field strength from 1.5 T to 3 T based on the increase in the net magnetization. However, the readout time for each spiral arm needs to be shortened at 3 T relative to 1.5 T to minimize off-resonance artifacts caused by field inhomogeneities. As we have previously shown that the limit for 1.5 T in terms of readout duration that does not have significant drop-out off-resonance artifacts is around 8 ms[111], we chose a readout duration of 4 ms for our experiments at 3 T[112].

As seen in Figure 3-1, when all these factors are considered together, the 3 T high-resolution interleaved SS and SMS acquisitions would have an SNR of roughly 91% and 91% respectively as compared to our previously validated 2×2 mm^2 technique at 1.5 T. Thus, the increase in field strength should compensate for the loss in SNR from the higher resolution and shorter spiral readout durations, making whole-heart high-resolution perfusion imaging feasible.

3.2.2 Pulse Sequences

To perform a comprehensive evaluations of different acquisition strategies for spiral perfusion at 3 T, two different factors were assessed: (1) slice-interleaved SS versus SMS acquisition and (2) acquisition of data with or without OVS. Four sequence variants were utilized in this study: SS without OVS (SS w/o OVS), SS with OVS (SS w/ OVS), SMS without OVS (SMS w/o OVS), and SMS with OVS (SMS w/ OVS).

For both SS and SMS acquisitions, a non-selective saturation with an optimized hard-pulse train for T_1-weighted preparation[113] and a spectrally selective adiabatic inversion recovery pulse (SPAIR) for fat suppression were used (Figure 3-1).

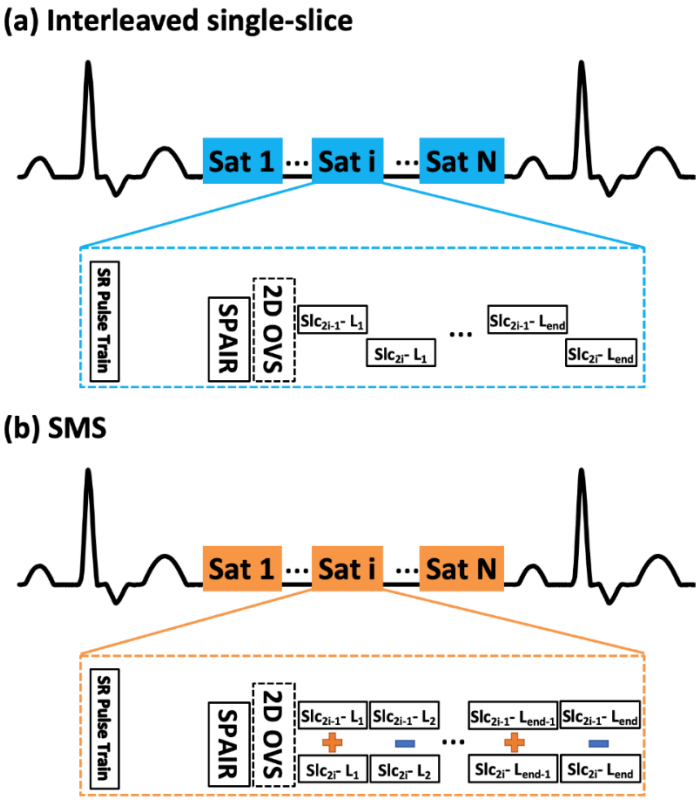

Figure 3-1. Pulse sequences for the interleaved SS (a) and SMS (b) spiral perfusion imaging. Specifically, (b) shows the acquisition scheme for MB=2. The OVS module was utilized only for OVS acquisitions.

For acquisitions using OVS, the OVS module was applied after the SPAIR pulse. The OVS module consisted of an adiabatic nonselective BIR-4 tip-down RF pulse with parameters optimized for 3 T performance, followed by a 2.2-ms spatially selective spiral tip-back RF pulse and a spoiler module as previously described for single-shot spiral perfusion imaging[11]. The BIR-4 pulse that was utilized for the OVS module was lengthened from 4 ms at 1.5 T to 5.12 ms at 3 T to reduce SAR, and the shape parameters were optimized to minimize B_0 and B_1 sensitivity over a ±200 Hz range of off-resonance frequencies. For OVS acquisition, the k-space trajectory was modified to support a nominal FOV of 170×170 mm^2 (50% FOV reduction) to image only the region around the heart. The OVS pulse was designed to support a FOV of 80×80 mm^2. By reducing the excited FOV, OVS enables a coarser sampling of k-space and improved sampling efficiency which should lead to the reduction of aliasing from structures outside of the heart region. OVS was evaluated for the interleaved SS and SMS MB=2 experiments.

Acquisition Type	SS	SMS
FOV (mm)	340	340
Matrix size	272×272	272×272
Spatial resolution (mm)	1.25	1.25
Slice thickness (mm)	10	10
No. of spiral interleaves	4	8
Spiral readout per interleave (ms)	4.1	4.1
Saturation time (ms)	120	120
TR (ms)	8	8
Temporal sampling footprint (ms)	56	64
Highest possible heart rate (BPM)	108	108 (MB=2) 163 (MB=3)
Flip angle (degree)	26	18
Number of slices	6 or 8	6 or 8 (MB=2) 6 or 9 (MB=3)
No. of slices per saturation recovery	2	2 (MB=2) 3 (MB=3)
Spiral density type	dual density	dual density
Starting density (Nyquist)	1	2
Ending density (Nyquist)	0.05 (w/o OVS) 0.12 (w/ OVS)	0.10 (w/o OVS) 0.26 (w/ OVS)

Table 3-1. Detailed spiral pulse sequence parameters for both SS and SMS acquisitions.

To achieve high spatial resolution with a small number of spiral interleaves, significant k-space undersampling is required. Variable density spirals enable the center of k-space to be more densely sampled with significant undersampling of the higher spatial frequencies, which can result in an incoherent noise-like aliasing pattern that is potentially advantageous for a CS reconstruction[8]. We utilized dual density (DD) spiral trajectories with a Fermi-function shape for the transition region[9] for both SS and SMS acquisitions (Table 3-1). SS acquisitions utilized a slice-interleaved approach[9], where spiral arms from two slices were acquired in an

interleaved fashion following each saturation recovery (SR) pulse. Non-adjacent slices were acquired in each saturation block to reduce effects of crosstalk between slices. The same total sampling time for interleaved SS and SMS acquisition were kept constant at 64 ms (8 TR), allowing for the acquisition of 8 spirals per saturation pulse for both strategies. This means that each slice of the SS technique has 4 interleaves, while the SMS technique has 8 interleaves per slice.

For SMS acquisitions, MB RF pulse excitation pulses were designed by the summation of the slice-selective SS sinc RF pulses with Hadamard phase modulation[72] for each slice. The SS RF pulse was a 1 ms sinc-shaped pulse with a time-bandwidth product of 5.6[9]. Depending on different SMS factors, 2 (MB=2) or 3 (MB=3) slices were acquired in each SR block, and SR blocks were repeated until all the slices are imaged. In our experiments, 6-8 slices were acquired for MB=2 and 6-9 slices were acquired for MB=3 (Table 3-1). The number of acquired slices was based on both R-R duration and specific absorption rate (SAR) constraints.

Spiral interleaves were uniformly distributed in each heartbeat and were rotated by the golden angle (137°) between heart beats. This strategy was chosen to achieve temporal incoherence and also to permit a similar sampling strategy for both SMS acquisitions with Hadamard phase cycling of the interleaves in each heart-beat[9,72] and the interleaved SS acquisitions.

3.2.3 Image Reconstruction and Processing

Figure 3-2. The proposed motion-compensated L1-SPIRiT reconstruction technique for single-slice acquisition (a) and the motion-compensated SMS-Slice-L1-SPIRiT image reconstruction technique for SMS acquisitions (b). illustrates the image reconstruction and processing approach utilized in this study. SS and SMS images were reconstructed using a motion-compensated approach: (SMS-Slice-) L1-SPIRiT[8,107], which can be expressed as follows:

$$\underset{x}{argmin}||\Phi R F_u x - y||_2^2 + \lambda_1||(G_{SPIRiT} - I)x||_2^2 + \lambda_2||\Psi x||_1 + \lambda_3||(G_{TP} - I)x||_2^2 \qquad \textbf{[3-3]}$$

where x are motion-corrected multi-channel images to be reconstructed at each slice location, y is the acquired spiral SS or SMS data that might contain motion, F_u is an inverse Fourier gridding operator (NUFFT) that

transforms from Cartesian image space to spiral k-space[48], R is the motion-correction operator mapping the motion-corrected image series to the motion-corrupted image series, G_{SPIRiT} is an image-space SPIRiT operator for each slice[45], G_{TP} is an image-space through-plane (TP) operator which is calibrated by enforcing consistency on the desired slice and blocking the signal from the interfering slices to reduce slice leakage artifacts[107,108], Ψ is the finite time difference transform that operates on each individual coil separately enforcing sparsity in the temporal domain of perfusion image series, I is the identity matrix, λ_1, λ_2 and λ_3 are parameters that balance the data acquisition consistency with SPIRiT calibration consistency, temporal sparsity and slice consistency, and Φ is the SMS Hadamard phase modulation operator. For SS acquisition the same equation can be utilized by setting Φ to I and setting $\lambda_3 = 0$, which leads to the L1-SPIRiT reconstruction approach we have described previously[8]. Note that the Φ operator depends on the number of interleaves and the desired SMS factor, and when λ_3 is set to 0 the reconstruction becomes our previously proposed SMS-L1-SPIRiT reconstruction[9].

The slice-by-slice motion correction operator, R , was incorporated into the image reconstruction process to compensate for motion caused by imperfect breath-holding during acquisition[114]. As most of the motion resulting from breathing motion can be approximated using in-plane rigid shifts, the R operator was implemented as a linear phase shift in the k-space domain. In order to achieve robust motion correction in the setting of the dynamic signal intensity variation, images were registered to synthetic images derived by performing principal component analysis (PCA) in the temporal dimension so that images could be rigidly registered to a target frame that has consistent signal intensities[115].

The SPIRiT[45] and TP[107,108] operators for each slice were estimated using an auto-calibration approach so that the additional acquisition of calibration data was unnecessary. For SS, SPIRiT operators for each slice were estimated by temporally averaging the dynamic perfusion image series. This ensures that the training data is free of any aliasing artifacts. Specifically, for SMS acquisitions, the initial under-sampled images at each slice location were generated by performing NUFFT[48] on the phase demodulation data. The SPIRiT and TP operators were then generated from the temporally averaging image series for each slice (Figure 3-1Figure 3-2). Due to the large number of interleaves across the temporally averaged data and the Hadamard phase modulation strategy,

the interfering slices should have almost complete cancellation of signal allowing for the auto-calibration approach.

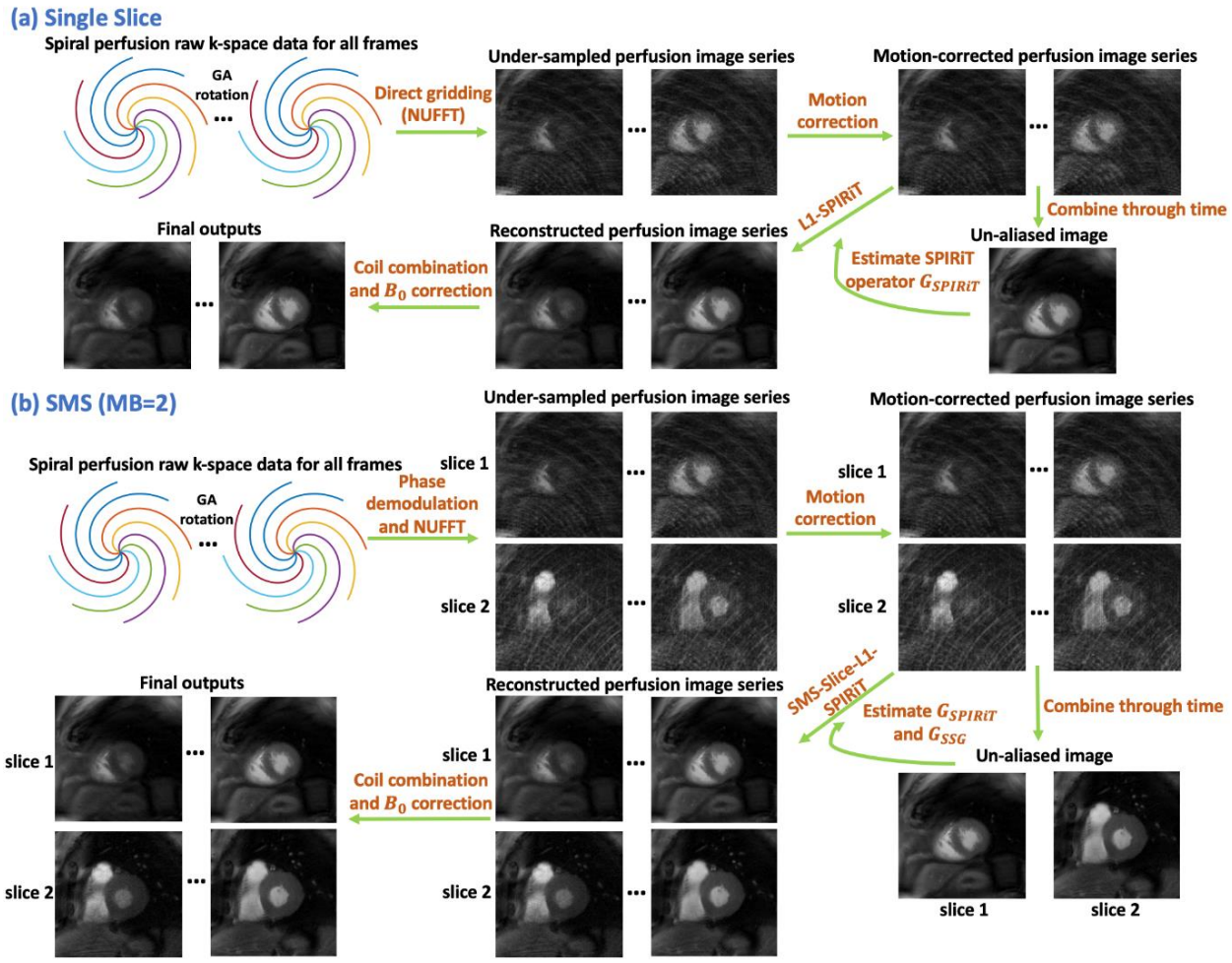

Figure 3-2. The proposed motion-compensated L1-SPIRiT reconstruction technique for single-slice acquisition (a) and the motion-compensated SMS-Slice-L1-SPIRiT image reconstruction technique for SMS acquisitions (b).

For SS acquisitions, dynamic perfusion image series were reconstructed slice by slice as described by Yang et al[8]. For SMS acquisitions, multiple slices for each SMS acquisition were reconstructed simultaneously and y was the phase-modulated k-space data for each SMS acquisition. $\lambda_1 = 1$ and $\lambda_2 = 0.4M_0$ where M_0 was the maximal magnitude value of the motion-corrected NUFFT images were selected for SS reconstructions based on the results of a retrospective experiment that balanced image quality and temporal fidelity as described by Feng et al[116]. The same regularization parameters were used for all reconstructions. For SMS reconstructions,

$\lambda_1 = 1$, $\lambda_2 = 0.5M_0$ and $\lambda_3 = 1$ were selected based on a similar criterion regarding image quality and temporal fidelity. The nonlinear iterative conjugate gradient descent algorithm[117] with 80 iterations was used to solve the optimization problem.

Additionally, prior to image reconstruction, coil selection was performed to retain coils with low artifact power and high SNR over the heart region as we have described previously[31]. Coil compression with a 5% tolerance[118] was performed to accelerate the reconstruction process. To enhance the image quality and minimize the artifacts caused by field inhomogeneities at 3 T, an automatic B_0 inhomogeneity correction method based on auto-focus[119] was performed after image reconstruction. B_0 inhomogeneity correction was performed on coil-combined complex images generated from the multi-coil reconstruction using the method described by Walsh et al [120].

The image reconstruction and processing were implemented in MATLAB (The MathWorks, Natick, MA). The image-based non-Cartesian reconstruction used Fessler's NUFFT code[48].

3.2.4 Retrospective Experiment

To test the newly proposed SMS-Slice-L1-SPIRiT reconstruction strategy, we reconstructed 10 simulated SMS MB=2 datasets using the same reconstruction parameters for both SMS-Slice-L1-SPIRiT and the SMS-L1-SPIRiT where TP kernels were not incorporated. Simulation data were retrospectively created by inverse gridding and phase-modulated addition of previously acquired high resolution SS perfusion datasets reconstructed using L1-SPIRiT with 1.25 mm resolution at 3 T which served as the ground truth. The reconstructed images of both methods were assessed quantitatively using the root mean square error (RMSE) and structural similarity index (SSIM)[121].

3.2.5 Human Studies

34 healthy volunteers and 8 patients undergoing clinically ordered CMR studies with gadolinium (Gd)-based contrast agents (Gadoteric acid - Gadoterate meglumine; Dotarem Guerbet or Clariscan GE Healthcare) were included in this study. The 13 healthy subjects underwent perfusion imaging during two separate

gadolinium injections separated by a 20-minute washout period, while the other 21 healthy volunteers and 8 patients underwent a single gadolinium injection. Overall, the studies in volunteers and patients resulted in 55 perfusion datasets for analysis. Of the 8 patients, 2 were for evaluation of myocarditis, 4 were for evaluation for heart failure/cardiomyopathy, 1 was for evaluation of hypertrophic cardiomyopathy, and 1 was for the evaluation of pericarditis. Written informed consent was obtained from all subjects using a protocol approved by the University of Virginia Health Sciences Research Institutional Review Board. Imaging was performed on 3 T MRI scanners (MAGNETOM Prisma/Skyra; Siemens Healthineers, Erlangen, Germany). Perfusion imaging was performed using 0.075 mmol/kg of contrast agent injected intravenously at a rate of 4 mL/s followed by 25 mL of saline flush at 4 mL/s. Subjects were asked to hold their breath as long as possible, followed by shallow breathing during the acquisition of perfusion images over 50 to 60 heartbeats.

3.2.6 Image Analysis

For the image quality assessment, each set of perfusion images were blindly graded on a 5-point scale (5, excellent; 1, poor) by 2 experienced cardiologists. The image quality grading was conducted independently by each of the two cardiologists, and their average score was computed.

To address the effects of the B_0 inhomogeneity correction, we randomly presented 10 cases with and without B_0 correction to a cardiologist who blindly reviewed the images side by side to choose the image set with less blurring. Ties were allowed if there was no difference in the visual appearance of blurring.

Additionally, one cardiologist also blindly evaluated the dropout severity of all different acquisitions (5, excellent; 1, poor).

3.2.7 Statistical Analysis

Normally distributed parameters are described by their mean and standard deviation, while non-normally distributed parameters are described using the median and interquartile range (IQR). For retrospective experiment evaluating the proposed SMS-Slice-L1-SPIRiT reconstruction technique, the normality of the SSIM and RMSE values were assessed using the Shapiro-Wilk test. As the visual scoring was graded on an ordinal

scale, a non-parametric Kruskal-Wallis test was used to test for differences between the techniques. Comparisons between individual imaging techniques were conducted using a Wilcoxon signed-rank test with Bonferroni correction for multiple comparisons. For all statistics a $p<0.05$ was considered statistically significant. Statistical analysis was performed using SAS software (version 9.4; SAS Institute Inc., Cary, NC).

3.3 Results

The retrospective multi-band reconstruction experiment demonstrated the proposed SMS-Slice-L1-SPIRiT had a higher SSIM (0.936±0.033 vs. 0.854±0.032, $p<0.05$) and lower RMSE (0.010±0.003 vs. 0.015±0.003, $p<0.05$) as compared to SMS-L1-SPIRiT for the SMS MB=2 acquisition without OVS. This improved performance was also confirmed by visual assessment of the prospectively acquired SMS MB=2 w/o OVS perfusion images which demonstrated average scores of 3.7±0.4 for the SMS-Slice-L1-SPIRiT reconstruction and 3.1±0.5 for the SMS-L1-SPIRiT reconstruction ($p<0.05$). SSIM and NRMSE for the retrospective experiments were normally distributed by Shapiro-Wilks test justifying the use of paired t-tests.

Figure 3-3 (a) shows an example case of SS acquisition without OVS from a clinical patient undergoing the resting perfusion with whole-heart coverage, which has an image quality score of 5 and minimal artifacts. Figure 3-3 (b) presents an example case for SMS MB=2 without OVS acquisition from a healthy volunteer undergoing the resting perfusion with whole-heart coverage. Good image quality was demonstrated with a score of 4 due to mild residual aliasing artifacts.

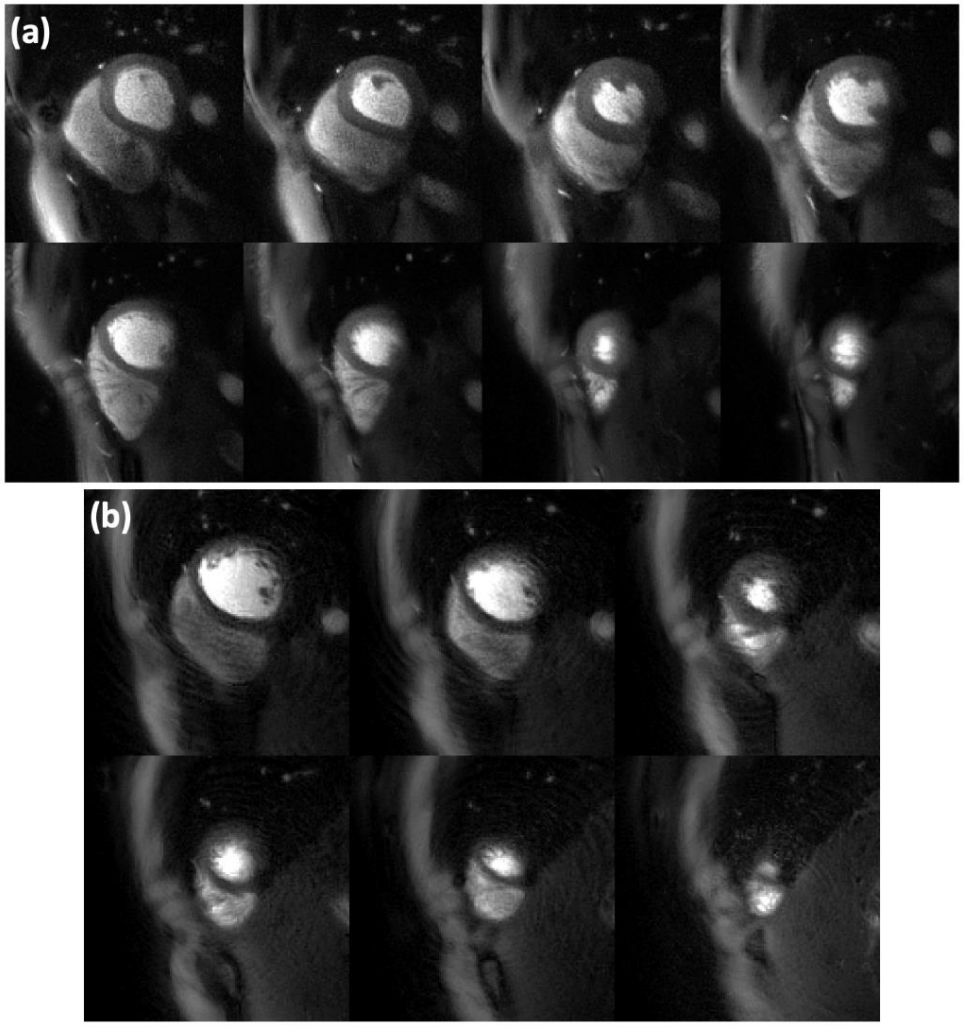

Figure 3-3. Example cases for SS w/o OVS acquisition (a) and SMS MB=2 w/o OVS acquisition (b). (a) shows an example case of SS w/o OVS spiral resting perfusion acquisition from a clinical patient with whole-heart coverage. Excellent image quality and minimal artifacts were demonstrated with an image-quality score of 5. (b) shows an example case of SMS MB=2 w/o OVS spiral resting perfusion acquisition from a healthy volunteer with whole-heart coverage. Good image quality was demonstrated with a score of 4. There is mild residual aliasing artifact.

Figure 3-4 shows a direct comparison of whole-heart resting perfusion imaging at a middle time frame using SS acquisition and SMS MB=2 acquisition with OVS from the same healthy subject. The image quality was higher for the interleaved SS acquisition than the SMS acquisition due to residual aliasing artifacts that can be seen in the SMS images. Overall, the image quality score of SMS acquisition with OVS was less than the SS acquisition with OVS.

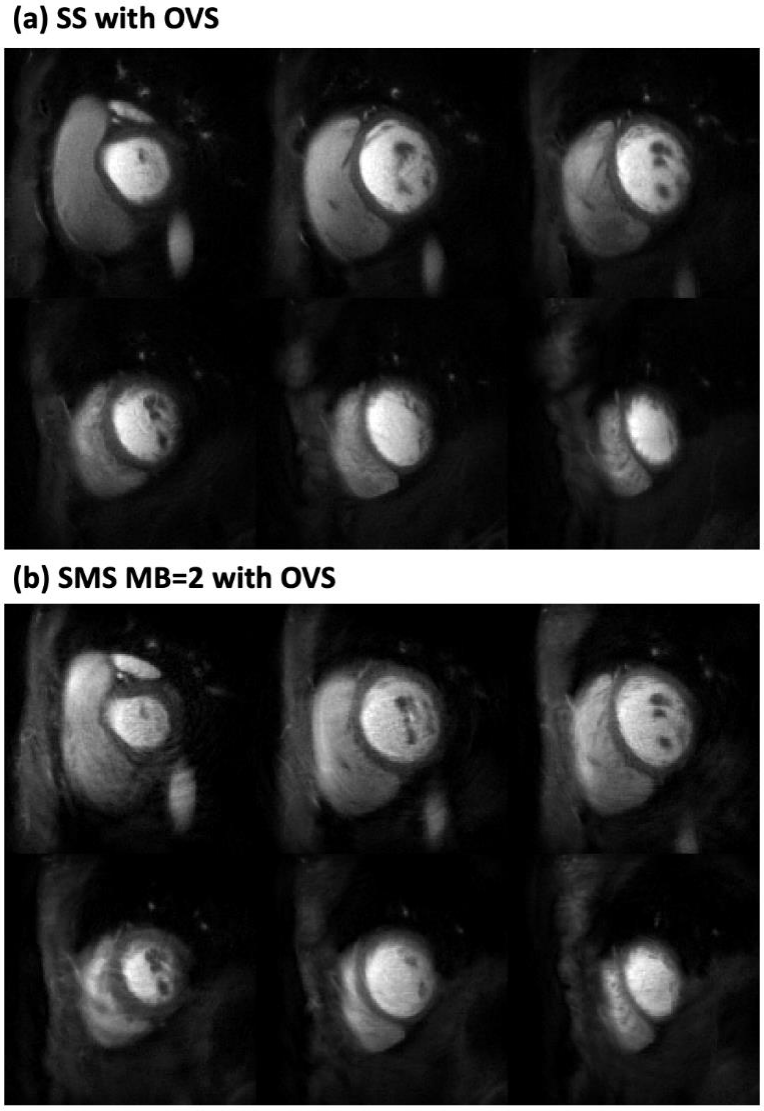

Figure 3-4. Direct comparison of whole-heart resting perfusion imaging at a middle time frame using SS acquisition (a) and SMS MB=2 (b) with OVS from the same healthy volunteer. Good image quality was demonstrated for OVS acquisitions for both SS and SMS MB=2. SS acquisition has a score of 4 and SMS MB=2 has a score of 3.5 due to more residual aliasing artifacts.

Figure 3-5 shows an example case of whole-heart perfusion imaging at a middle time frame using SMS MB=3 acquisition without OVS from a healthy subject. Mild, but noticeable residual aliasing artifacts can be visualized.

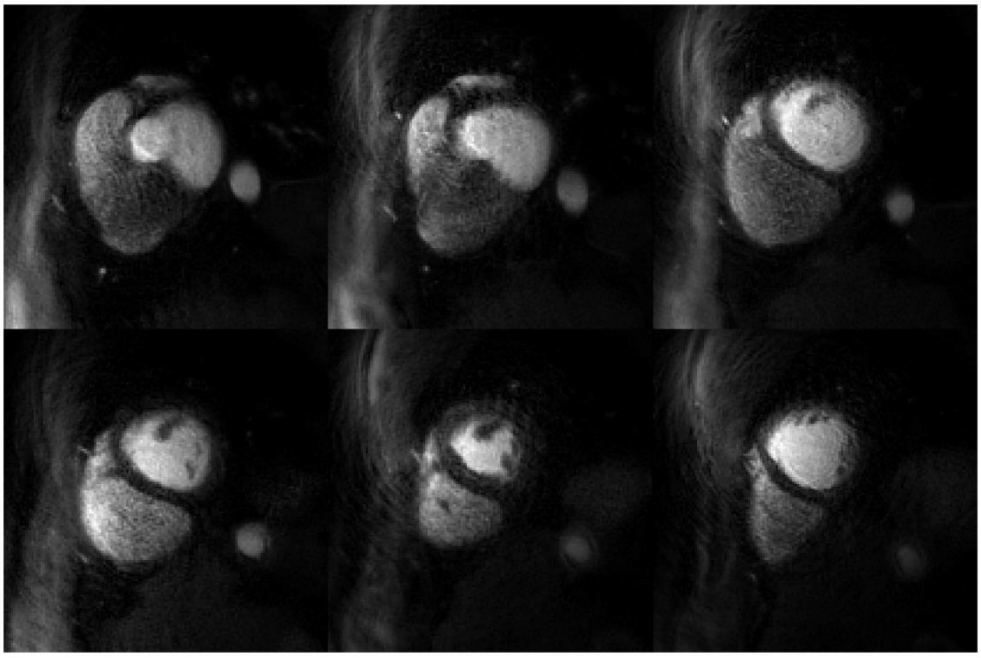

Figure 3-5. An example case of SMS MB=3 without OVS spiral resting perfusion acquisition from a healthy volunteer with whole-heart coverage. Good image quality was demonstrated with a score of 4.

To demonstrate the fidelity of temporal profile in myocardium, six segments in the myocardium from the American Heart Association (AHA) segmental model were selected from one of the slices presented in Figure 3, and the mean signal intensity of the (SMS-Slice)-L1-SPIRiT reconstruction was plotted through temporal frames as compared to the corresponding region from the undersampled NUFFT data from the same slice which is reconstructed without any temporal constraint (Figure 3-6). Signal intensity and temporal fidelity in the ROI from the reconstructed results demonstrate good agreement with the under-sampled data (NUFFT results), with preserved temporal fidelity of the myocardial signal.

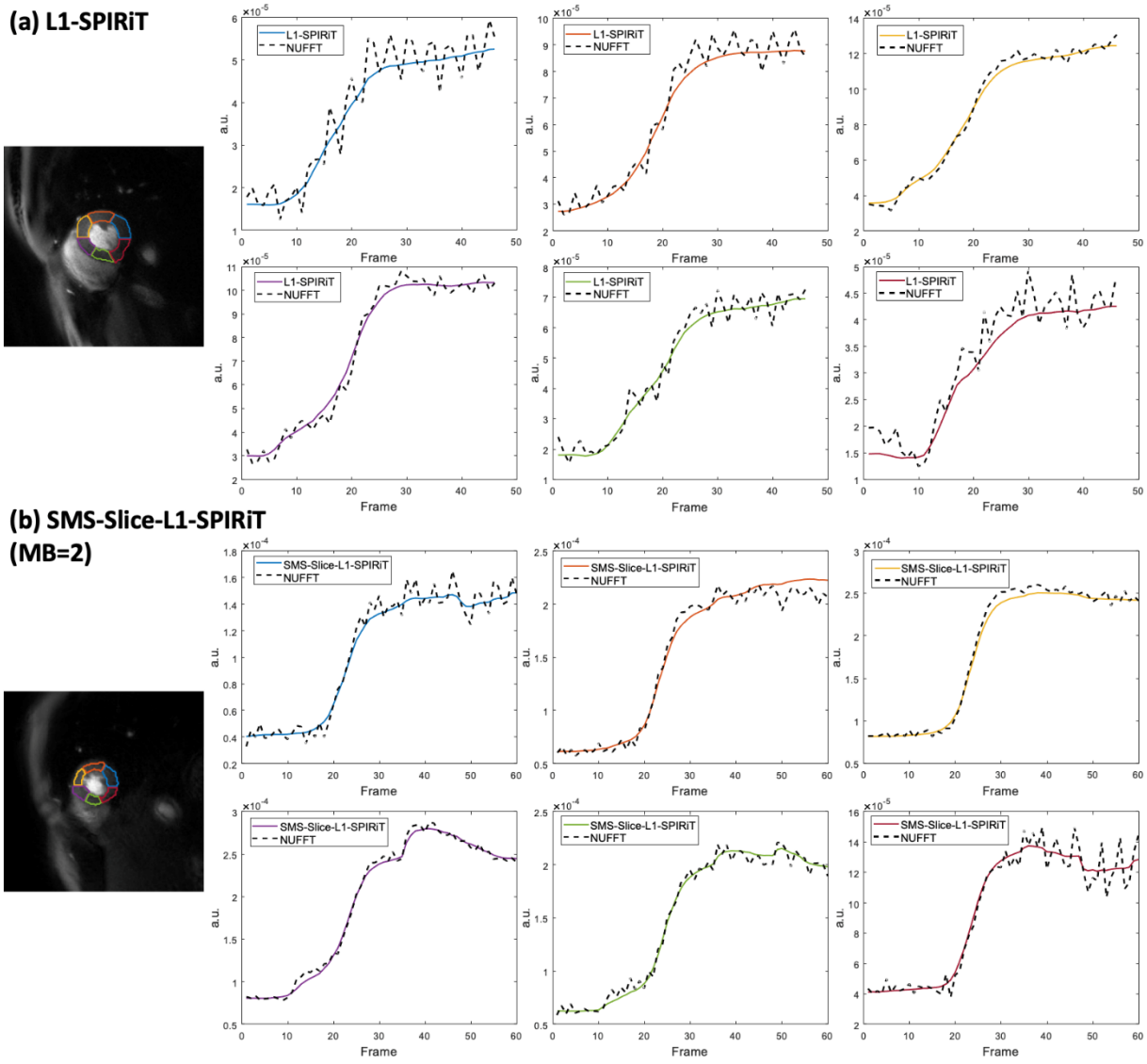

Figure 3-6. The temporal fidelity of the myocardium from one of the slices is shown in Figure 3-3. The signal is the mean value of the six segments in the myocardium based on the AHA segmental model. The reconstruction results demonstrate good temporal agreements with the under-sampled NUFTT reconstruction.

Given the short readout duration there were minimal off-resonance blurring artifacts. In some cases, there was blurring of the intracardiac structures such as the papillary muscles during maximal LV enhancement. Figure 3-7 demonstrates the performance of B_0 inhomogeniety correction for a SS acquisition without OVS. The images show reduced blurring particularly in the region of the papillary muscles which are within the LV cavity following B_0 inhomogeneity correction. These artifacts primarily affect the epicardial aspect of the inferolateral wall and can be differentiated from ischemia which primarily affects the sub-endocardium. 10 cases with or

without B_0 inhomogeneity correction was blindly evaluated by an experienced cardiologist, and 7 of 10 cases with B_0 inhomogeneity correction had superior image quality while the other 3 cases were considered to have similar degrees of blurring.

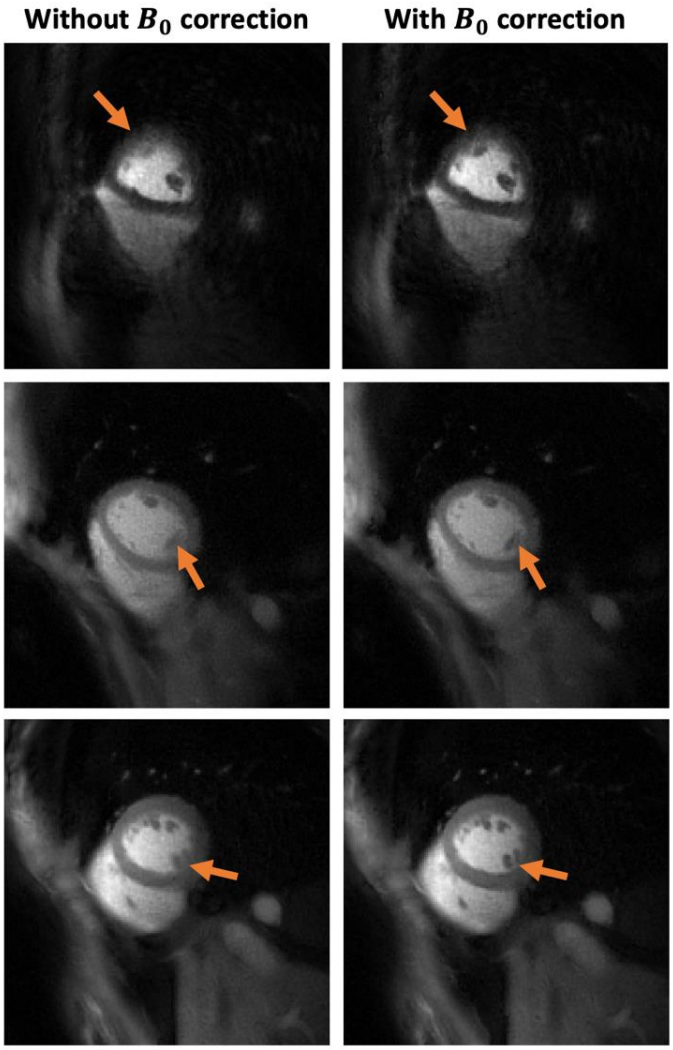

Figure 3-7. Utilization of the B_0 inhomogeneity correction compensates the artifact caused due to field inhomogeneity. For a SS without OVS acquisition from a healthy volunteer, (a) shows one of the frames before doing inhomogeneity correction and (b) shows the corresponding output after doing the correction.

Figure 3-8 presents the image quality scores for the different acquisition methods and the number of studies for each acquisition. SS w/o OVS acquisition has the highest image quality (4.5 [4, 5]),) while SS w/ OVS (3.5 [3.25, 3.75]) showed the lowest score ($p<0.05$). SS w/o OVS had a significantly higher image quality score than SS w/ OVS, SMS MB=2 w/ OVS and SMS MB=2 w/o OVS($p<0.05$). There was no significant

difference in visual image quality score among the SS w/o OVS, and SMS MB=3 w/o OVS (Figure 3-8). However, the point estimate was higher for SS w/o OVS.

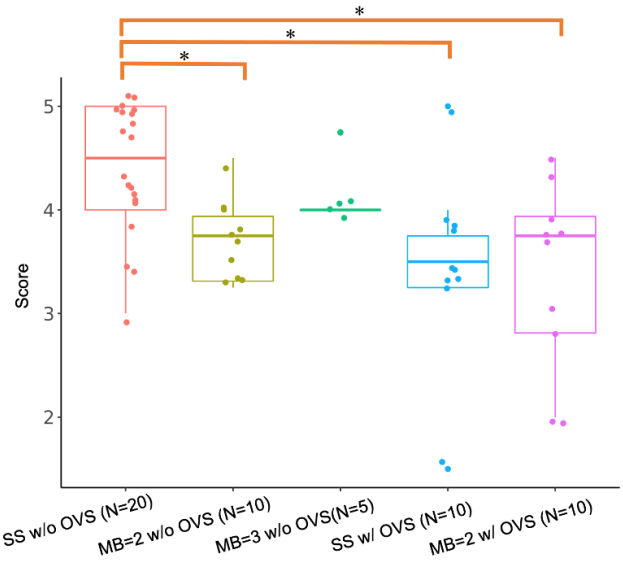

Figure 3-8. Image quality score for each acquisition method. Images were blindly graded by 2 experienced cardiologists (5, excellent; 1, poor). The scores shown is the average score from 2 cardiologists. *Indicates significant difference ($p < 0.05$). The number of studies involved in each acquisition method is denoted as the number of *N*.

The average drop-out score for SS w/o OVS, SMS MB=2 w/o OVS, SMS MB=3 w/o OVS, SS w/ OVS, and SMS MB=2 w/ OVS were 4.4, 3.8, 4.6, 3.8 and 3.9, respectively (5, excellent; 1, poor), which demonstrated the overall good reconstruction performance in terms of the drop out severity in the inferolateral wall.

3.4 Discussion

We demonstrate that high quality images of first-pass myocardial perfusion can be acquired using high-resolution whole-heart spiral perfusion techniques at 3 T for both SS and SMS acquisitions with or without OVS. Specifically, SS without OVS acquisition demonstrated the highest image quality. Given the high sampling efficiency of spiral imaging, an in-plane spatial resolution of 1.25×1.25 mm^2 was achieved over 6 to 8 slices with a temporal sampling footprint of 56 ms (7 TR) or 64 ms (8 TR) per slice for SS and SMS acquisitions, respectively. Recent studies using Cartesian and radial imaging at 3 T have either demonstrated lower spatial-temporal resolution or more limited spatial coverage than what is feasible using spiral trajectories[99–101]. The enhanced spatial resolution may increase the ability to assess transmural differences in myocardial perfusion[15–

[17], and the whole-heart coverage may improve the ability to assess the extent of ischemia and quantify the ischemic burden.

This work is an extension of our prior spiral perfusion sequence development for 1.5 T[8,9,11] whole-heart perfusion imaging. To have adequate SNR for perfusion imaging with high spatial resolution, we adapted the spiral acquisition and reconstruction techniques for 3 T. The same spiral trajectory and pulse sequence parameters was used for both 3 T MR systems used in our study (MAGNETOM Prisma/Skyra; Siemens Healthineers, Erlangen, Germany). Studies were performed on either scanner based on scanner availability and clinical patient scheduling. There were no clear differences in image quality between the two different MR systems, however this was not systematically studied. In this study we focused on validating the proposed strategy for interleaved SS and SMS MB=2 acquisitions, as these are the minimal acceleration factors required to achieve whole-heart coverage (6-8 2D slices) with the given spatial resolution for each heartbeat. With the high acquisition efficiency of dual-density spiral trajectories, current acquisition protocols result in in-plane acceleration factors of around 10 and 5 at the outer-edge of k-space for SS and SMS acquisitions, respectively. The proposed SS and SMS MB=2 acquisitions can support heart rate up to 108 beats per minute (BPM), and a heart rate above 120 BPM can be supported by reducing the saturation time to 100 ms per slice. SMS MB=3 acquisition can support a heart rate up to 163 BPM. Based on our experience at 1.5 T[11], we hypothesized that OVS would reduce remote aliasing and improve image quality. However, the impact of OVS, was marginal at best at 3T. In this study we utilized a more optimized strategy to automatically select coils with high sensitivity around the heart[31], which reduced the amount of aliasing from remote coils, potentially reducing the gains previously achieved with OVS. Furthermore, the time between saturation and acquisition was shorter for single-shot imaging at 1.5 T which may have resulted in better suppression of the outer-volume signal. Further, although we optimized the OVS module for 3 T, performance may have been degraded by the increase in B_1 and B_0 inhomogeneity between 1.5 T and 3 T. To reduce SAR, we lengthened the BIR-4 pulse in the OVS module to 5 ms but increasing the duration of the BIR-4 pulse results in further degradation of the performance. Another challenge for using OVS at 3 T is that the minimal acquisition time per slice may need to be increased to avoid going over the time-averaged SAR limit when acquiring data with 3 or more saturations.

While data was acquired during breath-holding in this study, we adapted our previously proposed rigid-registration strategy for motion correction[114]. This strategy was incorporated directly into the reconstruction pipelines for SS and SMS reconstruction to correct for the residual motion that can cause blurring for temporally constrained CS reconstruction. To further improve registration given the significant signal intensity variation, we utilized an iterative-PCA based registration technique[115] which improved registration as compared to a pair-wise approach. While this approach corrects for bulk cardiac motion, it does not correct for through-plane motion artifacts. One approach to reducing through-plane motion artifacts is prospective slice tracking[122], which could potentially be utilized to improve motion correction for 2D imaging.

Off-resonance effects due to B_0 inhomogeneity can cause artifacts, particularly at 3 T including blurring and signal-dropout. At 1.5 T, readouts that are less than 8 ms are typically sufficient to avoid signal drop out artifacts for slices that are 8-10 mm thick[8,9]. At 3 T, we have used readouts that are less than 5 ms, and have seen further improvement in off-resonance performance for readouts less than 4 ms[112]. We have previously utilized off-resonance correction based on acquisition of a field map at each heartbeat, however for highly accelerated imaging this represents a significant overhead (2 additional interleaves per slice per heartbeat)[8]. For our whole-heart accelerated acquisition we utilized an auto-focusing B_0 inhomogeneity correction method which does not require acquisition of a B_0 field map, has a low computational cost and reduces blurring particularly during the peak of first pass of the contrast agent in the LV cavity. Some cases still have mild dropout artifacts in the inferolateral wall. These artifacts primarily affect the epicardial aspect of the inferolateral wall and can be differentiated from ischemia which primarily affects the sub-endocardium. We are currently performing a clinical evaluation of these pulse sequences and will be able to determine if they affect diagnostic utility. From our prior 1.5 T clinical study which utilized 6 ms readouts at 1.5 T we did not see a degradation of diagnostic performance in the LCX territory. Dropout artifacts typically result from signal dephasing across the slice dimension, and can be avoided using shorter readouts and thinner slices, by phase-encoding in the through slice direction, or by using 3D acquisitions[123]. However, utilization of thinner slices reduces SNR, and phase-encoding in the slice dimension reduces efficiency.

Given that the SS interleaved sequence without OVS had the highest image quality, this may be the preferred sequence to achieve whole-heart high-resolution perfusion imaging when 6-8 slices are desired, particularly given the reduced SAR as compared to the SS interleaved acquisition with the OVS module. Preliminary clinical experiments using this technique have demonstrated good performance[13].

We also demonstrated that SMS was feasible at an SMS factor of 3 with good image quality. With MB=3, 6 slices can be acquired at high heart rate with or without OVS without limitations by SAR. Preliminary experiments suggest that imaging at MB=3 is feasible using this strategy. The SMS MB=3 w/o OVS shows higher image quality score than SMS MB=2, which may result from the more incoherent aliasing due to the different SMS phase modulation pattern. Further improvements in the SMS reconstruction algorithm, including further optimization of the strategy for leakage-blocking kernals[107,108,124] could potentially further improve image quality.

This study also has several limitations. While in volunteer studies we could obtain resting perfusion imaging using two different techniques, for studies performed as part of clinical routine, only a single resting perfusion study could be performed. The SS and SMS techniques could not be performed in a paired manner in the clinical subjects as only a single resting perfusion study could be performed. This may add variability when comparing the different techniques utilized in this study. The experiments in this study were performed during resting perfusion, and stress perfusion was not conducted. To address the clinical value of high-resolution perfusion imaging, further qualitative and quantitative evaluations of the performance of the proposed techniques with stress imaging in patients with suspected CAD will be necessary. We have recently demonstrated initial clinical evaluations of the proposed technique for SS acquisitions[12]. While the current spiral acquisition strategy and reconstruction pipeline demonstrate good image quality, further optimization of the trajectory and reconstruction techniques could potentially further improve image quality. Other OVS techniques which do not utilize a BIR-4 may achieve adequate OVS performance without SAR limitations.

3.5 Conclusion

We demonstrated the successful application of high-resolution (1.25×1.25 mm^2) spiral perfusion imaging with whole-heart coverage at 3 T for both SS and SMS acquisitions with and without OVS in a clinical setting. The increased transmural resolution may improve assessment of myocardial perfusion gradients, and the whole-heart coverage may improve quantification of ischemic burden. Further validation will be required in patients undergoing stress CMR to assess the clinical value of high-resolution perfusion imaging.

Chapter 4: DEep learning-based rapid Spiral Image Reconstruction (DESIRE) for High-resolution Spiral Perfusion Imaging

4.1 Introduction

For first-pass perfusion imaging, a contrast agent is injected, and images are acquired over the subsequent 40-60 heart beats. As images are acquired in each heartbeat at stress during the first pass of the contrast agent, the data for each frame must be collected in less than 500-600 ms requiring highly efficient data acquisition strategies. However, this typically requires undersampling in the k-space domain which can result in undesirable aliasing artifacts in the image domain.

Recently, we have developed a rapid interleaved single-slice (SS) spiral perfusion pulse sequence and a corresponding motion-compensated L1-SPIRiT image reconstruction technique[8,33,125]. We have also developed spiral simultaneous multi-slice (SMS) techniques including motion-compensated SMS-L1-SPIRiT reconstruction and SMS-Slice-L1-SPIRiT reconstruction which includes in-plane and through-plane kernels that can further reduce the through-plane aliasing artifacts[9,33,107,126]. However, these advanced image reconstruction techniques rely on iterative algorithms such as non-linear conjugate gradient to recover the images which is time-consuming. As such, these reconstructions are typically performed off-line and do not provide rapid feedback to CMR technicians and physicians. Moreover, the need for parameter tuning for the compressed sensing (CS)-based image reconstruction algorithm can be problematic.

Thus, a faster image reconstruction technique, instead of an iterative non-Cartesian image reconstruction, is essential to facilitate clinical translation. Using deep convolutional neural networks (CNN) for CMR image reconstruction not only boosts reconstruction speed and simplifies parameter tuning, but also maintains high image quality. Recent advances in CMR image reconstruction using CNN[51–64] have been proposed, but most of the works were based on Cartesian imaging. Fan et al[51] and Hauptmann et al[52] demonstrated dynamic radial CMR image reconstruction using 3D U-Net[127,128]based networks. However, the application of deep learning reconstruction for CMR spiral imaging and SMS imaging have been limited. Some image reconstruction

techniques with Cartesian sampling utilized data fidelity updates[54,55,58,129]. However, explicitly enforcing data fidelity is time-consuming and memory-consuming for non-Cartesian imaging, especially for dynamic imaging such as myocardial perfusion imaging.

In this work, we sought to develop a DEep learning-based rapid Spiral Image REconstruction technique (DESIRE) for high-resolution spiral first-pass myocardial perfusion imaging for both SS and SMS MB=2 acquisitions with whole-heart coverage. The highly accelerated spiral perfusion imaging has an in-plane acceleration factor of 10 and 5 for SS and SMS MB=2 acquisitions, respectively. Utilizing the proposed 3D U-Net based denoising architecture, following pre-processing steps of coil selection, motion correction, and NUFFT, the image reconstruction time could be shortened from ~30 minutes per dynamic series to under 3 minutes with a network inference time of ~100 ms while still maintaining high image quality as compared with a current state-of-the-art CS algorithm, making online reconstruction feasible.

4.2 Methods

4.2.1 Pulse Sequences and Data Acquisition

To evaluate the DESIRE technique, first-pass perfusion imaging was performed using both SS and SMS acquisitions. For both SS and SMS MB=2 acquisitions, a variable-density spiral trajectory with Fermi transition was adopted, leading to an in-plane acceleration factor of around 10 and 5 for SS and SMS, respectively. Pulse sequence parameters were from our previously proposed high-resolution spiral perfusion studies at 3 T[33,112,125,126]: FOV=340 mm, TR=8 ms, TE=1 ms, in-plane resolution=1.25×1.25 mm^2, slice thickness=10 mm, flip angles were 26° and 18° for SS and SMS, respectively. Each spiral-out interleave had a readout time of 4 ms, and the number of interleaves were 4 and 8 for SS and SMS acquisitions, respectively. Both SS and SMS had similar signal-to-noise ratio (SNR) and temporal sampling footprint for each slice. Spiral interleaves were uniformly distributed in each heart-beat and were rotated by the golden angle (137°) between heart beats, to achieve temporal incoherence and also to achieve a similar sampling strategy for both SMS MB=2 acquisitions with Hadamard phase cycling of the interleaves in each heart-beat[9,72] and the interleaved SS acquisitions.

A non-selective saturation with an optimized hard-pulse train[113] for T_1-weighted preparation and a spectrally selective adiabatic inversion recovery pulse (SPAIR) for fat suppression were utilized.

Resting perfusion images from 29 healthy volunteers and 5 clinical patients undergoing clinically ordered CMR studies with gadolinium (Gd)-based contrast agents (Gadoteric acid - Gadoterate meglumine; Dotarem Guerbet or Clariscan GE Healthcare) were included. Written informed consent was obtained from all subjects using protocols approved by the University of Virginia Health Sciences Research Institutional Review Board. Imaging was performed on 3 T MRI scanners (MAGNETOM Prisma/Skyra; Siemens Healthineers, Erlangen, Germany). Spiral perfusion imaging was performed using 0.075 mmol/kg of contrast agent injected intravenously at a rate of 4 mL/s followed by 25 mL of saline flush at a rate of 4 mL/s. Subjects were asked to hold their breath as long as possible followed by shallow breathing during the acquisition of perfusion images over 50 to 60 heartbeats. 6-8 slices were acquired for each subject up to the SAR limitation and subject's heart size. 6 out of 29 healthy subjects underwent spiral perfusion imaging during two separate gadolinium injections separated by a 20-minute washout period and the other 23 subjects underwent 1 spiral perfusion scan. Overall, the studies in volunteers and patients resulted in 30 SS and 10 SMS MB=2 perfusion datasets for analysis.

4.2.2 Motion-compensated (SMS-Slice-)L1-SPIRiT Reconstruction Technique

The proposed DESIRE technique aims to achieve similar image reconstruction quality as the iterative L1-SPIRiT based reconstruction technique for high-resolution spiral perfusion imaging. The previously proposed motion-compensated L1-SPIRiT reconstruction results served as the reference images for training of the image reconstruction networks.

The interleaved SS and SMS images can be reconstructed using a motion-compensated technique: (SMS-Slice-) L1-SPIRiT[8,107,126] where the through-plane operator was incorporated in the proposed SMS-Slice-L1-SPRIiT reconstruction for spiral perfusion imaging to reduce the slice leakage and improve the reconstruction performance, which can be expressed as follows:

$$\underset{x}{argmin}||\Phi RF_u x - y||_2^2 + \lambda_1||(G_{SPIRiT} - I)x||_2^2 + \lambda_2||\Psi x||_1 + \lambda_3||(G_{TP} - I)x||_2^2 \qquad \textbf{[4-1]}$$

where x are motion-corrected multi-channel dynamic perfusion images to be reconstructed for each slice, y is the acquired spiral SS or SMS data that might contain motion, F_u is an inverse Fourier gridding operator (NUFFT) that transforms from Cartesian image space to spiral k-space[48], R is the motion-correction operator mapping the motion-corrected perfusion image series to the motion-corrupted image series[130], G_{SPIRiT} is an image-space SPIRiT operator for each slice[45], G_{TP} is an image-space through-plane (TP) operator which is calibrated by enforcing consistency on the desired slice and blocking the signal from the interfering slices to reduce slice leakage artifacts[33,131,132], Ψ is the finite time difference transform that operates on each individual coil separately enforcing sparsity in the temporal domain of perfusion image series, I is the identity matrix, λ_1, λ_2 and λ_3 are parameters that balance the data acquisition consistency with SPIRiT calibration consistency, temporal sparsity and slice consistency, and Φ is the SMS Hadamard phase modulation operator[72] that depends on the number of interleaves and the desired SMS factor. For SS acquisition the same equation can be utilized by setting Φ to I and setting $\lambda_3 = 0$, which results in the SS L1-SPIRiT reconstruction. $\lambda_1 = 1$ and $\lambda_2 = 0.4M_0$ where M_0 was the maximal magnitude value of the NUFFT images were chosen for SS reconstructions as in our SMS-Slice-L1-SPIRiT manuscript.[33] Similarly, for SMS reconstructions, $\lambda_1 = 1$, $\lambda_2 = 0.5M_0$, and $\lambda_3 = 1$ were selected as in our prior publication[33]. These parameters were selected based on the results of a retrospective experiment that balanced image quality and temporal fidelity as first described by Feng et al[116]. The same regularization parameters were used for all reconstructions.

The motion correction operator R was 2D in-plane rigid motion correction as described by Zhou et al[130]. To achieve good motion correction in the setting of the dynamic signal intensity variation in perfusion image series, images were registered to synthetic images derived by performing temporal principal component analysis so that images could be rigidly registered to a target frame that has consistent signal intensities[33].

Prior to image reconstruction, coil selection is performed to retain coils with low artifact power and high SNR in the region around the heart as described by Zhou et al[31]. This CS-based motion-compensated image reconstruction problem is solved using a nonlinear iterative conjugate gradient descent algorithm[117] with 80 iterations to achieve high image quality. This iterative reconstruction process takes ~30 minutes per dynamic

perfusion image series from a single slice location. The (SMS-Slice-)L1-SPIRiT image reconstruction and processing with GPU-accelerated NUFFT[133] was conducted in MATLAB (The MathWorks, Natick, MA).

4.2.3 Proposed DESIRE Reconstruction Technique

We sought to comprehensively evaluate the reconstruction performance by evaluating four different factors: (1) the choice of magnitude-valued and complex-valued data types, (2) the difference of complex-valued and real-valued convolutions, (3) the influence of network structures including depth and the number of kernels at the initial layer for 3D networks and (4) the comparison between the (2D+t) and the 3D convolutional unit. The number of trainable parameters for each network are listed in Table 4-1.

Network Structure		No. of Trainable Parameters
Complex-valued Convolution	3D, D2K16	609282
	3D, D3K16	2510594
	3D, D2K32	2434050
	3D, D3K32	10037762
Non-complex-valued Convolution	3D, D2K16 (Magnitude Data)	304641
	(2D+t), D2K16	305164
	3D, D2K16 (Baseline)	305090
	3D, D3K16	1255746
	3D, D2K32	1217922
	3D, D3K32	5019778

Table 4-1. The number of trainable parameters for each network.

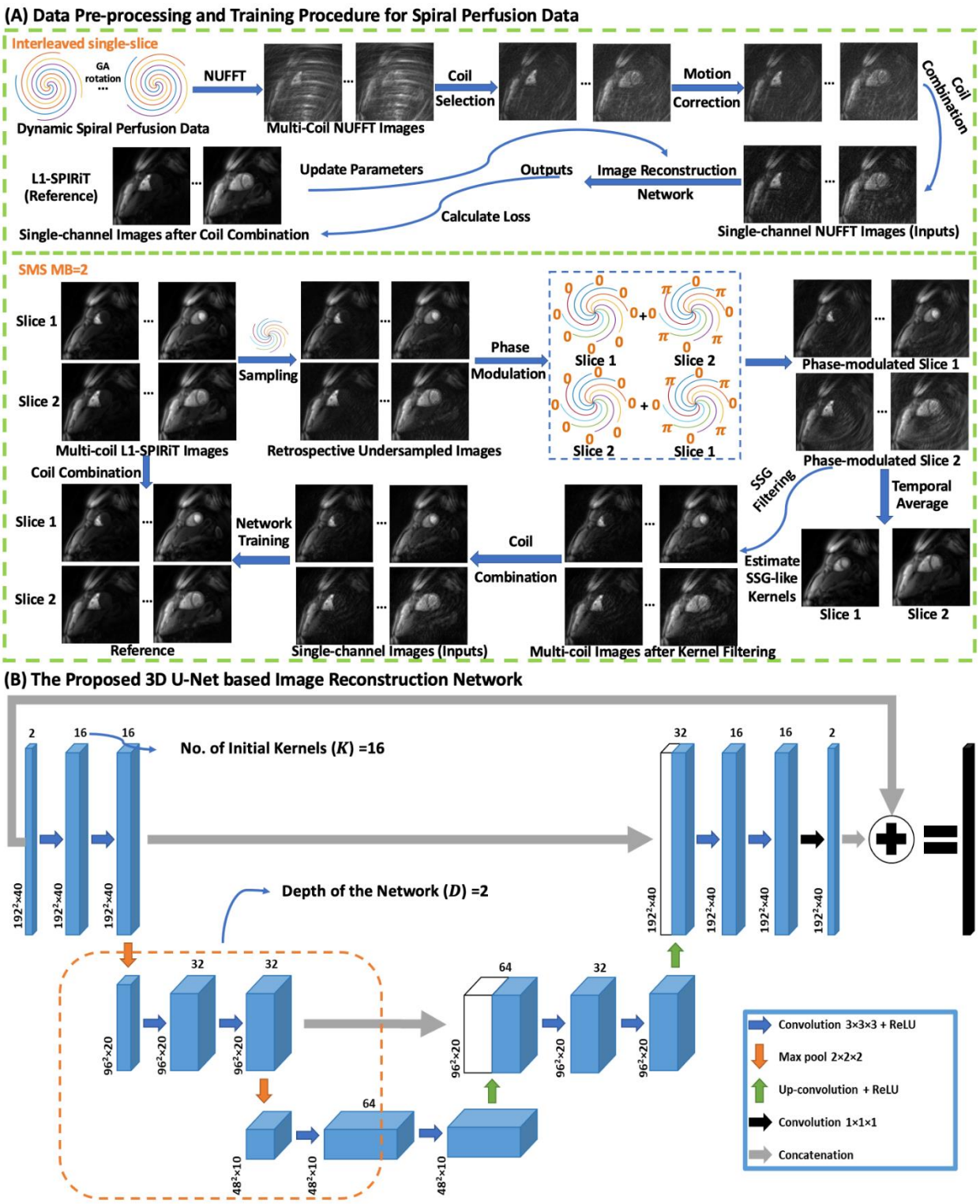

Figure 4-1. The proposed deep learning-based image reconstruction workflow and the proposed 3D U-Net based image reconstruction network for spiral first-pass perfusion imaging. (A) shows the pre-processing steps for both interleaved SS and SMS MB=2 acquisitions. The baseline network is shown in (B), which has several initial kernels of 16

and a depth of 2. The numbers above each layer denote the number of kernels at each layer, and the corresponding image shape at each layer is also labelled.

All the following comparisons were conducted with respect to the baseline model as shown in Figure 4-1-B. This baseline model is a 3D U-Net image reconstruction network taking the complex-valued data as inputs where real and imaginary parts are concatenated along the channel dimension[134]. The outputs are the concatenated real and imaginary perfusion image series. As illustrated in Figure 4-1-B, the baseline network has a depth of 2 (D=2), 16 initial kernels (K=16), 3×3×3 convolution kernel and 2×2×2 pooling size. We chose to use a kernel size of 3 based on preliminary experiments which demonstrated that kernel sizes of 5 and 7 did not improve reconstruction performance. The non-linear ReLU activations are conducted after each convolutional layer on each channel. Batch normalization operations are omitted from the network to reduce the GPU memory costs. A residual connection is conducted by summing the inputs and the model outputs[51,52].

Data Pre-Processing

Prior to inputting the data into the image reconstruction network, the pre-processing steps for data preparation were conducted as illustrated in Figure 4-1-A. For 3D networks, the inputs to the network were undersampled 3D perfusion image series (2D spatial + time) from a single slice location following coil-selection[31], rigid motion-correction[130], and adaptive phase combination as described by Walsh et al[135]. To save the GPU memory cost, each dynamic perfusion image series was cropped into a 192×192 matrix with 40 temporal frames, where temporal frames 1 to 40 were cropped out of temporal frames 1 to 50 or 60 to reconstruct images during the first pass of the contrast agent. For each 3D input (2D spatial + time), the image intensities were normalized by its maximum absolute value.

Specifically, for SMS MB=2, to prevent slice-leakage artifact from being learned by the SMS network, the reference image data were SS L1-SPIRiT images at each slice locations, and the input images were the retrospective data from the two separate slice images with Hadamard SMS MB=2 phase modulation[72]. Similar to the SMS-Slice-L1-SPIRiT method[33], an through-plane kernel was applied on the initial images to further reduce the interfering artifact from the other slice prior to inputting the data into the network.

Evaluation 1: Magnitude-valued vs. Complex-valued Data Input Types

We evaluated the reconstruction performance between using magnitude-valued or complex-valued data inputs and outputs. The magnitude-valued data for both inputs and outputs were generated by using the absolute values of the complex-valued data following optimal coil combination. Magnitude images do not take the complex-nature of the input data into account, whereas utilizing complex-valued data takes the phase of the MR images into consideration. A magnitude image-based 3D network was utilized where only a single input and output channel was used. The number of initial kernels and depth were the same as the baseline network shown in Figure 4-1-B. The magnitude-valued data were fed into the 3D model to compare the performance with respect to the baseline model taking the complex-valued data as inputs.

Evaluation 2: Complex-valued vs. Real-valued Convolutions

Unlike the baseline model taking the real and imaginary parts of data into two separate channels and performing real-valued convolutions at each layer, the complex-valued convolutions explored the inherent relationship between complex numbers, and it might improve the image reconstruction performance[136,137].

Assume a complex image data is represented as $I = a + ib$, where a is the real part and b is the imaginary part. The convolution of I with a complex filter $F = x + iy$ can be formulated as:

$$C = I * F = (a + ib) * (x + iy) = (a * x - b * y) + i(a * y + b * x) \quad \textbf{[4-2]}$$

which can be formulated as the following matrix form:

$$C = \begin{bmatrix} Re(I * F) \\ Im(I * F) \end{bmatrix} = \begin{bmatrix} x & -y \\ y & x \end{bmatrix} \begin{bmatrix} a \\ b \end{bmatrix} \quad \textbf{[4-3]}$$

where $Re(I * F)$ is the real component of C and $Im(I * F)$ is the imaginary component of C.

The network that performed the complex-valued convolution had the same structure as the baseline network (Figure 4-1-B). Due to GPU memory limitation, the complex-valued convolution could only be used with a depth of 2 and 16 initial kernels (D2K16). The complex-valued convolution as shown above was enforced at each layer for the real and imaginary channels. The complex-valued image reconstruction network utilized

ℂReLU where real and imaginary parts underwent standard ReLU operations separately, which has been demonstrated to result in the superior performance in the U-Net based image reconstruction network previously[137].

Evaluation 3: Different 3D Network Structures

The baseline network as shown in Figure 4-1-B has a depth of 2 (D=2) and 16 kernels in the initial layer (K=16). The U-Net based network has a structure where the number of kernels at each layer doubles as the network goes to each deeper layer. Compared with the baseline network, we aimed to evaluate the reconstruction performance as a function of the depth of the network (D) and the number of kernels at initial layer (K). Increasing the number of kernels at initial layer give the network more capacity to learn the mapping function from the undersampled images to the ground truth. With pooling operations, the height and width of the image gradually reduces as the number of layers increases, which helps the kernels in the deeper layers to focus on a larger receptive field to better understand the features presented in the image. Given the limitation of GPU memory, we explored 3D networks with real-valued convolutions that had a depth of 2 or 3 (D=2 or 3) and 16 or 32 kernels at the initial layer (K=16 or 32), which resulted in four network structures: D2K16, D2K32, D3K16 and D3K32. Additionally, analysis was conducted for the complex-valued convolutional network structures with more layers and initial kernels: D2K16, D2K32, D3K16 and D3K32.

Evaluation 4: Comparison of (2D+t) and 3D Convolutional Networks

For the 3D input data, either joint 3D convolutions or the separable 3D convolutions[55,58,138] (i.e. the 3D convolution is decomposed into simpler 2D spatial and 1D temporal convolutions, referred as 2D+t convolutions) can be conducted. The performance of (2D+t) and 3D convolutions were compared for the baseline network (D2K16). For (2D+t) convolutional networks, an additional ReLU activation is added in between spatial and temporal convolutions to enhance the representational power. To make a fairer comparison, the number of trainable parameters between (2D+t) and 3D networks is matched by setting the number of 2D spatial filters as:

$$N = \frac{t d_x d_y N_{in} N_{out}}{d_x d_y N_{in} + t N_{out}} \quad \textbf{[4-4]}$$

where the spatial kernel size is $d_x \times d_y \times 1$ and the temporal kernel size is $1 \times 1 \times t$, N_{in} is the number of input kernels at each layer, N_{out} is the number of kernels after the temporal convolution at each layer, and N is the number of kernels after the intermediate spatial convolution. d_x, d_y and t were set as 3 to match the kernel size of 3D convolutions. This leads to the number of trainable parameters of 305164 and 305090 for (2D+t) and 3D convolutional networks, respectively.

Training Procedures

The deep learning model was implemented in PyTorch and all of the training procedures were conducted on a GPU server equipped with Python (version 3.6, Python Software Foundation). The training of the 3D baseline networks was conducted using PyTorch.

Each network was trained with a batch size of 4 using the standard ADAM optimizer with hyperparameters β_1=0.9, β_2=0.999, ϵ=10^{-8} and a learning rate of 0.0001. All of the trainings were conducted for 150 epochs by minimizing an $\ell 1$ loss: mean absolute error (MAE) of the reconstructed images to the ground-truth L1-SPIRiT images. MAE was calculated using the magnitude images of the final reconstructions. The choice of this $\ell 1$ loss function was based on our initial experiments that demonstrated improved SSIM for $\ell 1$ loss as compared to $\ell 2$ loss, which was consistent with other studies comparing loss functions for image reconstruction and restoration[61,139].

SS and SMS networks were trained separately. In the training procedure for both SS and SMS MB=2 networks, 156 slices from 20 perfusion data were used for training, and another 14 slices from 2 perfusion data sets were used for validation.

4.2.4 Experimental Hardware

The training of networks (D2K16) was conducted on a single GPU (Tesla P100, 12GB memory, NVIDIA, Santa Clara, CA, USA). The training of the 3D networks with more layers or initial kernels and complex-valued convolutions were conducted on four P100 GPUs due to the memory limitation of a single GPU.

The reconstruction time of the proposed DESIRE with different network structures and operations was evaluated on the single aforementioned P100 GPU, and the CS-based SMS-Slice-L1-SPIRiT reconstruction with GPU-NUFFT[133] as GPU acceleration was conducted on a server equipped with an Intel i7-7700K CPU (4.20 GHz) with 32 GB memory. CS-based reconstruction also used P100 GPUs.

4.2.5 Image Analysis

For SS networks, the performance of the proposed technique was evaluated on a separate 56 slices from 8 subjects that were prospectively acquired using the SS pulse sequence. These SS data were also retrospectively processed to validate the training performance of SMS networks.

For SMS MB=2 networks, in addition to the retrospective data from SS acquisitions, another 76 slices from 10 subjects with prospective SMS MB=2 acquisitions were used for testing.

Structural similarity index (SSIM), peak signal-to-noise ratio (PSNR) and normalized root mean square error (NRMSE) were assessed for prospective SS data and retrospective SMS MB=2 data.

For both prospectively acquired SS and SMS MB=2 data, two experienced cardiologists blindly graded images reconstructed using the proposed DESIRE networks that had the best performance and the CS-based (SMS-Slice-)L1-SPIRiT (5, excellent; 1, poor). Example images from this scoring system are presented in the appendix of the work by Wang et al[33]. The reconstruction time per slice (40 dynamic frames) was also evaluated.

4.2.6 Statistical Analysis

The normality of the SSIM, PSNR and NRMSE values were assessed using the Shapiro-Wilk test. Normally distributed parameters are described by their mean and standard deviation, while non-normally distributed parameters are described using the median and interquartile range (IQR). A non-parametric Kruskal-

Wallis test with Tukey correction was used to test for differences between the techniques. Comparisons between individual performances were conducted using a Wilcoxon signed-rank test with Bonferroni correction. For all statistical comparisons a p-value of <0.05 were considered statistically significant. Statistical analysis was performed using SAS (version 9.4; SAS Institute Inc., Cary, NC).

4.2.7 Validation on High-resolution Spiral Perfusion Imaging at 1.5 T

1.5 T has been the dominant field strength for cardiac MR imaging as it has better B_0 and B_1 homogeneity than at 3 T. Here, we aim to develop high-resolution spiral perfusion imaging at 1.5 T for both SS and SMS imaging with high SMS acceleration factors (MB=3 and MB=4), to provide fast and high-quality image reconstruction.

SS (N=5), SMS MB=3 (N=9), and MB=4 (N=3) golden-angle spiral perfusion data sets with 1.5×1.5 mm^2 in-plane spatial resolution and whole-heart coverage (6-9 slices) were acquired from 17 patients undergoing clinical studies on a 1.5 T SIEMENS Aera scanner[125,126]. Detailed pulse sequence parameters are listed in Table 4-2.

	single-slice	simultaneous multi-slice
FOV (mm^2)	340×340	
Spiral Interleaves	5	8
Spiral Readout Duration (ms)	5	6
Spiral Shape	Fermi Dual Density	Linear Variable Density
Spiral Starting Density	1x (Nyquist)	0.75x (Nyquist)
Spiral Ending Density	0.15x (Nyquist)	0.2x (Nyquist)
TR (ms)	8	
TE (ms)	1	
Flip Angle (°)	26	18
Slice Thickness (mm)	8	
Spatial Resolution (mm^2)	1.5×1.5	
Temporal Resolution (ms)	~60	

Table 4-2. Detailed acquisition parameters for spiral perfusion imaging at 1.5 T.

Before inputting the data into the network, coil-selection[31], motion-correction[114], and adaptive phase combination[120] were performed on the NUFFT-gridded[48] multi-coil image series at each slice location.

Specifically, for SMS data, perfusion image series that were input to the network were filtered by the through-plane kernels[33,107] at each slice location to reduce the slice leakage.

The training data were SS golden-angle spiral perfusion data sets with whole-heart coverage acquired from 18 healthy volunteers and 4 patients undergoing our prior clinical studies on 3 T SIEMENS Skyra/Prisma scanners[33]. As described previously, the network adopted was the D3K32 with complex-valued convolutions enforced. The reference images were L1-SPIRiT reconstructions. 156 slices from 20 subjects were used for training. The training was conducted using PyTorch on four NVIDIA Tesla P100 GPUs with 150 epochs using an L1 loss. To test the performance of the proposed technique, prospective SS and SMS images were also reconstructed using the GPU-accelerated (SMS-Slice-)L1-SPIRiT where the through-plane kernel was utilized for SMS imaging to reduce the slice leakage.

Prospective SS and SMS images reconstructed by both (SMS-Slice-)L1-SPIRiT and the proposed DESIRE technique were blindly graded by an experienced cardiologist (5, excellent; 1, poor).

4.3 Results

High image quality was achieved using the proposed DESIRE image reconstruction technique for both SS and SMS MB=2 acquisitions. The Shapiro-Wilk test showed that the SSIM, PSNR and NRMSE for each network structure were non-parametric, therefore the median and IQR values were used to represent the data and Kruskal-Wallis test was conducted separately within the group of SS and SMS MB=2. Table 4-3-A and Table 4-3-B showed the image quality assessment with respect to SSIM, PSNR and NRMSE for both prospective SS and retrospective SMS MB=2 data.

A. Image Quality Assessment for Single-Slice Acquisition

Network Structure		SSIM	PSNR (dB)	NRMSE
Complex-valued Convolution	3D, D2K16	0.970 [0.962, 0.976][a]	41.054 [38.717, 43.101][b]	0.113 [0.087, 0.148][d]
	3D, D3K16	0.967 [0.958, 0.973]	41.145 [39.115, 42.712][b]	0.112 [0.090, 0.146][d]
	3D, D2K32	0.971 [0.963, 0.975][a]	40.857 [38.236, 43.127][b]	0.118 [0.094, 0.149][e]
	3D, D3K32	**0.977 [9.972, 0.982]**	**42.113 [40.174, 43.493][g]**	**0.102 [0.080, 0.125][f]**
Non-complex-valued Convolution	3D, D2K16 (Magnitude Data)	0.898 [0.881, 0.915]	36.893 [35.307, 38.098]	0.182 [0.145, 0.228]
	(2D+t), D2K16	0.957 [0.948, 0.965]	40.133 [37.981, 41.886]	0.130 [0.103, 0.165]
	3D, D2K16 (Baseline)	0.959 [0.950, 0.968]	40.658 [38.568, 42.238][c]	0.122 [0.097, 0.158][g]
	3D, D3K16	0.964 [0.954, 0.972]	40.617 [38.332, 42.557][c]	0.120 [0.095, 0.153][e, g]
	3D, D2K32	0.971 [0.963, 0.977][a]	41.971 [39.699, 43.524][g]	0.099 [0.081, 0.130][f]
	3D, D3K32	0.971 [0.964, 0.977][a]	41.571 [38.856, 43.668][b]	0.110 [0.089, 0.142][d]

B. Image Quality Assessment for SMS MB=2 Retrospective Data

Network Structure		SSIM	PSNR (dB)	NRMSE
Complex-valued Convolution	3D, D2K16	0.958 [0.949, 0.965][a]	39.603 [38.209, 40.792][c]	0.115 [0.095, 0.146][f]
	3D, D3K16	0.951 [0.939, 0.960][b]	39.696 [38.464, 40.801][c]	0.124 [0.010, 0.151]
	3D, D2K32	0.958 [0.949, 0.965][a]	40.394 [39.147, 41.508][d]	0.110 [0.090, 0.136][i]
	3D, D3K32	0.957 [0.946, 0.966][a]	40.400 [39.138, 41.512][d]	0.109 [0.088, 0.133][i]
Non-complex-valued Convolution	3D, D2K16 (Magnitude Data)	0.934 [0.922, 0.945]	39.083 [38.038, 40.322]	0.128 [0.105, 0.158]
	(2D+t), D2K16	0.953 [0.942, 0.962][b]	40.015 [38.788, 41.146][e]	0.120 [0.095, 0.146][f, g, h]
	3D, D2K16 (Baseline)	0.952 [0.941, 0.961][b]	39.861 [38.582, 40.948][c, e]	0.121 [0.096, 0.149][f, g]
	3D, D3K16	0.954 [0.943, 0.963][b]	40.237 [39.095, 41.413][d]	0.116 [0.093, 0.143] [h]
	3D, D2K32	0.957 [0.947, 0.965][a]	40.398 [39.162, 41.459][d]	0.113 [0.091, 0.140][f]
	3D, D3K32	**0.961 [0.950, 0.969]**	**40.834 [39.619, 42.004]**	**0.107 [0.086, 0.133][i]**

Table 4-3. Summary of the image quality assessment for different network structures. Different letters indicate groups there are no significant difference (p>0.05) and networks with the best performance are labelled as bold.

For evaluation 1, utilizing the complex-valued data showed better performance compared with using the magnitude-valued data in terms of SSIM, PSNR and NRMSE for both SS and SMS MB=2 ($p=1.27\times10^{-7}$). A model taking the magnitude-valued data might fail to explore the phase information.

Figure 4-2 shows comparison between magnitude-valued and complex-valued data types for 3D U-Net image reconstruction networks (D2K16) from a healthy volunteer undergoing SS acquisition. There is noticeable residual artifact along the chest wall with the magnitude-valued data.

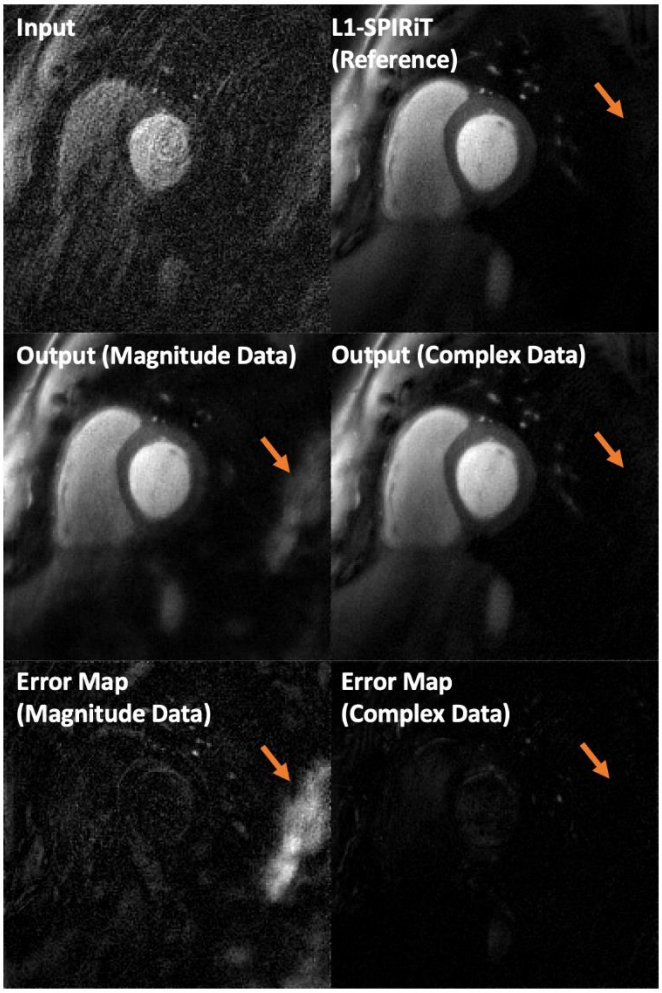

Figure 4-2. Evaluation of the image reconstruction results using magnitude data. Images were acquired from a healthy volunteer undergoing SS acquisition and reconstructed using the baseline network (D2K16). As pointed out by the arrows, the noticeable artifact from the chest wall can be visualized in the output of the network using the magnitude-valued data, which might be due to the failure to include the phase information in the data.

For evaluation 2, the utilization of complex-valued convolution was compared to standard real-valued convolutions with respect to SSIM, PSNR and RMSE for SS and SMS MB=2. For SS, the utilization of complex-valued convolution (D2K16) showed no statistically significant difference with non-complex-valued convolution using D2K32 and D3K32 networks in terms of SSIM ($p=0.08$ and $p=0.09$, respectively), and no

statistically significant difference with D3K32 in terms of PSNR (p=0.11) and NRMSE (p=0.06). For SMS MB=2, enforcing complex-valued convolution had no statistically significant difference with D2K32 in terms of SSIM (p=0.10), no statistically significant difference with D2K16 in terms of PSNR (p=0.41), and no statistically significant difference with D2K16 (p=0.30) and D3K16 (p=0.25) in terms of NRMSE. Enforcing the complex-valued convolution exploits the inherent phase information in MR data. The improvement by using complex-valued convolutions showed similar performance as increasing the number of layers and initial kernels for the magnitude convolutions.

Figure 4-3 demonstrates the performance of real-valued and complex-valued convolution operations from a healthy volunteer undergoing SS acquisition. Overall, good image quality was demonstrated by using the 3D U-Net networks. However, the network with complex-valued convolution recovered more details near the right ventricle as pointed out by the arrow. The error map showed that the complex-valued convolution operation had less errors than the regular convolutional network as compared with the ground-truth L1-SPIRiT images.

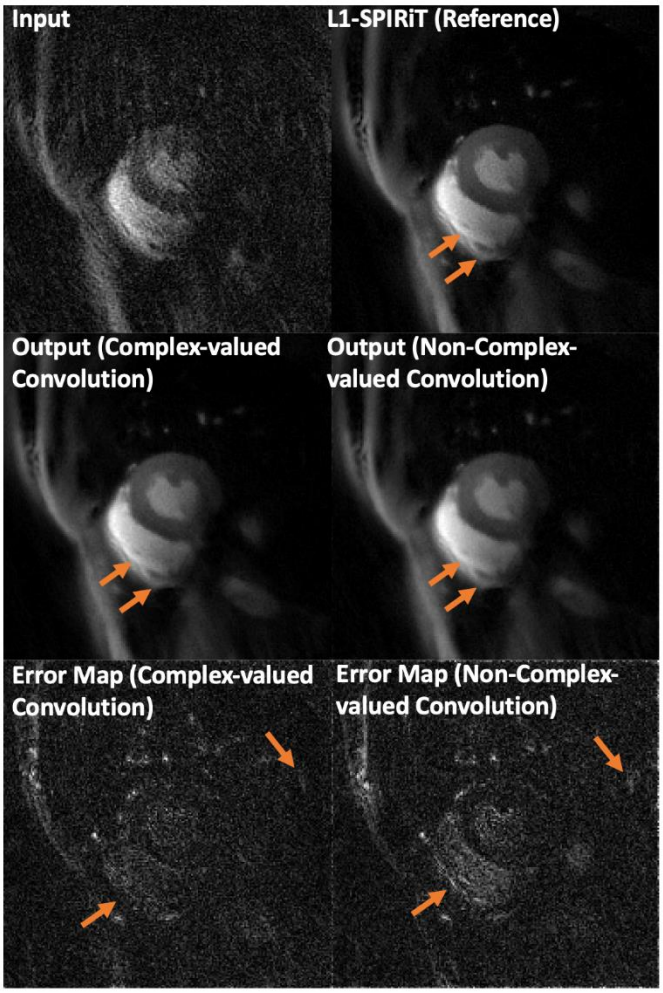

Figure 4-3. Evaluation of the complex-valued convolution. Images were acquired from a healthy volunteer using SS acquisition and reconstructed using the baseline network with and without complex-valued convolution. The network with complex-valued convolution recovered more details near the right ventricle as pointed out by the arrow. The error maps showed that the complex-valued convolution operation had less errors than the regular convolutional network as compared with the L1-SPIRiT images.

For evaluation 3, for real-valued convolutional networks, an improved performance was noticed by increasing the depth of network and the number of kernels at the initial layer. However, the capacity of the network can be achieved: for SS, there was no statistically significant difference between D2K32 and D3K32 in terms of SSIM ($p=0.14$) and no statistically significant difference between D2K16 and D3K16 in terms of PSNR ($p=0.18$) and NRMSE ($p=0.11$); for SMS MB=2, there was no statistically significant difference between D2K16 and D3K16 in terms of SSIM ($p=0.21$) and no statistically significant difference between D2K32 and D3K16 in terms of PSNR ($p=0.25$) and NRMSE ($p=0.27$). For complex-valued convolutional networks, the network

capacity was also achieved: for SS, there was no statistically significant difference between D2K16 and D2K32 in terms of SSIM (p=0.82) and PSNR (p=0.77) and no statistically significant difference between D2K16 and D3K16 in terms of PSNR (p=0.32) and NRMSE (p=0.41); for SMS MB=2, there was also no statistically significant difference between D2K16, D2K32 and D3K32 in terms of SSIM (p=0.48), no statistically significant difference between D2K16 and D3K16 in terms of PSNR (p=0.42), and no statistically significant difference between D2K32 and D3K32 in terms of NRMSE (p=0.38).

Figure 4-4 shows the comparison of different network structures. Increasing the number of kernels at initial layer and increase the depth of the network lead to improved performance. Overall, good image quality was achieved for all 3D network structures. However, as pointed out by arrows and error maps, subtle aliasing artifact could still be visualized for a network with fewer initial kernels and less depth.

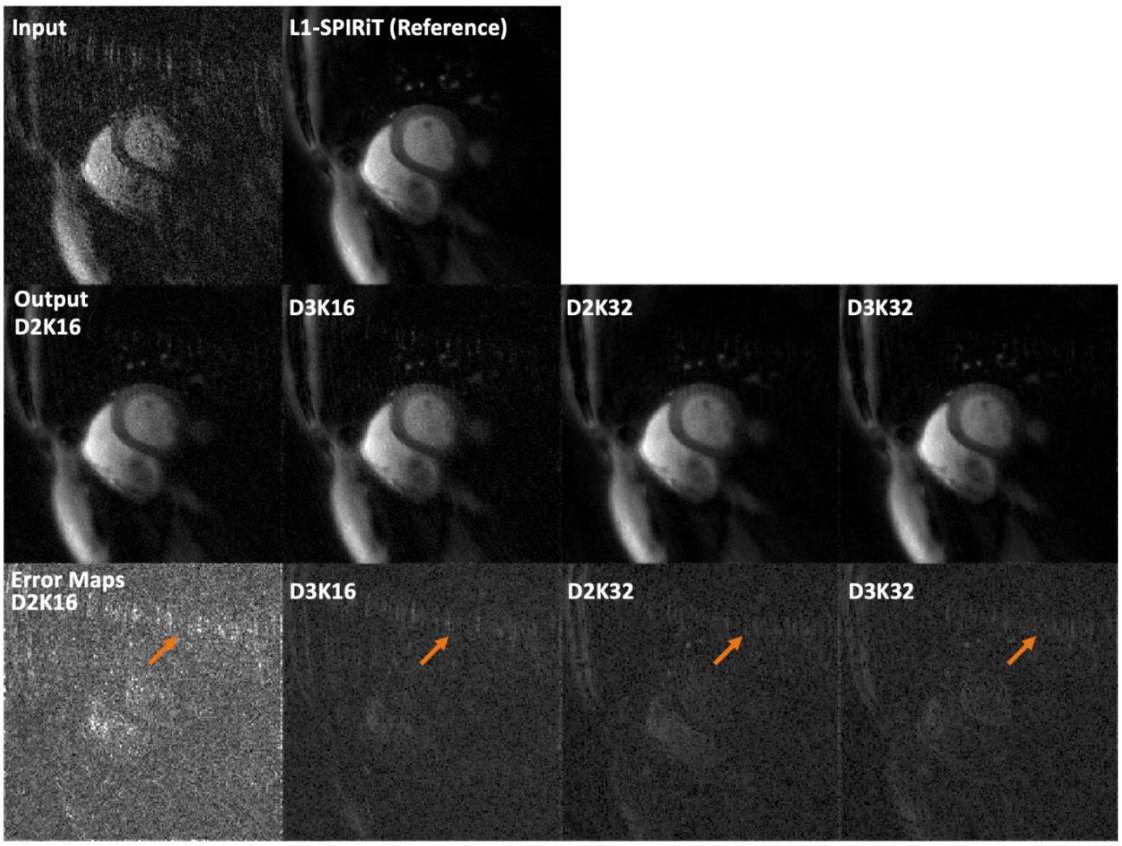

Figure 4-4. Evaluation of various network structures. Images were acquired from a healthy volunteer using SS acquisition and reconstructed using the 3D networks with different network structures. Images reconstructed using networks with more depth and initial kernels present less error as compared to the ground-truth images. Error maps were normalized with respect to the error map of D2K16 (baseline model).

For evaluation 4, the utilization of (2D+t) convolutions did not outperform the 3D convolutions for both SS and SMS MB=2 data. Results from SS data indicate the (2D+t) convolutional network was inferior to the results of 3D convolutional network ($p=6.04\times10^{-4}$) in terms of SSIM, PSNR and NRMSE (Table 4-3). However, for SMS MB=2, statistical analysis indicates the (2D+t) convolutional network had no statistically significant difference to the results of 3D convolutional network ($p=0.90$) in terms of SSIM, PSNR and NRMSE.

Figure 4-5 shows the comparison of using (2D+t) and 3D convolutional networks for case with SS acquisition. Overall, good image quality was achieved for both networks. However, subtle aliasing could still be visualized in the results for (2D+t) network.

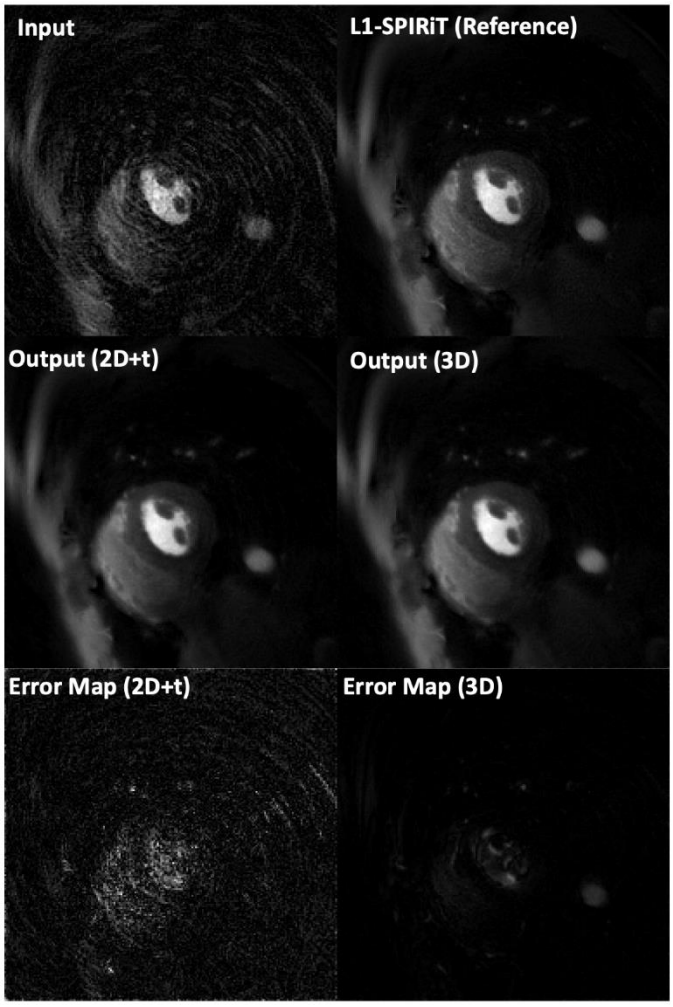

Figure 4-5. Evaluation of the (2D+t) and 3D convolutional networks. Images were acquired from a healthy volunteer with SS acquisition and reconstructed using the baseline network structure with (2D+t) and 3D convolutional

units. The network with 3D convolution recovered more details as pointed out by the arrow. The error maps showed that (2D+t) convolutional network had more errors than the 3D convolutional network as compared with the L1-SPIRiT images.

Figure 4-6 shows resting perfusion images acquire in a healthy volunteer using the SS acquisition. The images were reconstructed using DESIRE network that had the best performance (D3K32 with complex-valued convolution) and L1-SPIRiT separately. The image quality scores for this case were 5 and 4.8 for DESIRE and L1-SPIRiT, respectively. The SSIM, PSNR and NRMSE for these cases were 0.979 [0.972, 0.984], 42.456 [39.670, 43.434] dB and 0.082 [0.068, 0.114], respectively.

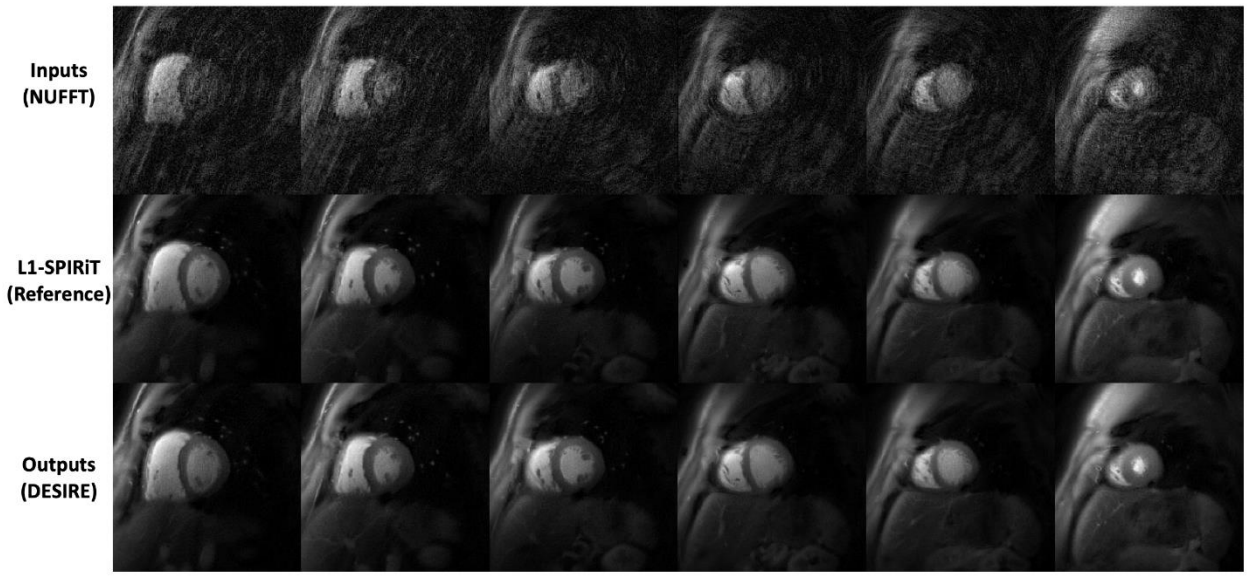

Figure 4-6. Interleaved SS prospective spiral perfusion images from a healthy volunteer with 6 slices reconstructed using L1-SPIRiT and the proposed DESIRE image reconstruction network (D3K32 with complex-valued convolution). Excellent image quality was demonstrated using the proposed image reconstruction network with an SSIM of 0.979 [0.972, 0.984], a PSNR of 42.456 [39.670, 43.434] dB, and a NRMSE of 0.082 [0.068, 0.114]. Image quality scores for the DESIRE and L1-SPIRiT were 5 and 4.8, respectively (5, excellent; 1, poor).

Figure 4-7 presents the performance for retrospective and prospective SMS MB=2 data. The images were reconstructed using DESIRE network that had the best performance (D3K32) and (SMS-Slice)-L1-SPIRiT separately. (A) shows an example case from a healthy volunteer undergoing SS acquisition but with retrospective SMS modulation. Good image quality was demonstrated with an SSIM of 0.964 [0.956, 0.969], a PSNR of 41.516 [40.681, 42.127] dB, and a NRMSE of 0.092 [0.081, 0.106]. (B) shows an example case from a healthy volunteer undergoing SMS MB=2 acquisition with whole-heart coverage. Good image quality was demonstrated with a score of 4.3 for DESIRE and 4.3 for SMS-Slice-L1SPIRiT (5, excellent; 1, poor).

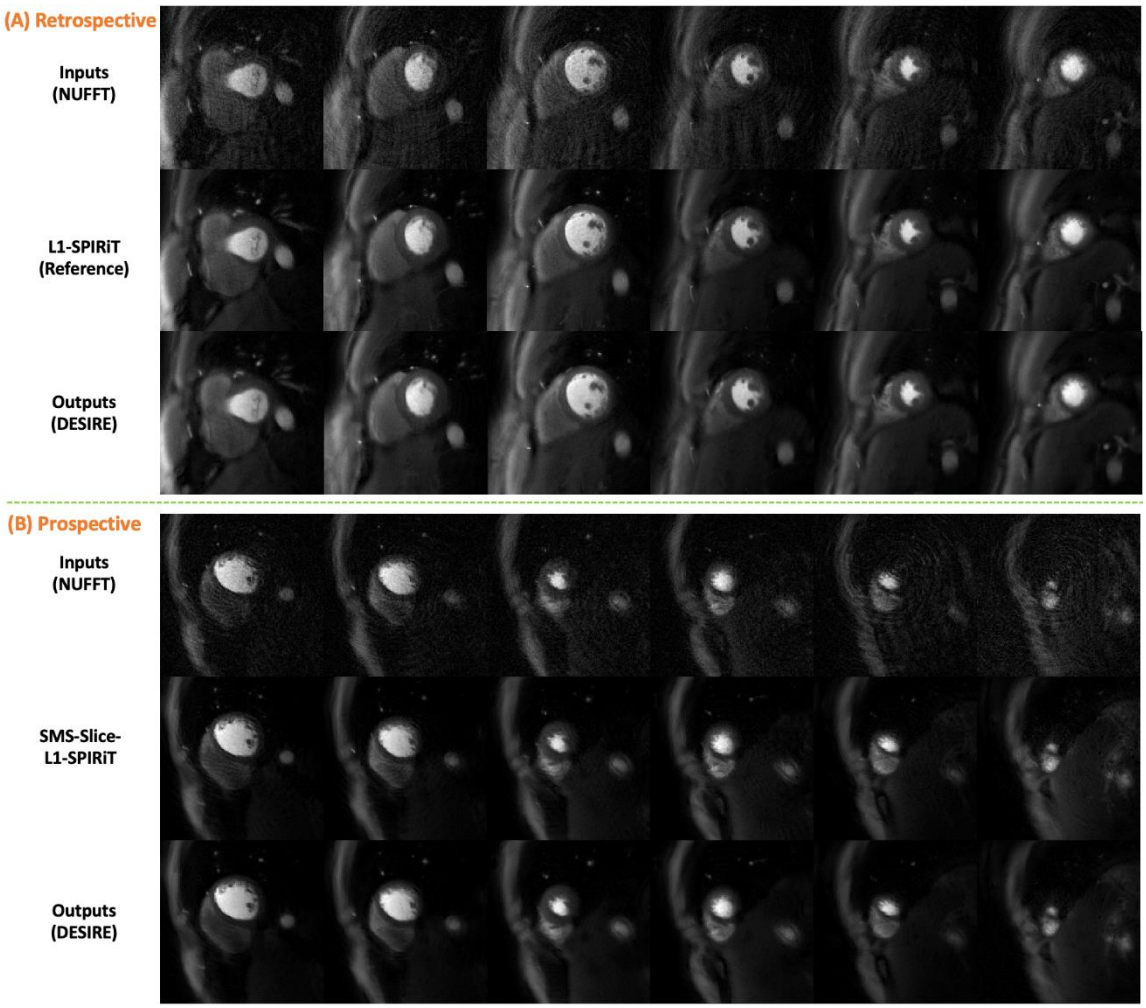

Figure 4-7. Evaluation of the SMS MB=2 acquisitions. (A) shows retrospective SMS MB=2 spiral perfusion images from a healthy volunteer with 6 slices and (B) shows prospective SMS MB=2 spiral perfusion images from a healthy volunteer with 6 slices reconstructed using the proposed DESIRE image reconstruction network (D3K32). Good image quality was demonstrated using the proposed image reconstruction network. The case in (A) has an SSIM of 0.964 [0.956, 0.969], a PSNR of 41.516 [40.681, 42.127] dB, a RMSE of 0.092 [0.081, 0.106]. The case in (B) has an image quality score of 4.3 and 4.3 (5, excellent; 1, poor) for DESIRE and SMS-Slice-L1-SPIRiT, respectively.

Figure 4-8 presents a patient that underwent a research stress spiral perfusion imaging using the SS acquisition. The images were reconstructed using DESIRE (D2K32) and L1-SPIRiT separately. Good image quality was demonstrated with an SSIM of 0.951 [0.943, 0.958], a PSNR of 38.750 [36.439, 40.276] dB and a NRMSE of 0.143 [0.101, 0.173]. The perfusion defect seen in the DESIRE image is in agreement with the L1-SPIRiT reconstruction and corresponds to the high-grade defect seen at cardiac catheterization. The temporal fidelity of the images reconstructed using DESIRE also had good agreement with the ground truth (L1-SPIRiT) and the input data for which each frame is reconstructed separately without any temporal regularization.

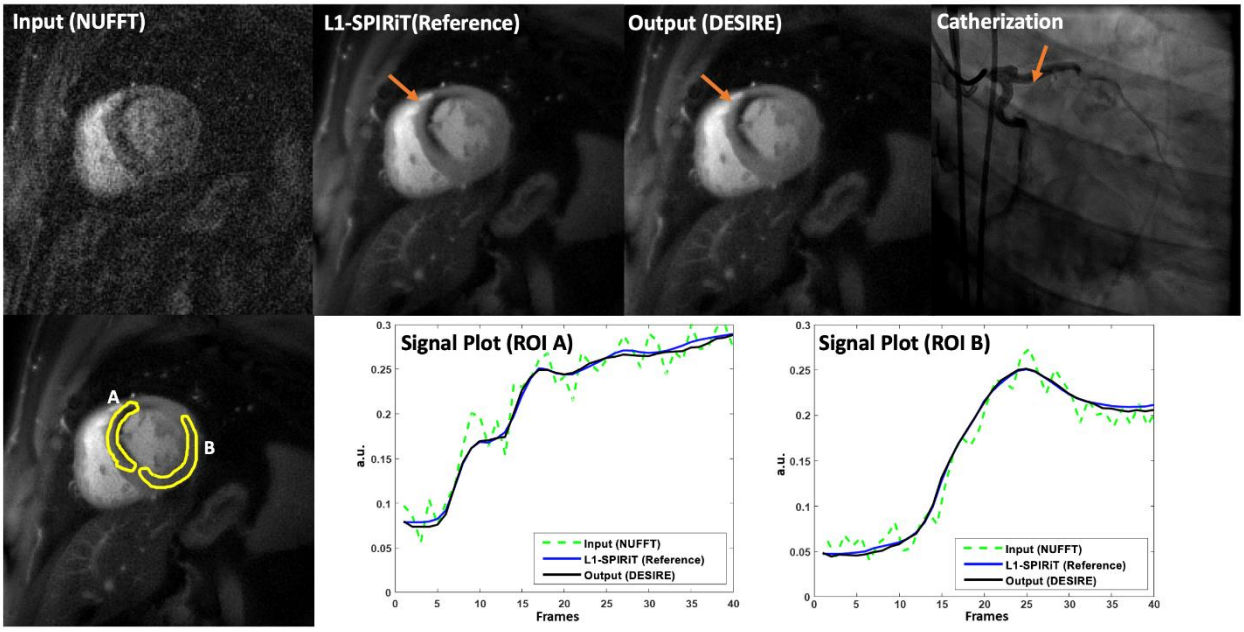

Figure 4-8. A patient underwent clinical stress spiral perfusion imaging using the SS acquisition. Images were reconstructed using the proposed DESIRE technique (D2K32 network) and L1-SPIRiT which served as the ground truth. Good image quality was demonstrated with an SSIM of 0.951 [0.943, 0.958], a PSNR of 38.750 [36.439, 40.276] dB and a NRMSE of 0.143 [0.101, 0.173]. The image quality score for DESIRE and L1-SPIRiT were 5 and 5, respectively. The perfusion defect showed in DESIRE had good agreement with the ground truth. The cardiac catherization showed that the left anterior descending artery had the complete occlusion. The signal plot demonstrated that the temporal fidelity using the DESIRE had good agreement with the ground truth and the inputs with the preserved temporal fidelity at myocardium circled by the yellow line.

Figure 4-9 presents the image quality scores from two experienced cardiologists (5, excellent; 1, poor). The SS and SMS MB=2 images were reconstructed using the networks that had the best performance (D2K32 for SS and D3K32 for SMS MB=2) and the CS-based (SMS-Slice-)L1-SPIRiT. Image quality scores were 4.5 [4.1, 4.8], 4.5 [4.3, 4.6], 3.5 [3.3, 4], and 3.5 [3.3, 3.8] for SS DESIRE and SS L1-SPIRiT, MB=2 DESIRE and MB=2 SMS-Slice-L1-SPIRiT, respectively. For both SS and SMS MB=2, the Wilcoxon signed-rank test showed that there was no statistically significant difference (p=1) between the proposed DESIRE and (SMS-Slice-)L1-SPIRiT reconstructions.

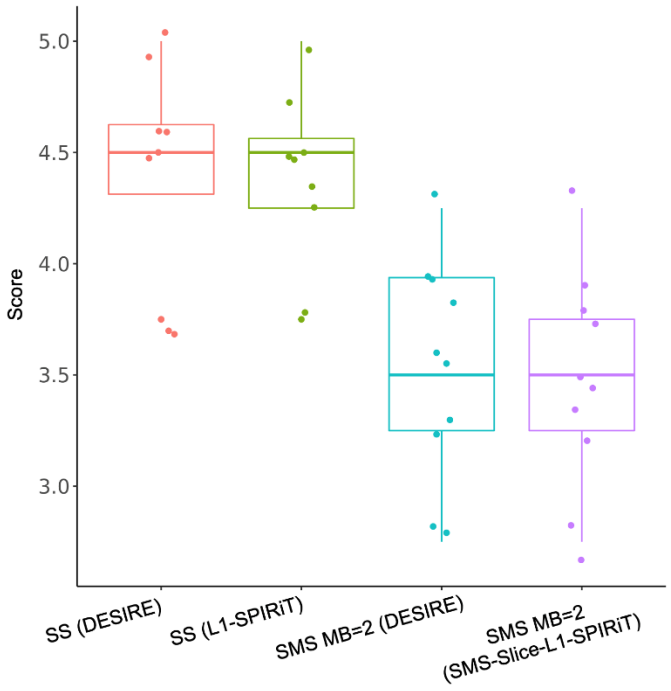

Figure 4-9. Image quality scores for prospective SS and SMS MB=2 acquisitions from two experienced cardiologists (5, excellent; 1 poor).

The image reconstruction time using the proposed DESIRE technique is significantly shorter than that of the reference L1-SPIRiT technique. Table 4-4 demonstrated the image reconstruction time using the proposed DESIRE technique. The reconstruction of each dynamic perfusion image series with 40 temporal frames can be achieved within a second, showing the potential of online reconstruction and advancing the clinical translation. However, the reconstruction time for the ground-truth L1-SPIRiT images was ~30 minutes per dynamic series.

Network Structure		Mean Reconstruction Time (ms) per Dynamic Series on a Single GPU (NVIDIA Tesla P100)
Complex-valued Convolution	3D, D2K16	374
	3D, D3K16	391
	3D, D2K32	742
	3D, D3K32	791
Non-complex-valued Convolution	3D, D2K16 (Magnitude Data)	77
	(2D+t), D2K16	89
	3D, D2K16 (Baseline)	89
	3D, D3K16	104
	3D, D2K32	161
	3D, D3K32	196

Table 4-4. Image reconstruction time of different network structures using the proposed DESIRE technique.

For spiral perfusion imaging at 1.5 T, good image quality was demonstrated with the proposed DESIRE technique. For (SMS-Slice-) L1-SPIRiT reconstruction, image quality scores were 4.5±0.7, 4.0±0.8 and 3.0±0.0 for SS, SMS MB=3 and MB=4 acquisitions. While for the proposed DESIRE technique, image quality scores were 4.4±0.8, 4.1±0.6 and 3.2±0.3 for SS, SMS MB=3 and MB=4 acquisitions (5 excellent, 1 poor). Figure 4-10 shows an example case from a patient undergoing clinical high-resolution spiral perfusion imaging with SS acquisitions. Excellent image quality was demonstrated with a score of 5 and 5 (5 excellent, 1 poor) for L1-SPIRiT and the proposed DESIRE technique, respectively. Figure 4-11 shows example cases from patient undergoing clinical high-resolution spiral perfusion imaging with SMS MB=3 (Figure 4-11-A) and MB=4 (Figure 4-11-B) acquisitions. For SMS MB=3 (Figure 4-11-A), excellent image quality was demonstrated with a score of 5 and 5 (5 excellent, 1 poor) for SMS-Slice-L1-SPIRiT and the proposed DESIRE technique, respectively. For SMS MB=4 (Figure 4-11-B), image quality scores were 3 and 3 (5 excellent, 1 poor) for SMS-Slice-L1-SPIRiT and the proposed DESIRE technique, respectively. The reconstruction time was ~800 ms per slice on a NVIDIA Tesla P100 GPU, while the reconstruction time of using (SMS-Slice-) L1-SPIRiT with GPU-accelerated NUFFT on an Intel Xeon CPU (2.40 GHz) was ~30 minutes per image series.

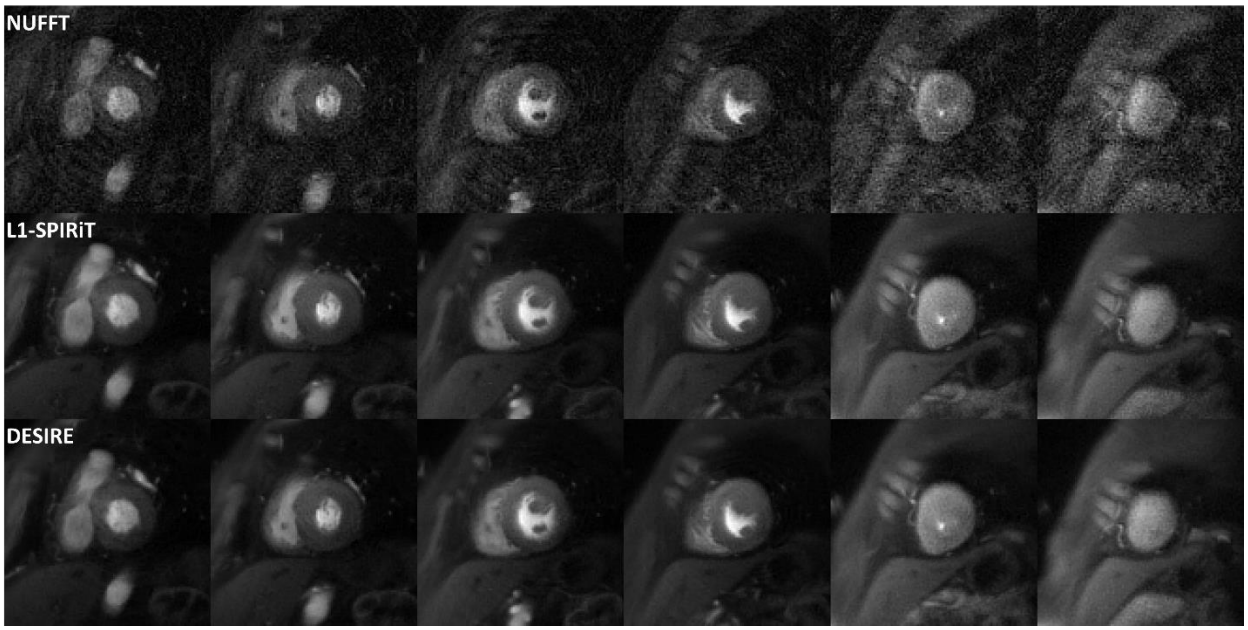

Figure 4-10. Prospective spiral perfusion images from a healthy volunteer using single-slice acquisition with 6 slices reconstructed with L1-SPIRiT and the proposed DESIRE technique. Excellent image quality was demonstrated using the proposed image reconstruction network with a score of 5 for both L1-SPIRiT and the proposed DESIRE reconstructions (5 excellent, 1 poor).

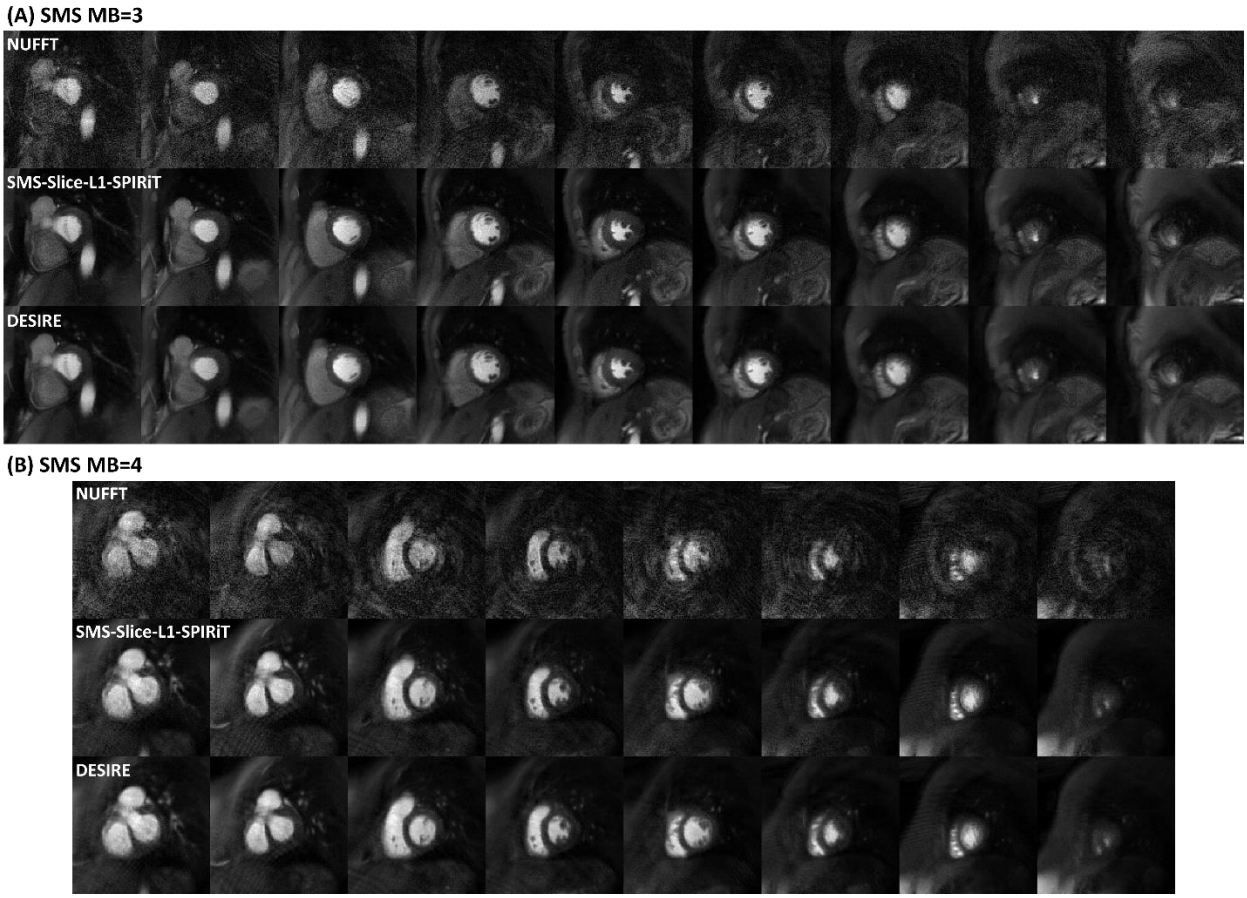

Figure 4-11. High-resolution spiral SMS perfusion imaging reconstructed with SMS-Slice-L1-SPIRiT and the proposed DESIRE technique. (A) shows an example case of 9 slices of 1.5 mm resolution perfusion images at middle time frame with an SMS factor of 3 from a patient with image quality score of 5 and 5 for SMS -Slice-L1-SPIRiT and the proposed DESIRE technique (5 excellent, 1 poor). (B) shows an example case of 8 slices with an SMS factor of 4 from a patient with image quality score of 3 and 3 for SMS -Slice-L1-SPIRiT and the proposed DESIRE technique.

4.4 Discussion

We demonstrated that high-resolution first-pass myocardial perfusion images for both SS and SMS acquisitions at 3 T and 1.5 T with whole-heart coverage can be reconstructed using the proposed DESIRE technique. After the evaluation of the complex-valued data and convolution operation and the network structures, we found that the 3D U-Net based image reconstruction networks containing more initial kernels and depth with complex-valued data produced images with the highest image quality metric and visual scores. Utilizing complex-valued convolutions had a similar effect to increasing the number of initial kernels, and typically produced better results than a similarly sized magnitude-convolutional network. Compared with the traditional

CS-based image reconstruction technique, the proposed technique significantly reduced the image reconstruction time from approximately 30 minutes to approximately 100 ms per dynamic perfusion image series after the pre-processing steps of the data, making the online image reconstruction feasible and advancing the clinical translation.

This work provides a deep learning-based rapid image reconstruction solution for spiral SS and SMS myocardial perfusion imaging. In the preprocessing steps, both coil selection and motion correction were conducted. The coil selection operation can help remove coils remote from the heart which produce spiral swirling artifacts, hence improve the quality of images input to the network. We utilized motion correction of the input data to further enhance the reconstruction performance of DESIRE. For SMS MB=2 acquisitions, two slices were acquired simultaneously with Hadamard phase modulation as we have described previously. The SMS image reconstruction aims to reduce the slice leakage and recover the image content at each slice location. The utilization of the retrospective undersampling from SS images for training and the single slice-reconstructed images as the output prevents the network from learning any artifacts which may be present when using training data reconstructed using an SMS reconstruction. To further reduce the slice leakage, we filtered the data using the calibrated through-plane kernels as a pre-processing step as we have described previously[33]. The further improvements of spiral SMS reconstructions and further validation on SMS acquisitions with a higher MB factor is of interest. The training inputs to the network were generated from the single-slice "high-apparent SNR" L1-SPIRiT reconstructions while the testing inputs were prospectively acquired SMS MB=2 images, suggesting the testing data had lower SNR level. To test whether such a SNR difference would degrade the image quality for SMS images, we trained a separate network with noise added to the retrospective inputs so that both the retrospective and prospective inputs have similar SNR levels. The prospective testing outputs for both networks trained with or without added noise had image quality scores of 4 [3.5, 4] vs. 4 [3.5 4] ($p=1$), indicating the robustness of the networks.

The choice of U-Net based image reconstruction network for spiral imaging was empirical. Of note, models which explicitly enforce data fidelity for non-Cartesian data are computationally demanding and require increased GPU memory. In our preliminary studies, we tried DL-ESPIRiT model[55] without data fidelity and the

deep cascade model[54] without data fidelity. However, both reconstruction models showed inferior performance compared with the 3D U-Net based models as shown in this work. For U-Net based models, the pooling structure enables the kernels in the deeper layers to focus on a larger receptive field to better learn the features presented in non-Cartesian imaging. Radial image reconstruction networks [51,52,63] also utilized U-Net based networks. More analysis regarding the performance of network structure for non-Cartesian imaging is necessary.

In this work, a 3D U-Net based image reconstruction network with a depth of 2 and 16 kernels at the initial layer was proposed as the baseline network. Our preliminary experiments evaluated 2D U-Net based image reconstruction networks. However, the 2D networks had limited performance likely due to the lack of including the temporal correlations in the dynamic spiral perfusion data. Compared with the 2D networks, the 3D networks showed significantly improved performance at the expense of increased training time for both SS and SMS MB=2 data. We also evaluated the performance of different kernel sizes in our preliminary experiments. Compared with the kernel size of 3 utilized in our study, the performance was not improved using a kernel size of 5 or 7 ($p=0.87$). However, using a kernel size of 5 or 7 would increase the number of trainable parameters and cost more GPU memory.

The utilization of the complex-valued data and the complex-valued convolution is also of interest for deep learning-based MR image reconstruction. The complex-valued data and convolution inherently take the phase information into account, which exploit the inherent complex nature of MR raw data[63,64,137]. In this work, networks which utilized complex-valued convolutions on complex input and output further demonstrated that the utilization of complex-valued data and complex-valued convolution could improve the reconstruction performance for spiral perfusion imaging. While the training cost for complex-valued models is higher, at the time of deployment image reconstruction is still within a second.

Assessing the influence U-Net structures could provide guidance to improve the reconstruction performance. Using more initial kernels and depth provide the network structures with more capacity to extract the features and learn the mapping function from the undersampled inputs to the ground truth. For both SS and SMS MB=2 data, an improved performance was noticed by increasing the initial kernels and network depth for

both complex-valued and non-complex-valued convolutional networks. However, for both SS and SMS MB=2, D2K32 and D3K32 had similar performance suggesting adequate capacity for the 2-layered network. By visual analysis the reconstructions using complex convolutions were slightly sharper for small trabeculations within the LV and RV cavities. For SMS MB=2 networks, the reconstruction task includes removing both in-plane aliasing due to in-plane undersampling and through-plane slice-leakage artifact due to SMS acquisition, which is a more complicated reconstruction task. Increasing the depth and the number of kernels provides the network more capacity to achieve this and the results showed improved performance.

A related MR image reconstruction study using (2D+t) convolutions demonstrated superior performance as compared to using 3D convolutions[55]. However, in our 3D U-Net based networks for spiral perfusion image reconstruction, (2D+t) convolutional network was inferior to 3D convolutional networks for SS data and had similar performance for SMS MB=2 data. Previous applications of (2D+t) for CMR image reconstruction have been using cardiac cine imaging with Cartesian data sampling and networks using RNNs with explicitly enforced data fidelity. The difference in network architecture and the difference in contrast signal variation for perfusion datasets could account for these differences. For MR image reconstructions with CNNs, the performance and analysis of convolutional units might vary due to network structure and data type. Further investigation is still warranted.

Several previously proposed image reconstruction techniques for Cartesian imaging incorporated data fidelity[54,55,58,129]. However, for non-Cartesian imaging such as radial and spiral imaging, the enforcement of data fidelity requires the NUFFT operation and gradient updates that are memory-consuming and time-consuming, especially for our 3D image reconstruction networks. To preserve the features from the input, our proposed network structure utilized a residual connection between the input and the final output layer. Furthermore, given the fact that we have achieved a high image quality with an SSIM of around 0.95 for both SS and SMS MB=2, further improvement by enforcing data fidelity might not justify the increased reconstruction time, but requires further study.

This study also has several limitations. First, the coil selection and motion correction in pre-processing steps for a single slice took around 1 minute, respectively. And the calibration process of through-plane kernel for SMS MB=2 acquisition took another 1 minute. If these are included the total reconstruction time per slice is still <3 minutes which would be clinically acceptable and compatible with online reconstruction. The optimization of the pre-processing by utilizing high-performance computers and parallel processing could further shorten the reconstruction time. Moreover, given the fact that it is not possible to acquire the fully sampled data for spiral perfusion imaging, our previously proposed CS-based image reconstruction was considered as the ground truth. Further optimization of the acquisition strategy could improve both the CS reconstructed ground truth images and the DESIRE reconstruction.

4.5 Conclusion

The proposed image reconstruction technique (DESIRE) enabled fast and high-quality image reconstructions for both SS and SMS MB=2 high-resolution first-pass spiral perfusion imaging with whole-heart coverage at 3 T and 1.5 T. Further validation will be warranted in patients to comprehensively assess the clinical value of the proposed technique.

Chapter 5: High-resolution Cartesian Perfusion Imaging with Deep learning-based Rapid Image Reconstruction

5.1 Introduction

First-pass contrast-enhanced myocardial perfusion imaging is useful for evaluating coronary artery disease (CAD)[3]. Cartesian perfusion imaging has been most frequently utilized in clinical settings[140]. However, compared with non-Cartesian imaging like spiral imaging, the Cartesian imaging has relatively low acquisition efficiency and whole-heart quantitative perfusion imaging cannot be achieved with 2D acquisition. Additionally, Cartesian imaging is less robust to motion artifacts, and the dart-rim artifact (DRA) which are known to be exacerbated by low spatiotemporal resolution[7] can be severe. Developing high-resolution Cartesian perfusion imaging with high acceleration to minimize the temporal footprint could potentially avoid the DRA, but the reconstruction time could also be significantly longer, especially for compressed sensing (CS)-based reconstruction algorithms where an iterative reconstruction process is involved. Due to the relatively low acquisition efficiency, it is difficult to achieve whole-heart coverage with Cartesian perfusion imaging techniques. To overcome this limitation, simultaneous multi-slice (SMS) perfusion imaging techniques that could enable increased slice coverage to enable whole-heart coverage[132,141], has also been developed for high-resolution Cartesian perfusion imaging.

To accelerate the image reconstruction process, data-driven and physics-driven approaches have been proposed. For data-driven approaches, as shown in Chapter 4:, denoising networks in the image space are trained in an end-to-end way. Compared with data-driven reconstruction network utilized in this work, physics-based reconstruction methods[142] incorporate data fidelity and help preserve fine features of images. Several previously proposed image reconstruction techniques for Cartesian imaging incorporated data fidelity[54,55,58,129]. However, physics-driven image reconstruction networks are not widely applied to dynamic imaging, especially for perfusion imaging.

While high-resolution SMS imaging has been demonstrated at 1.5 T using a Cartesian SSFP approach[141], we sought to develop a high-resolution Cartesian SS and SMS perfusion imaging technique with a novel deep learning-based reconstruction technique, to provides fast and high-quality perfusion imaging for 3 T applications. With SMS imaging, multiple slices can be excited and acquired at the same time, and whole-heart coverage could be achieved, to provide a relatively comprehensive clinical review and analysis. An SMS factor of two was adopted for accelerated Cartesian perfusion imaging.

5.2 Methods

5.2.1 Pulse Sequences and Data Acquisition

The Cartesian SS and SMS perfusion sequence utilized a Poisson-disc sampling patterns along phase encoding direction[143] with an in-plane acceleration factor of 4. For SMS imaging, a Hadamard phase modulation factor of 2 was adopted[72], resulting in a total of acceleration factor of 8. For SMS MB=2 phase modulation, the Hadamard phase modulation is the same as CAIPIRINHA phase modulation[73]. The saturation pulse consisted of a hard RF pulse train that was optimized at 3 T so that the specific absorption rate (SAR) could be met[33]. The saturation pulse was played out for each acquisition. A SPAIR pulse was utilized for fat saturation. The detailed acquisition parameters are listed in Table 5-1.

Acquisition Parameters	
FOV (mm^2)	320×320
Matrix Size	192×192
Spatial Resolution (mm^2)	1.67×1.67
In-plane Acceleration Factor	4
Number of Lines in k-space Center	8
TR (ms)	3
TE (ms)	1.5
Flip Angle (°)	24
Saturation Pulse Delay Time (ms)	10
Slice Thickness (mm)	8

Table 5-1. The detailed acquisition parameters for the Cartesian high-resolution perfusion imaging.

To test the proposed technique, 10 healthy volunteers and 5 patients undergoing clinically ordered CMR studies with gadolinium on 3 T scanners (MAGNETOM Prisma/Skyra; Siemens Healthineers, Erlangen,

Germany) were involved. For healthy volunteers, two contrast injections were conducted, resulting in two perfusion datasets for each subject. Totally, 25 perfusion data were involved in this study.

For single-slice acquisition, 3 slices were acquired for each subject due to the limitation of the available acquisition window in each heartbeat. While for SMS MB=2 acquisitions, 3 phase-modulated slices (6 slices) were acquired, enabling whole-heart coverage.

5.2.2 CS-based Cartesian (SMS)-L1-SENSE Reconstruction

For perfusion imaging, due to the unavailability of the fully sampled data, a state-of-art CS-based image reconstruction technique - (SMS)-L1-SENSE served as the reference for the network training. The (SMS-)L1-SENSE reconstruction method is an extension of the 2D k-t SPARSE-SENSE reconstruction[144] and can be formulated as:

$$\underset{x}{argmin}||\Phi FSx - y||_2^2 + \lambda||\Psi x||_1 \qquad \textbf{[5-1]}$$

where x is the multi-slice dynamic image series to be reconstructed, S is the coil sensitivity maps for each slice estimated from the calibration images acquired in a separate scan using a method described by Walsh et al[33], F is the fast Fourier operator that transforms the image space to k-space, Φ is the Hadamard SMS MB=2 phase modulation pattern, y is the acquired k-space data, Ψ is the finite time difference sparsifying operator, I is the identity matrix and λ balances between data consistency and sparsity. $\lambda = 0.03M_0$ was chosen as a tradeoff between image quality and temporal fidelity, where M_0 was the maximal magnitude value of the initial images derived by setting λ as 0 and executing the algorithm once. Specifically, for SS acquisitions, Φ is I.

Before image reconstruction, coil compression[118] was conducted to accelerate the reconstruction process.

The image reconstruction and processing were implemented in MATLAB (The MathWorks, Natick, MA). The algorithm was solved using a non-linear conjugate gradient algorithm with 30 iterations.

5.2.3 Deep learning-based Image Reconstruction Technique

Figure 5-1 shows the proposed physics-driven unrolled image reconstruction network. The deep learning (DL) image reconstruction network consists of several repeating modules, and each block has a denoiser and a data fidelity update. Four repetitive denoising modules with five 3D convolutional layers in each denoising module and 32 kernels in each layer were implemented, which is the maximum denoising capacity allowed in our GPU (40 GB memory) due to the limited GPU memory.

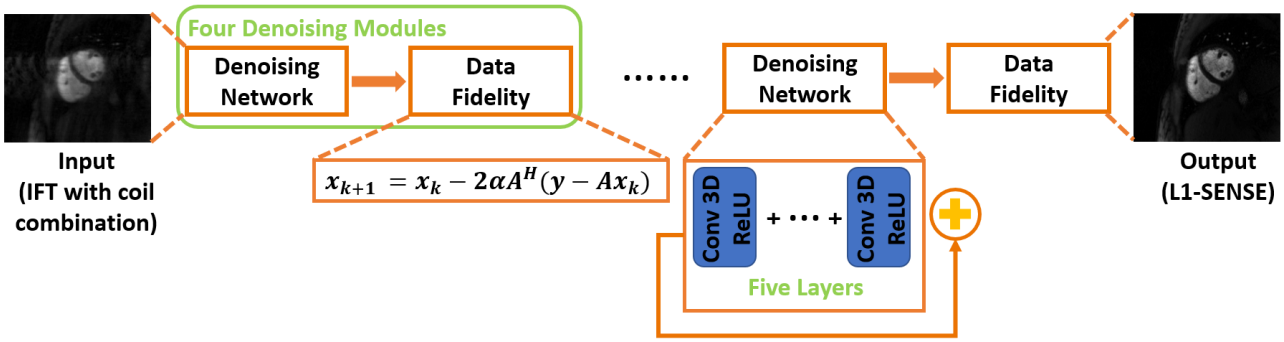

Figure 5-1. The proposed physics-driven unrolled image reconstruction network for Cartesian perfusion imaging.

To comprehensively evaluate the performance of the proposed image reconstruction network, following factors were assessed:

(a) the utilization of shared weights and non-shared weights in each denoising block:

As shown in MoDL proposed by Aggarwal et al[66], utilization of shared weights in each denoiser can provide superior performance compared with non-shared weights. In this work, we also compared the performance for the application of dynamic perfusion imaging.

(b) the utilization of the data fidelity:

The physics-driven image reconstruction network incorporates data fidelity to preserve the consistency with acquired data. The utilization of data fidelity has been demonstrated to be able to preserve details in image content[55]. To demonstrate the performance, with shared weights in each denoising module, images reconstructed

with and without data fidelity are compared. The data fidelity update is conducted using the proximal gradient descent (PGD) method:

$$x_{k+1} = x_k - 2\alpha A^H(y - Ax_k) \quad \textbf{[5-2]}$$

where the x_k is the kth image output from the denoising network before conducting data fidelity while x_{k+1}, α is the learning step size which is learnable through the model training process, y is the acquired raw data in k-space, and A is the encoding matrix. Specifically, as shown in [5-1, A could be represented as the FS for single-slice acquisition while ΦFS for SMS MB=2 acquisitions.

5.2.4 Experimental Setup

For single-slice acquisitions, the inputs to the network were a single-channel complex-valued under-sampled dynamic image series after inverse Fourier transform and optimal coil combination[135] The real and imaginary parts of the data were concatenated into two channels and the complex-valued convolution operation was enforced[145]. The outputs were concatenated real and imaginary dynamic image series reconstructed using the CS-based L1-SENSE as the reference images.

For SMS MB=2 acquisitions, initial images at each slice location were generated by setting λ shown in [5-1. The denoising module from the single-slice acquisition was enforced on each phase-demodulated slice, and then the data fidelity update was conducted jointly on both slices. To prevent slice-leakage artifact from being learned by the network, the SMS image reconstruction network was trained using the SS L1-SENSE images at each slice locations as the reference data, and the input images were the retrospective data from the two separate slice images with Hadamard SMS MB=2 phase modulations.

45 perfusion slices from 15 subjects undergoing single-slice acquisitions were used for training. To save GPU memory, each image series was cropped into a 192×192 matrix with 40 temporal frames. Each dynamic image series signal was normalized to 0-1. The training of networks was conducted on a single GPU (Tesla A100, 40 GB memory, NVIDIA, Santa Clara, CA, USA) with 100 epochs for around 20 hours. The network was implemented using PyTorch with a batch size of 1 and an l1 loss (absolute error) function using an ADAM

optimizer. The reconstruction time of the proposed DL method was also evaluated on the single aforementioned A100 GPU, and the CS-based SMS-L1-SENSE reconstruction was conducted on a server equipped with an Intel i7-7700K CPU (4.20 GHz) with 128 GB memory.

5.2.5 Image Analysis

For single-slice acquisitions, the performance of the proposed technique was evaluated on a separate 15 slices from 5 subjects that were prospectively acquired using the single-slice pulse sequence. For SMS MB=2 networks, another 18 slices from 3 subjects with prospective SMS MB=2 acquisitions were used for testing. Structural similarity index (SSIM), peak signal-to-noise ratio (PSNR) and normalized root mean square error (NRMSE) were assessed for prospective single-slice data. For both prospectively acquired single-slice and SMS MB=2 data, an experienced cardiologist blindly graded images reconstructed using the proposed networks and the CS-based (SMS-)L1-SENSE (5, excellent; 1, poor). The reconstruction time per slice (40 dynamic frames) was also evaluated.

5.2.6 Statistical Analysis

The normality of the SSIM, PSNR and NRMSE values were assessed using the Shapiro-Wilk test. Normally distributed parameters are described by their mean and standard deviation, while non-normally distributed parameters are described using the median and interquartile range (IQR). For all statistical comparisons a p-value of <0.05 were considered statistically significant. Statistical analysis was performed using SAS (version 9.4; SAS Institute Inc., Cary, NC).

5.3 Results

The difference in image quality between using shared weights and non-shared weights for each denoising block was compared. As shown in Figure 5-2, little difference was noticed and there was no statistical difference in the quantitative parameters. Images reconstructed using shared weights has an SSIM of 0.929 [0.920, 0.935], a PSNR of 34.88 [32.10, 35.68] dB, and an NRMSE of 0.193 [0.185, 0.200]. While images reconstructed using non-shared weights has an SSIM of 0.931 [0.921, 0.933], a PSNR of 34.89 [32.10, 35.70]

dB, and an NRMSE of 0.192 [0.182, 0.199]. There is no statistical difference between using shared weights and non-shared weights.

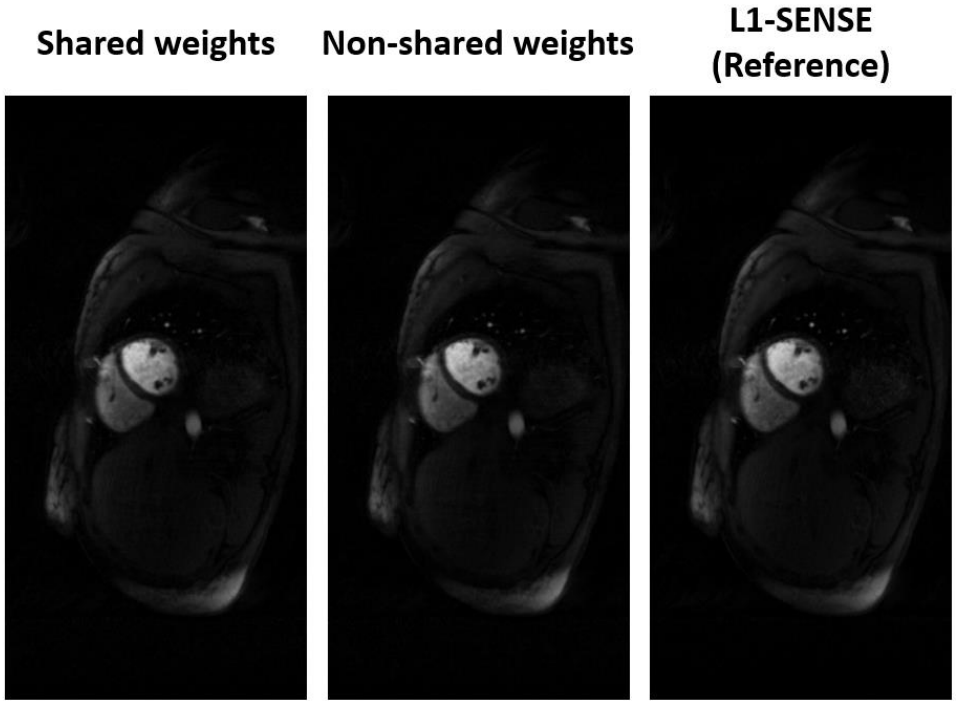

Figure 5-2. Comparison of image reconstruction network using shared weights and non-shared weights for each denoising module. Little differences are noticed, and there is no statistical difference.

Image reconstruction networks with and without data fidelity update were compared. As shown in Figure 5-2, image reconstructed using data fidelity preserve more fine details with respect to image reconstructed with network not incorporating data fidelity. Image reconstructed with data fidelity has an SSIM of 0.929 [0.920, 0.935], a PSNR of 34.88 [32.10, 35.68] dB, and an NRMSE of 0.193 [0.185, 0.200]. While images reconstructed with network without data fidelity has an SSIM of 0.911 [0.900, 0.921], a PSNR of 33.45 [31.95, 34.58] dB, and an NRMSE of 0.211 [0.200, 0.228] ($p=0.01$). This analysis demonstrates the necessity of incorporating data fidelity into the image reconstruction.

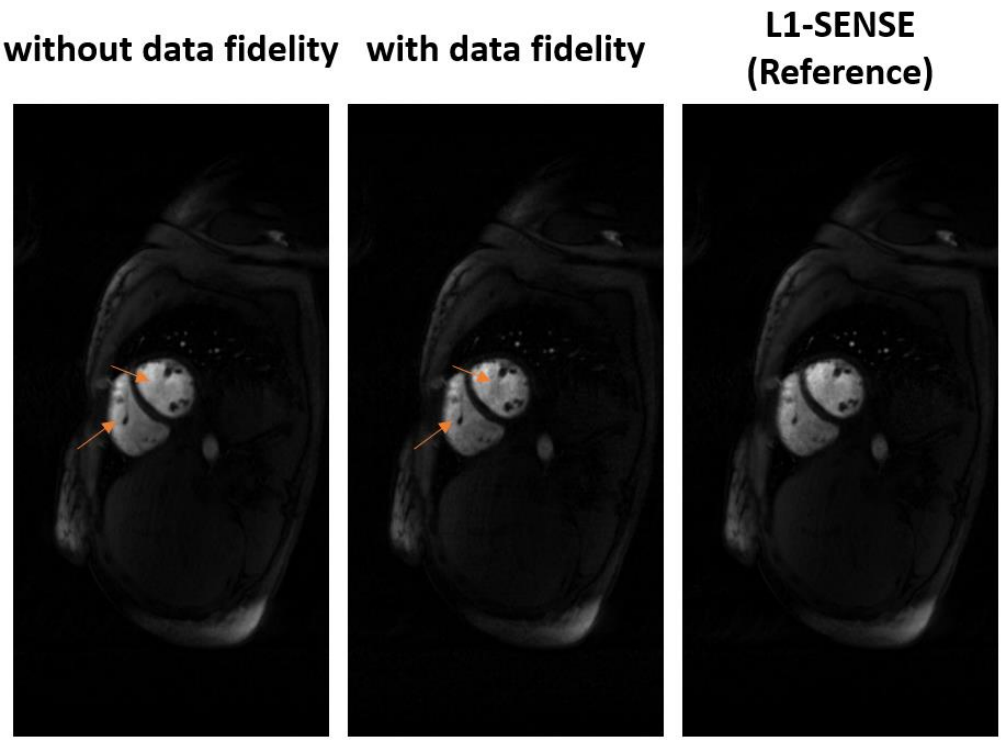

Figure 5-3. Comparison of image reconstruction network with and without data fidelity. As pointed out by arrows, fine features are preserved by incorporating data fidelity.

With the above analysis, we utilized shared weights in each denoiser, four repetitive denoising modules and data fidelity was enforced. Both single slice acquisitions and SMS MB=2 acquisitions were assessed by cardiologist using results from such network setting.

The DL image reconstruction results from single-slice acquisitions had SSIM, PSNR and NRMSE of 0.944 [0.933, 0.952], 36.24 [35.02, 37.25] dB and 0.162 [0.132, 0.175] with respect to the reference (L1-SENSE), demonstrating good performance of the proposed method. The image reconstruction time for (SMS)-L1-SENSE was 45 minutes per slice while the reconstruction time using proposed deep learning method was around 8 seconds, demonstrating a rapid and high-quality image reconstruction.

For single-slice acquisitions, the image quality scores were 4.5 [4 ,5] and 3.6 [3.5, 4] for L1-SENSE and DL reconstructions, respectively. While for SMS MB=2 acquisitions, the image quality scores were 3.7 [2.5, 4.5] and 3.3 [2.4, 4] for SMS-L1-SENSE and DL reconstructions.

Figure 5-4 shows an example case from a healthy volunteer undergoing clinical Cartesian single-slice perfusion imaging with an image quality score of 4 and 3 for L1-SENSE and DL image reconstruction, respectively, demonstrating the high image quality of the proposed method.

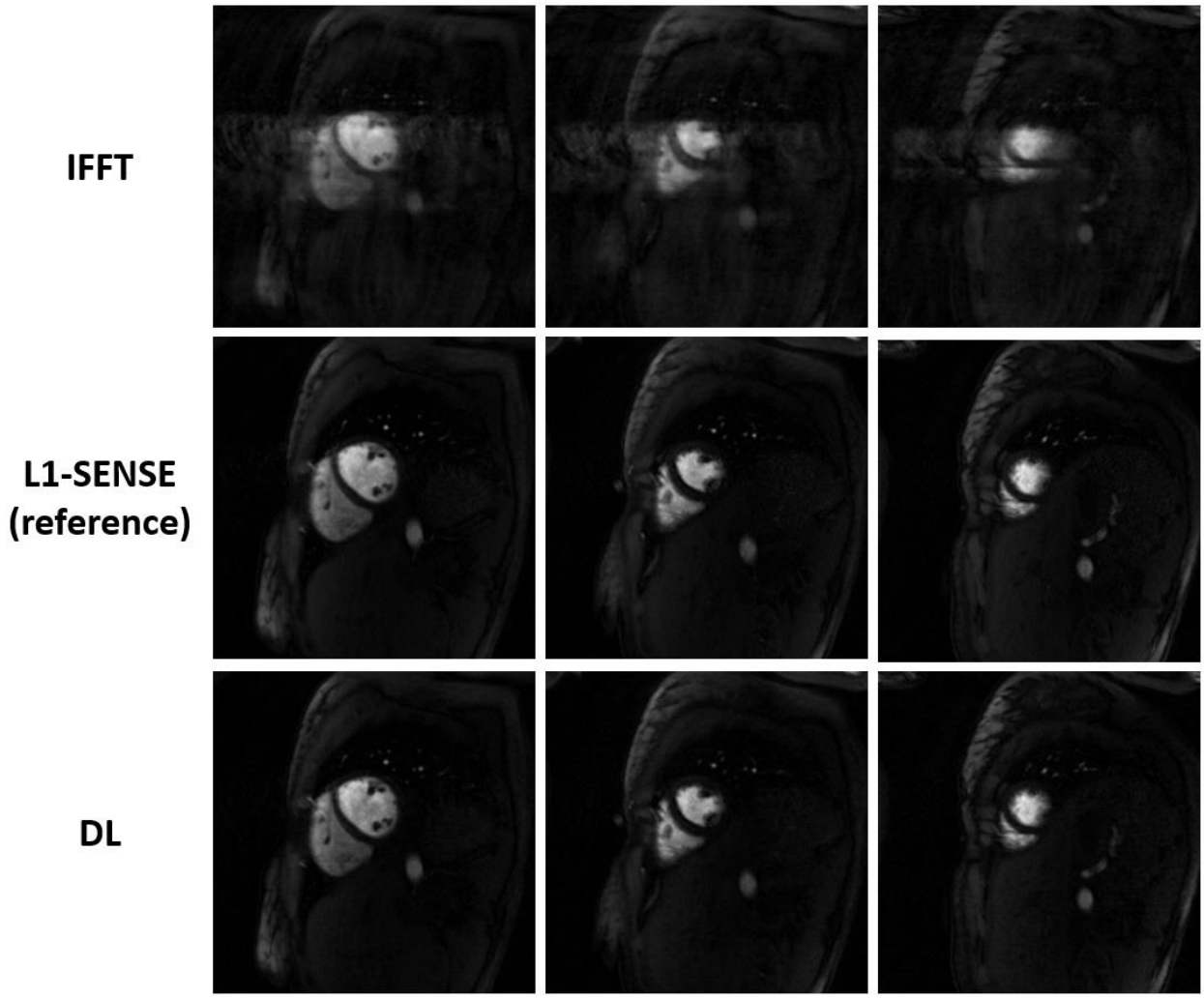

Figure 5-4. Cartesian perfusion imaging from a healthy volunteer underwent single-slice acquisition with an in-plane acceleration factor of 4. Image is reconstructed using the inverse Fast Fourier transform (IFFT), deep learning (DL), and compressed sensing (CS) method.

Figure 5-5 shows an example case from a healthy volunteer undergoing clinical Cartesian SMS MB=2 perfusion imaging with an image quality score of 4.5 and 4 for SMS-L1-SENSE and DL reconstruction, respectively, demonstrating the good performance of the proposed image reconstruction method.

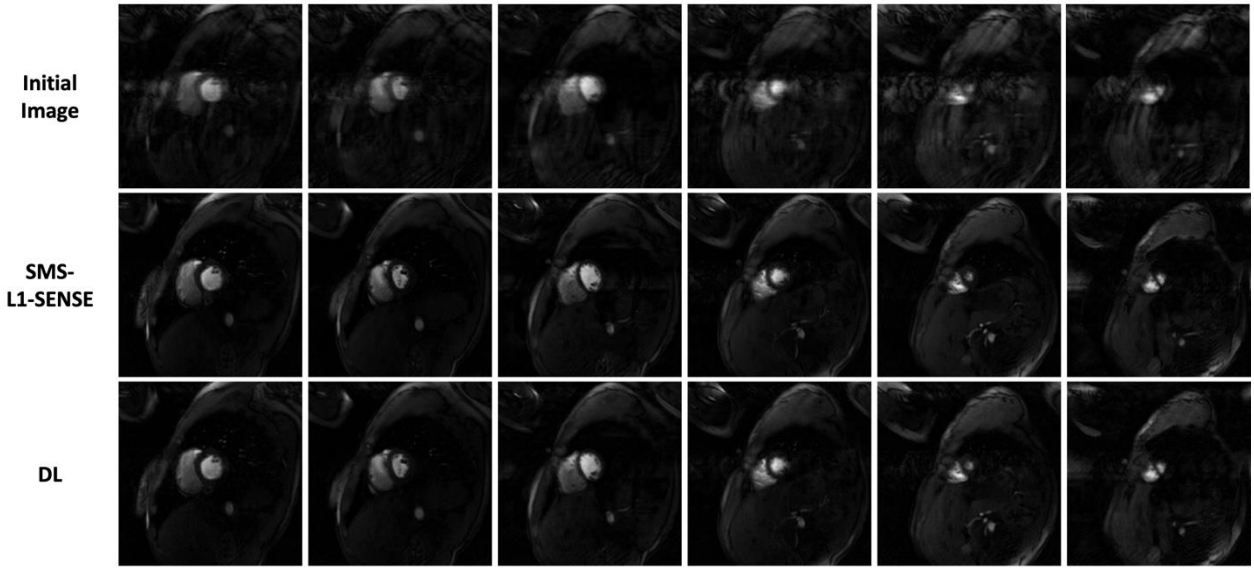

Figure 5-5. Cartesian perfusion imaging from a healthy volunteer underwent SMS MB=2 acquisition with whole-heart coverage. Image is reconstructed using the deep learning (DL) and compressed sensing (CS) method (SMS-L1-SENSE).

5.4 Discussion

We demonstrated high-quality high-resolution Cartesian first-pass myocardial perfusion imaging for both SS and SMS MB=2 acquisitions at 3 T and images can be reconstructed using the proposed rapid DL image reconstruction technique. The proposed physics-driven DL-based image reconstruction approach demonstrated rapid and high-quality reconstructions, making online reconstruction feasible so that results could be provided to doctors in a timely manner.

The model we adopted used shared weights among different denoising modules. Compared with networks trained using different weights for each module, utilizing shared weights could reduce the number of trainable parameters significantly and save the GPU memory cost. However, by comparing networks without using shared weights, image reconstruction performance was similar.

The utilization of data fidelity could help enhance the image reconstruction performance and perverse some fine details shown in the image. In this work, the proximal gradient decent method was utilized to conduct data fidelity update. Optimization of the data fidelity update such as utilizing conjugate gradient descent could further improve the performance[66].

There are also several limitations in this work. Firstly, the coil compression in pre-processing steps for a single slice took around 1 minute and the image reconstruction took around 8 seconds. The optimization of the pre-processing by utilizing high-performance computers and parallel processing could further shorten the time of pre-processing. Optimization of the data fidelity step could further shorten the inference time. Exploration of deep learning-based image reconstruction approach for SMS imaging is still of interest. Moreover, given the fact that it is impossible to acquire the fully sampled data for perfusion imaging with whole-heart coverage, a state-of-art CS-based image reconstruction method (L1-SENSE) was considered as the reference in the network training process. Further optimization of the acquisition strategy could improve both the CS reconstructed images and the deep learning-based image reconstructions.

5.5 Conclusion

The proposed high-resolution Cartesian perfusion imaging with deep learning-based rapid image reconstruction network enabled fast and high-quality image reconstructions for both SS and SMS MB=2 high-resolution first-pass Cartesian perfusion imaging. Further validation will be warranted in patients to comprehensively assess the clinical value of the proposed technique.

Chapter 6: Conclusions and Future Works

6.1 Overview of Findings

The overall goal of this dissertation is to develop advanced techniques for fast high-resolution first pass CMR perfusion imaging with whole-heart coverage.

Firstly, high spatial resolution (1.25×1.25 mm^2) spiral perfusion imaging at 3 T was proposed. The proposed single slice and SMS imaging incorporated OVS imaging to further advance the acquisition efficiency. Pulse sequences were carefully optimized so that high spatial-temporal resolution of spiral perfusion imaging could achieved, and SAR limitation could be met at 3 T. On the reconstruction side, to further improve the reconstruction performance for SMS imaging, a novel reconstruction approach that incorporated a through-plane kernel into the CS-based image reconstruction pipeline to reduce the slice leakage was proposed and evaluated. Results demonstrated superior performance of the technique using the through-plane kernel as compared to the technique not using the through-plane kernel. To compensate for respiratory motion, motion compensation was incorporated into the image reconstruction pipeline for both single slice and SMS acquisitions. After image reconstruction, the automatic B_0 inhomogeneity correction was incorporated to further advance the image quality. Overall, high image quality was demonstrated for spiral perfusion imaging with whole-heart coverage at 3 T for both SS and SMS acquisitions with and without OVS in human studies. In direct comparison, the interleaved single slice spiral approach without OVS had the highest image quality. With high resolution, the increased transmural resolution may improve assessment of myocardial perfusion gradients, and the whole-heart coverage may improve quantification of ischemic burden. Further validation will be required in patients undergoing stress CMR to assess the clinical value of high-resolution perfusion imaging.

However, one of the limitations of the proposed iterative CS-based image reconstruction algorithm for spiral perfusion imaging was the long reconstruction time, impeding the clinical translation of the proposed technique. To overcome this limitation, a DEep learning-based rapid Spiral Image Reconstruction (DESIRE) was proposed and implemented for both single slice and SMS imaging with an MB factor of 2. The image reconstruction network was a 3D U-Net based network that took CS-based L1-SPIRiT reconstructions as

reference. We systematically assessed the performance of the proposed network in terms of four different factors: (1) the choice of magnitude-valued and complex-valued data types, (2) the difference of complex-valued and real-valued convolutions, (3) the influence of network structures including depth and the number of kernels at the initial layer for 3D networks and (4) the comparison between the (2D+t) and the 3D convolutional unit. Results demonstrated that, complex-valued data inputs using the 3D complex-valued convolutional network with more depth and kernels in the initial layer had the best performance. The proposed method demonstrated high image quality for both spiral single slice and SMS imaging with an MB factor of up to 3. Specifically, for SMS MB=2 acquisitions, to prevent slice-leakage artifact from being learned by the SMS network, the reference image data were SS L1-SPIRiT images at each slice locations, and the input images were the retrospective data from the two separate slice images with Hadamard SMS MB=2 phase modulations. The proposed method could shorten the reconstruction time from around 30 minutes per image series (40 dynamic frames) at a slice location to around 1 second. With an online implementation this would allow for rapid reconstruction facilitating clinical translation. The proposed DESIRE technique enables rapid image reconstruction for both single-slice and SMS imaging with high spatial resolution and respiratory motion correction. Specifically, we also demonstrated that the proposed technique could provide high-quality reconstruction for SMS spiral perfusion imaging at 1.5 T with an SMS acceleration factor of 3 and 4.

As Cartesian perfusion techniques are most commonly deployed clinically, we also sought to evaluate the proposed CS, SMS, and deep-learning techniques for Cartesian high-resolution perfusion imaging for both single slice and SMS acquisitions with an MB factor of 2 using a 2D Poisson-Disc incoherent sampling pattern along temporal dimension. With SMS MB=2 acquisitions, whole-heart coverage for Cartesian perfusion imaging could be achieved. To overcome the limitation of the long reconstruction time for the iterative CS-based Cartesian (SMS)-L1-SENSE reconstructions, a deep learning-based physics-driven rapid image reconstruction network was proposed. The proposed unrolled image reconstruction network took CS-based L1-SENSE results as reference and incorporated both image denoising blocks and data fidelity so that fine features could be preserved. For SMS MB=2 acquisitions, to prevent slice-leakage artifact from being learned, the reference image data were SS L1-SNESE reconstruction results at each slice locations, and the input images were the

retrospective data from the two separate slice images with Hadamard phase modulations. Utilizing the proposed DL-based image reconstruction network, the reconstruction time could be shortened from 45 minutes dynamic series at a slice location to around 8 seconds. This proposed approach could provide rapid and high-quality image reconstruction for both single slice and SMS MB=2 high-resolution Cartesian perfusion imaging, demonstrating the potential for clinical translation. Further validation and comparison between spiral and Cartesian quantitative perfusion imaging will be required in patients undergoing stress CMR to assess the clinical value of the Cartesian versus spiral perfusion imaging techniques.

6.2 Future Work

6.2.1 Deep learning-based Rapid Image Reconstruction for other Spiral Imaging Modalities

The proposed DESIRE reconstruction network was essentially a denoising network for spiral dynamic imaging, which motivates the applications of the network on other dynamic imaging applications such as spiral real-time cine imaging. Iterative CS image reconstruction of spiral imaging is time-consuming, and a high-resolution real-time cardiac cine imaging at 1.5 T using rapid spiral acquisitions and deep learning-based imaging reconstruction for both bSSFP and GRE imaging could make high-quality and rapid online reconstruction for cardiac cine imaging feasible.

Figure 6-1 shows examples from the testing data for the bSSFP (Figure 6-1-A) and GRE (Figure 6-1-B) imaging, respectively. The case shown in Figure 6-1-A had an image quality score of 4.5 for L1-SENSE and DESIRE. The case shown in Figure 6-1-B had an image quality score of 4 for both L1-SENSE and DESIRE.

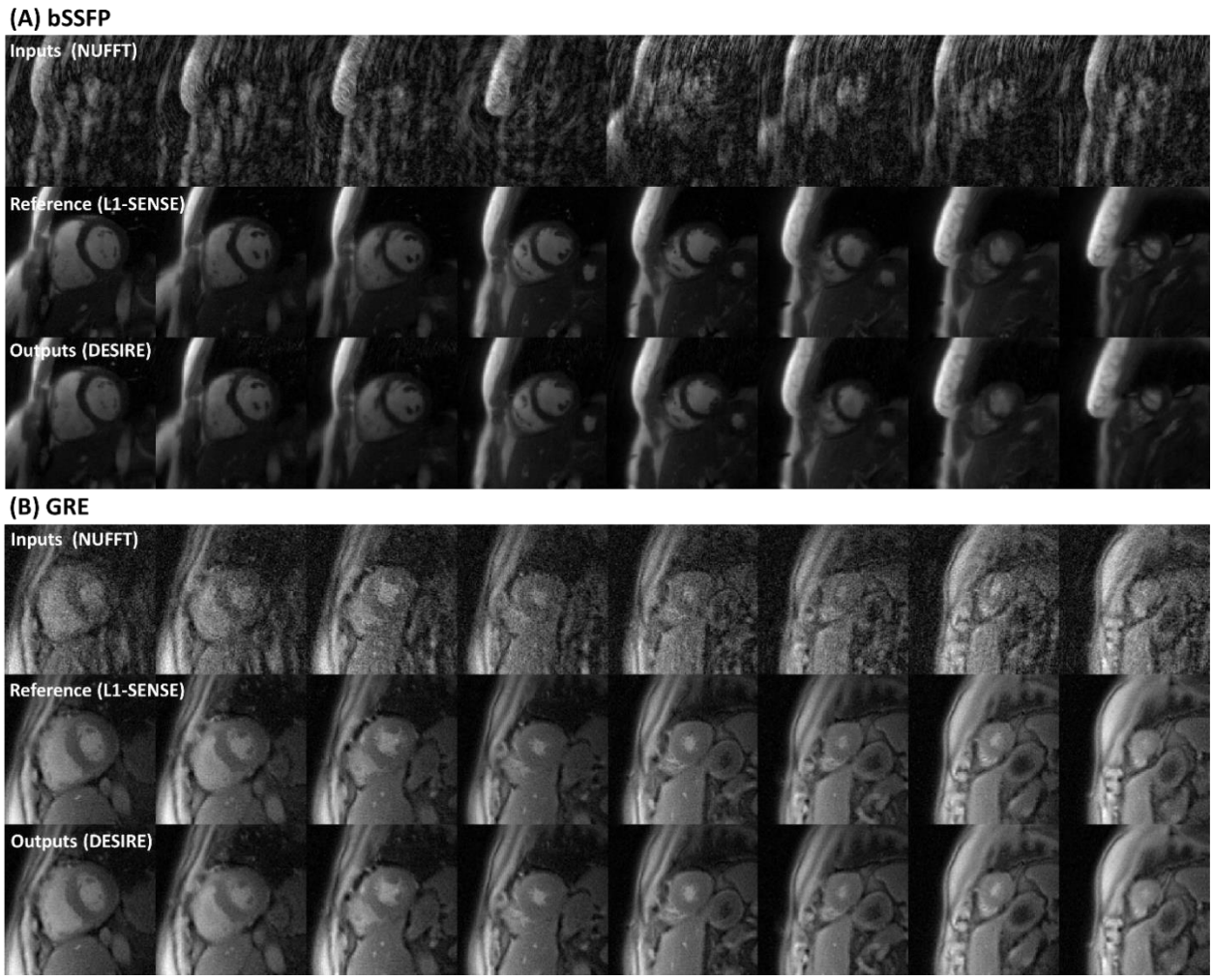

Figure 6-1. Cardiac bSSFP and GRE cine imaging at 1.5 T reconstructed using the proposed DESIRE technique and the spiral L1-SENSE served as the reference.

Besides, the proposed method could potentially be applied to spiral T_1 mapping. However, signal evolution in T_1 mapping should be carefully analyzed since the network might potentially bias the temporal fidelity of the signal evolutions. Incorporation of physics-driven methods that incorporate data fidelity for spiral imaging might further enhance the image reconstruction performance.

6.2.2 Deep learning-based Rapid Quantification Analysis for Spiral Perfusion Imaging

With the rapid image reconstruction technique, rapid image reconstruction could be achieved with a clinically acceptable time frame (<1 second). It is also essential to provide rapid analysis of the quantification of spiral perfusion imaging. To date, the current available online quantification techniques do not include the rapid

online reconstructions[146,147]. The rapid online image reconstruction framework for both spiral and Cartesian perfusion imaging could be incorporated with deep learning-based rapid motion correction and quantification techniques.

Appendix - Vita of the Author

EDUCATION

Beijing Jiaotong University, Beijing, China ***Sept 2013 – Jul 2017***

BE in Biomedical Engineering (with honor)

JOURNAL PUBLICATONS

1. **Wang J,** Weller DS, Kramer CM, Salerno M. DEep learning-based rapid Spiral Image REconstruction (DESIRE) for high-resolution spiral first-pass myocardial perfusion imaging. NMR in Biomedicine. 2021;e4661. doi:10.1002/nbm.4661.
2. **Wang J**, Yang Y, Weller D, Zhou R, Van Houten M, Sun C, Epstein F, Meyer C, Kramer C, Salerno M. High spatial resolution spiral first-pass myocardial perfusion imaging with whole-heart coverage at 3 T. *Magn. Reson. Med. 2021; 86: 648– 662.*
3. Zhou R, **Wang J**, Weller D, Yang Y, Mugler J, Salerno M. Free-breathing self-gated continuous-IR spiral T1 mapping: Comparison of dual flip-angle and Bloch-Siegert B1-corrected techniques. *Magn. Reson. Med. 2022;1- 13.*
4. Zhou R, Weller D, Yang Y, **Wang J**, Jeelani H, Mugler J, Salerno M. Dual excitation flip angle simultaneous Cine And T1 mapping using SPiral Acquisition with Respiratory and Cardiac Self-gating (CAT-SPARCS). *Magn. Reson. Med. 2021; 86: 82– 96.*

CONFERENCE PROCEEDINGS

1. **Wang J**, Zhou R, Wang X, Awad M, Salerno M. Free-breathing High-resolution Spiral Real-time Cardiac Cine Imaging at 1.5 T with DEep learning-based Spiral Image REconstruction (DESIRE). *In Proceedings of the ISMRM 30th Annual Scientific Sessions, London, England, UK, 2022 (oral Power Pitch).*
2. **Wang J**, Rodriguez Lozano P, Salerno M. High-resolution Spiral First-pass Myocardial Perfusion Imaging at 1.5 T with DEep learning-based rapid Spiral Image REconstruction (DESIRE). *In Proceedings of the ISMRM 30th Annual Scientific Sessions, London, England, UK, 2022 (digital poster).*
3. **Wang J**, Rodriguez Lozano P, Salerno M. High-resolution Spiral First-pass Myocardial Perfusion Imaging using DEep learning-based rapid Spiral Image REconstruction (DESIRE) at 1.5 T. *In Proceedings of the SCMR 25th Annual Scientific Sessions, 2022 (oral presentation).*
4. **Wang J**, Zhou R, Wang X, Awad M, Salerno M. DEep learning-based rapid Spiral Image REconstruction (DESIRE) for Free-breathing High-resolution Spiral Real-time Cardiac Cine Imaging at 1.5 T. *In Proceedings of the SCMR 25th Annual Scientific Sessions, 2022 (poster).*
5. **Wang J**, Weller D, Salerno M. DESIRE: DEep learning-based rapid Spiral Imaging Reconstruction for high-resolution spiral first-pass myocardial perfusion imaging with whole-heart coverage. *In Proceedings of the SCMR 24th Annual Scientific Sessions, 2021 (oral presentation, ECA finalist).*
6. **Wang J**, Weller DS, Rodriguez Lozano P, Salerno M. High-resolution Spiral First-pass Myocardial Perfusion Imaging using DEep learning-based rapid Spiral Image REconstruction (DESIRE). *In Proceedings of the ISMRM 29th Annual Meeting and Exhibition, 2021, p. 23 (digital poster).*
7. **Wang J**, Zhou R, Salerno M. Free-breathing High-resolution Spiral Real-time Cardiac Cine Imaging using DEep learning-based rapid Spiral Image REconstruction (DESIRE). *In Proceedings of the ISMRM 29th Annual Meeting and Exhibition, 2021, p. 877 (digital poster).*

8. **Wang J**, Yang Y, Zhou R, Sun C, Jacob M, Weller DS, Epstein F, Salerno M. High resolution spiral simultaneous multi-slice first-pass perfusion imaging with whole-heart coverage at 1.5 T and 3 T. *In Proceedings of the ISMRM 28th Annual Meeting and Exhibition, 2020, p. 1313 (oral presentation, Summa cum Laude Awards).*

9. **Wang J**, Yang Y, Zhou R, Jacob M, Weller DS, Salerno M. SMS Slice L1-SPIRiT: auto-calibrated image reconstruction for spiral simultaneous multi-slice first-pass perfusion imaging with 1.25 mm resolution and whole heart coverage at 3T. *In Proceedings of the SCMR 23rd Annual Scientific Sessions, Orlando, Florida, USA, 2020 (oral presentation).*

10. **Wang J**, Yang Y, Feng X, Weller DS, Salerno M. Analysis of Sampling Strategies for Convolutional Neural Network Based Cardiac Magnetic Resonance Image Reconstruction. *In Proceedings of the ISMRM 27th Annual Meeting and Exhibition, Montreal, Quebec, Canada, 2019, p. 2155 (digital poster).*

11. **Wang J,** Wang F, Wang Y, Ning J, Dong Z, Ying K, Chen H. Weighted k-t SPIRiT with Golden Angle Radial Sampling for Dynamic Contrast-Enhanced Liver Imaging. *In Proceedings of the ISMRM 25th Annual Meeting and Exhibition, Honolulu, Hawaii, USA, 2017, p. 3201 (digital poster).*

12. Wang X, **Wang J,** Zhou R, Salerno M. Rapid Free-breathing 3D SPirAl Respiratory and Cardiac Self-gated (SPARCS) Cine Acquisition Using an Undersampled Stack-of-Spirals. *In Proceedings of the ISMRM 30th Annual Scientific Sessions, London, England, UK, 2022 (digital poster).*

13. Awad M, **Wang J,** Feng X, Zhou R, Salerno M. Deep learning-based Automatic Analysis for Free-breathing High-resolution Spiral Real-time Cardiac Cine Imaging at 3T. *In Proceedings of the ISMRM 30th Annual Scientific Sessions, London, England, UK, 2022 (digital poster).*

14. Rodriguez Lozano P, Pan J, **Wang J,** Robinson A, Van Houten M , Kramer CM, Salerno M. Clinical Evaluation of High Resolution Stress Myocardial Perfusion Imaging with Whole Heart Coverage at 3T. *In Proceedings of the SCMR 25th Annual Scientific Sessions, 2022 (digital poster).*

15. Wang X, Zhou R, **Wang J,** Van Houten M, Salerno M. Clinical Validation of Spiral Acquisition with Respiratory correction and Cardiac Self-gating (SPARCS) using bSSFP and GRE sequences at 1.5T. *In Proceedings of the SCMR 25th Annual Scientific Sessions, 2022 (digital poster).*

16. Zhou R, Yang Y, **Wang J,** Mugler JP, Salerno M. Free-breathing self-gated continuous-IR spiral T1 mapping: A comparison of dual flip-angle and Bloch-Siegert B1-corrected techniques. *In Proceedings of the SCMR 25th Annual Scientific Sessions, 2022 (oral presentation).*

17. Zhou R, Weller DS, Yang Y, **Wang J**, Mugler J, Salerno M. Comparison of free-breathing self-gated continuous IR spiral T1 mapping: dual flip angle versus Bloch-Siegert B1-corrected techniques. *In Proceedings of the ISMRM 29th Annual Meeting and Exhibition, 2021, p. 1545 (oral presentation).*

18. Zhou R, Weller DS, Yang Y, **Wang J**, Mugler J, Salerno M. Free breathing simultaneous cine and T1 mapping spiral acquisition with respiratory correction at 3T using dictionary learning. *In Proceedings of the SCMR 23rd Annual Scientific Sessions, Orlando, Florida, USA, 2020 (poster).*

19. Robinson AA, Yang Y, Van Houten M, **Wang J**, Epstein F, Meyer C, Kramer CM, Salerno M. Diagnostic Accuracy of High Resolution Stress Myocardial Perfusion. *In Proceedings of the SCMR 23rd Annual Scientific Sessions, Orlando, Florida, USA, 2020 (best moderated E-poster).*

HONORS & AWARDS

SCMR Seed Grant Awardee	SCMR 2022
SCMR Registration Award	SCMR 2022
Early Career Award Finalist	SCMR 2021
Summa cum Laude Awards	ISMRM 2020
ISMRM Education Stipend	ISMRM 2017, 2019 and 2020

Bibliography

1. Virani SS, Alonso A, Benjamin EJ, et al. Heart Disease and Stroke Statistics—2020 Update: A Report From the American Heart Association. *Circulation* 2020;141.

2. Mozaffarian D, Benjamin EJ, Go AS, et al. Executive Summary: Heart Disease and Stroke Statistics—2016 Update. :8.

3. Salerno M, Beller GA. Noninvasive Assessment of Myocardial Perfusion. *Circ. Cardiovasc. Imaging* 2009;2:412–424.

4. Greenwood JP, Maredia N, Younger JF, et al. Cardiovascular magnetic resonance and single-photon emission computed tomography for diagnosis of coronary heart disease (CE-MARC): a prospective trial. *The Lancet* 2012;379:453–460.

5. Jaarsma C, Leiner T, Bekkers SC, et al. Diagnostic Performance of Noninvasive Myocardial Perfusion Imaging Using Single-Photon Emission Computed Tomography, Cardiac Magnetic Resonance, and Positron Emission Tomography Imaging for the Detection of Obstructive Coronary Artery Disease: A Meta-Analysis. *J. Am. Coll. Cardiol.* 2012;59:1719–1728.

6. Lipinski MJ, McVey CM, Berger JS, Kramer CM, Salerno M. Prognostic Value of Stress Cardiac Magnetic Resonance Imaging in Patients With Known or Suspected Coronary Artery Disease: A Systematic Review and Meta-Analysis. *J. Am. Coll. Cardiol.* 2013;62:826–838.

7. Bella EVRD, Parker DL, Sinusas AJ. On the dark rim artifact in dynamic contrast-enhanced MRI myocardial perfusion studies. *Magn. Reson. Med.* 2005;54:1295–1299.

8. Yang Y, Kramer CM, Shaw PW, Meyer CH, Salerno M. First-pass myocardial perfusion imaging with whole-heart coverage using L1-SPIRiT accelerated variable density spiral trajectories: Whole Heart Spiral Myocardial Perfusion Imaging. *Magn. Reson. Med.* 2016;76:1375–1387.

9. Yang Y, Meyer CH, Epstein FH, Kramer CM, Salerno M. Whole-heart spiral simultaneous multi-slice first-pass myocardial perfusion imaging. *Magn. Reson. Med.* 2019;81:852–862.

10. Smith TB, Nayak KS. Reduced field of view MRI with rapid, B1-robust outer volume suppression. *Magn. Reson. Med.* 2012;67:1316–1323.

11. Yang Y, Zhao L, Chen X, et al. Reduced field of view single-shot spiral perfusion imaging: rFOV Single-Shot Spiral Perfusion Imaging. *Magn. Reson. Med.* 2018;79:208–216.

12. Yang Y, Robinson A, Mathew R, Kramer C, Salerno M. Initial Clinical Evaluation of Quantitative Ultra-high Resolution First-pass Spiral Perfusion Imaging with Whole Heart Coverage in Patients with Ischemic Heart Disease at 3T. In: Proceedings of the 27th Annual Meeting of ISMRM, Montréal, QC, Canada, 2019. p 1229.

13. Robinson A, Yang Y, Van Houten M, et al. Diagnostic Accuracy of High Resolution Stress Myocardial Perfusion. In: Proceedings of the SCMR 23rd Annual Scientific Sessions, Orlando, Florida, USA, 2020. Abstract 751192.

14. Pan JA, Robinson AA, Yang Y, et al. Diagnostic Accuracy of Spiral Whole-Heart Quantitative Adenosine Stress Cardiovascular Magnetic Resonance With Motion Compensated L1-SPIRIT. *J. Magn. Reson. Imaging* 2021;54:1268–1279.

15. Chiribiri A, Hautvast GLTF, Lockie T, et al. Assessment of Coronary Artery Stenosis Severity and Location. *JACC Cardiovasc. Imaging* 2013;6:600–609.

16. Hsu L-Y, Groves DW, Aletras AH, Kellman P, Arai AE. A Quantitative Pixel-Wise Measurement of Myocardial Blood Flow by Contrast-Enhanced First-Pass CMR Perfusion Imaging. *JACC Cardiovasc. Imaging* 2012;5:154–166.

17. Klocke FJ, Lee DC. Probing Transmural Myocardial Perfusion With CMR∗. *JACC Cardiovasc. Imaging* 2014;7:23–25.

18. Motwani M, Maredia N, Fairbairn TA, et al. High-Resolution Versus Standard-Resolution Cardiovascular MR Myocardial Perfusion Imaging for the Detection of Coronary Artery Disease. *Circ. Cardiovasc. Imaging* 2012;5:306–313.

19. Ma D. Magnetic Resonance Fingerprinting. *Case Western Reserve University*.

20. Setsompop K. Design Algorithms for Parallel Transmission in Magnetic Resonance Imaging. *Massachusetts Institute of Technology*; 2008.

21. Simonetti OP, Ahmad R. Low-Field Cardiac Magnetic Resonance Imaging: A Compelling Case for Cardiac Magnetic Resonance's Future. *Circ. Cardiovasc. Imaging* 2017;10:e005446.

22. Brown RW, Cheng YCN, Haacke EM, Thompson MR, Venkatesan R. Magnetic Resonance Imaging: Physical Principles and Sequence Design. *Wiley*; 2014.

23. Nishimura DG. Principles of Magnetic Resonance Imaging. *Stanford University*; 1996.

24. Lustig M. Sparse MRI. *Stanford University*; 2008.

25. MRI Questions and Answers; MR imaging physics & technology. Questions and Answers in MRI. http://mriquestions.com/.

26. Lauterbur PC. Image Formation by Induced Local Interactions: Examples Employing Nuclear Magnetic Resonance. *Nature* 1973;242:190–191.

27. Ahn CB, Kim JH, Cho ZH. High-Speed Spiral-Scan Echo Planar NMR Imaging-I. *IEEE Trans. Med. Imaging* 1986;5:2–7.

28. Meyer CH, Hu BS, Nishimura DG, Macovski A. Fast Spiral Coronary Artery Imaging. *Magn. Reson. Med.* 1992;28:202–213.

29. Spielman DM, Pauly JM, Meyer CH. Magnetic resonance fluoroscopy using spirals with variable sampling densities. *Magn. Reson. Med.* 1995;34:388–394.

30. Adalsteinsson E, Star-Lack J, Meyer CH, Spielman DM. Reduced spatial side lobes in chemical-shift imaging. *Magn. Reson. Med.* 1999;42:314–323.

31. Zhou R, Yang Y, Mathew RC, et al. Free-breathing cine imaging with motion-corrected reconstruction at 3T using SPiral Acquisition with Respiratory correction and Cardiac Self-gating (SPARCS). *Magn. Reson. Med.* 2019;82:706–720.

32. Zhou R, Weller DS, Yang Y, et al. Dual-excitation flip-angle simultaneous cine and T1 mapping using spiral acquisition with respiratory and cardiac self-gating. *Magn. Reson. Med.* 2021;86:82–96.

33. Wang J, Yang Y, Weller DS, et al. High spatial resolution spiral first-pass myocardial perfusion imaging with whole-heart coverage at 3 T. *Magn. Reson. Med.* 2021;86:648–662.

34. Shin T, Nayak KS, Santos JM, Nishimura DG, Hu BS, McConnell MV. Three-dimensional first-pass myocardial perfusion MRI using a stack-of-spirals acquisition. *Magn. Reson. Med.* 2013;69:839–844.

35. Pipe JG. Motion correction with PROPELLER MRI: Application to head motion and free-breathing cardiac imaging. *Magn. Reson. Med.* 1999;42:963–969.

36. Noll DC. Multishot rosette trajectories for spectrally selective MR imaging. *IEEE Trans. Med. Imaging* 1997;16:372–377.

37. Gurney PT, Hargreaves BA, Nishimura DG. Design and analysis of a practical 3D cones trajectory. *Magn. Reson. Med.* 2006;55:575–582.

38. Willmering MM, Robison RK, Wang H, Pipe JG, Woods JC. Implementation of the FLORET UTE sequence for lung imaging. *Magn. Reson. Med.* 2019;82:1091–1100.

39. Stobbe RW, Beaulieu C. Three-dimensional Yarnball k-space acquisition for accelerated MRI. *Magn. Reson. Med.* 2021;85:1840–1854.

40. Speidel T, Metze P, Rasche V. Efficient 3D Low-Discrepancy k -Space Sampling Using Highly Adaptable Seiffert Spirals. *IEEE Trans. Med. Imaging* 2019;38:1833–1840.

41. Lazarus C, Weiss P, Chauffert N, et al. SPARKLING: variable-density k-space filling curves for accelerated T2*-weighted MRI. *Magn. Reson. Med.* 2019;81:3643–3661.

42. Sodickson DK, Manning WJ. Simultaneous acquisition of spatial harmonics (SMASH): Fast imaging with radiofrequency coil arrays. *Magn. Reson. Med.* 1997;38:591–603.

43. Pruessmann KP, Weiger M, Scheidegger MB, Boesiger P. SENSE: Sensitivity encoding for fast MRI. *Magn. Reson. Med.* 1999;42:952–962.

44. Griswold MA, Jakob PM, Heidemann RM, et al. Generalized autocalibrating partially parallel acquisitions (GRAPPA). *Magn. Reson. Med.* 2002;47:1202–1210.

45. Lustig M, Pauly JM. SPIRiT: Iterative self-consistent parallel imaging reconstruction from arbitrary k-space. *Magn. Reson. Med.* 2010;64:457–471.

46. Wright KL, Hamilton JI, Griswold MA, Gulani V, Seiberlich N. Non-Cartesian parallel imaging reconstruction. *J. Magn. Reson. Imaging* 2014;40:1022–1040.

47. Pruessmann KP, Weiger M, Börnert P, Boesiger P. Advances in sensitivity encoding with arbitrary *k* -space trajectories: SENSE With Arbitrary *k* -Space Trajectories. *Magn. Reson. Med.* 2001;46:638–651.

48. Fessler JA, Sutton BP. Nonuniform fast Fourier transforms using min-max interpolation. *IEEE Trans. Signal Process.* 2003;51:560–574.

49. Lustig M, Donoho D, Pauly JM. Sparse MRI: The application of compressed sensing for rapid MR imaging. *Magn. Reson. Med.* 2007;58:1182–1195.

50. Murphy M, Alley M, Demmel J, Keutzer K, Vasanawala S, Lustig M. Fast ℓ_1 -SPIRiT Compressed Sensing Parallel Imaging MRI: Scalable Parallel Implementation and Clinically Feasible Runtime. *IEEE Trans. Med. Imaging* 2012;31:1250–1262.

51. Fan L, Shen D, Haji-Valizadeh H, et al. Rapid dealiasing of undersampled, non-Cartesian cardiac perfusion images using U-net. *NMR Biomed.* 2020;33:e4239.

52. Hauptmann A, Arridge S, Lucka F, Muthurangu V, Steeden JA. Real-time cardiovascular MR with spatio-temporal artifact suppression using deep learning–proof of concept in congenital heart disease. *Magn. Reson. Med.* 2019;81:1143–1156.

53. Qin C, Schlemper J, Caballero J, Price AN, Hajnal JV, Rueckert D. Convolutional Recurrent Neural Networks for Dynamic MR Image Reconstruction. *IEEE Trans. Med. Imaging* 2019;38:280–290.

54. Schlemper J, Caballero J, Hajnal JV, Price AN, Rueckert D. A Deep Cascade of Convolutional Neural Networks for Dynamic MR Image Reconstruction. *IEEE Trans. Med. Imaging* 2018;37:491–503.

55. Sandino CM, Lai P, Vasanawala SS, Cheng JY. Accelerating cardiac cine MRI using a deep learning-based ESPIRiT reconstruction. *Magn. Reson. Med.* 2021;85:152–167.

56. Kofler A, Dewey M, Schaeffter T, Wald C, Kolbitsch C. Spatio-Temporal Deep Learning-Based Undersampling Artefact Reduction for 2D Radial Cine MRI With Limited Training Data. *IEEE Trans. Med. Imaging* 2020;39:703–717.

57. Biswas S, Aggarwal HK, Jacob M. Dynamic MRI using model-based deep learning and SToRM priors: MoDL-SToRM. *Magn. Reson. Med.* 2019;82:485–494.

58. Küstner T, Fuin N, Hammernik K, et al. CINENet: deep learning-based 3D cardiac CINE MRI reconstruction with multi-coil complex-valued 4D spatio-temporal convolutions. *Sci. Rep.* 2020;10:13710.

59. Gibbons EK, Tian Y, Huang Q, Chaudhari A, DiBella E. Rapid myocardial perfusion MRI reconstruction using deep learning networks. In: Proceedings of the 28th Annual Meeting of ISMRM, 2020. p 2216.

60. Le J, Tian Y, Mendes J, et al. Deep Learning for Radial Myocardial Perfusion Reconstruction using 3D residual booster U-Nets. In: Proceedings of the 28th Annual Meeting of ISMRM, 2020. p 2095.

61. Ghodrati V, Shao J, Bydder M, et al. MR image reconstruction using deep learning: evaluation of network structure and loss functions. *Quant. Imaging Med. Surg.* 2019;9:1516527–1511527.

62. Yaman B, Shenoy C, Deng Z, et al. Self-Supervised Physics-Guided Deep Learning Reconstruction For High-Resolution 3D LGE CMR. *ArXiv201109414 Eess* 2020.

63. Shen D, Ghosh S, Haji-Valizadeh H, et al. Rapid reconstruction of highly undersampled, non-Cartesian real-time cine k-space data using a perceptual complex neural network (PCNN). *NMR Biomed.* 2021;34:e4405.

64. El-Rewaidy H, Neisius U, Mancio J, et al. Deep complex convolutional network for fast reconstruction of 3D late gadolinium enhancement cardiac MRI. *NMR Biomed.* 2020;33:e4312.

65. Schlemper J, Caballero J, Hajnal JV, Price AN, Rueckert D. A Deep Cascade of Convolutional Neural Networks for Dynamic MR Image Reconstruction. *IEEE Trans. Med. Imaging* 2018;37:491–503.

66. Aggarwal HK, Mani MP, Jacob M. MoDL: Model-Based Deep Learning Architecture for Inverse Problems. *IEEE Trans. Med. Imaging* 2019;38:394–405.

67. Hammernik K, Schlemper J, Qin C, Duan J, Summers RM, Rueckert D. Systematic evaluation of iterative deep neural networks for fast parallel MRI reconstruction with sensitivity-weighted coil combination. *Magn. Reson. Med.* 2021;86:1859–1872.

68. Ahmad R, Bouman CA, Buzzard GT, et al. Plug-and-Play Methods for Magnetic Resonance Imaging: Using Denoisers for Image Recovery. *IEEE Signal Process. Mag.* 2020;37:105–116.

69. Akçakaya M, Moeller S, Weingärtner S, Uğurbil K. Scan-specific robust artificial-neural-networks for k-space interpolation (RAKI) reconstruction: Database-free deep learning for fast imaging. *Magn. Reson. Med.* 2019;81:439–453.

70. Nencka AS, Arpinar VE, Bhave S, et al. Split-slice training and hyperparameter tuning of RAKI networks for simultaneous multi-slice reconstruction. *Magn. Reson. Med.* 2021;85:3272–3280.

71. Barth M, Breuer F, Koopmans PJ, Norris DG, Poser BA. Simultaneous multislice (SMS) imaging techniques: SMS Imaging. *Magn. Reson. Med.* 2016;75:63–81.

72. Souza SP, Szumowski J, Dumoulin CL, Plewes DP, Glover G. SIMA: simultaneous multislice acquisition of MR images by Hadamard-encoded excitation. *J. Comput. Assist. Tomogr.* 1988;12:1026–1030.

73. Breuer FA, Blaimer M, Heidemann RM, Mueller MF, Griswold MA, Jakob PM. Controlled aliasing in parallel imaging results in higher acceleration (CAIPIRINHA) for multi-slice imaging. *Magn. Reson. Med.* 2005;53:684–691.

74. Setsompop K, Gagoski BA, Polimeni JR, Witzel T, Wedeen VJ, Wald LL. Blipped-controlled aliasing in parallel imaging for simultaneous multislice echo planar imaging with reduced g-factor penalty. *Magn. Reson. Med.* 2012;67:1210–1224.

75. Lee VS. Cardiovascular MRI: Physical Principles to Practical Protocols. *Lippincott Williams & Wilkins*; 2006.

76. Messroghli DR, Radjenovic A, Kozerke S, Higgins DM, Sivananthan MU, Ridgway JP. Modified Look-Locker inversion recovery (MOLLI) for high-resolution T1 mapping of the heart. *Magn. Reson. Med.* 2004;52:141–146.

77. Chow K, Flewitt JA, Green JD, Pagano JJ, Friedrich MG, Thompson RB. Saturation recovery single-shot acquisition (SASHA) for myocardial T(1) mapping. *Magn. Reson. Med.* 2014;71:2082–2095.

78. Shaw LJ, Merz CNB, Pepine CJ, et al. The Economic Burden of Angina in Women With Suspected Ischemic Heart Disease: Results From the National Institutes of Health–National Heart, Lung, and Blood Institute–Sponsored Women's Ischemia Syndrome Evaluation. *Circulation* 2006;114:894–904.

79. CDC. Coronary Artery Disease | cdc.gov. Centers for Disease Control and Prevention. https://www.cdc.gov/heartdisease/coronary_ad.htm. Published July 19, 2021. Accessed August 6, 2022.

80. Patel MR, Peterson ED, Dai D, et al. Low Diagnostic Yield of Elective Coronary Angiography. *N. Engl. J. Med.* 2010;362:886–895.

81. Yang Y. Whole-heart Coverage Quantitative First-pass Spiral Perfusion in Cardiac Magnetic Resonance Imaging. *University of Virginia*; 2016.

82. Takx RAP, Blomberg BA, El Aidi H, et al. Diagnostic accuracy of stress myocardial perfusion imaging compared to invasive coronary angiography with fractional flow reserve meta-analysis. *Circ. Cardiovasc. Imaging* 2015;8:e002666.

83. Nagel E, Greenwood JP, McCann GP, et al. Magnetic Resonance Perfusion or Fractional Flow Reserve in Coronary Disease. *N. Engl. J. Med.* 2019;380:2418–2428.

84. Shaw P, Yang Y, Li Y, et al. High resolution CMR perfusion imaging demonstrates reduced flow reserve and endo/epi ratio in microvascular coronary disease. *J. Cardiovasc. Magn. Reson.* 2015;17:P148.

85. Cerqueira MD, Weissman NJ, Dilsizian V, et al. Standardized Myocardial Segmentation and Nomenclature for Tomographic Imaging of the Heart. *Circulation* 2002;105:539–542.

86. Gerber BL, Raman SV, Nayak K, et al. Myocardial first-pass perfusion cardiovascular magnetic resonance: history, theory, and current state of the art. *J. Cardiovasc. Magn. Reson.* 2008;10:18.

87. Jerosch-Herold M. Quantification of myocardial perfusion by cardiovascular magnetic resonance. *J. Cardiovasc. Magn. Reson.* 2010;12:57.

88. Greenwood JP, Maredia N, Younger JF, et al. Cardiovascular magnetic resonance and single-photon emission computed tomography for diagnosis of coronary heart disease (CE-MARC): a prospective trial. *The Lancet* 2012;379:453–460.

89. Shah R, Heydari B, Coelho-Filho O, et al. Stress Cardiac Magnetic Resonance Imaging Provides Effective Cardiac Risk Reclassification in Patients With Known or Suspected Stable Coronary Artery Disease. *Circulation* 2013;128:605–614.

90. Camici PG, Rimoldi OE. The Clinical Value of Myocardial Blood Flow Measurement. *J. Nucl. Med.* 2009;50:1076–1087.

91. Lee DC, Johnson NP. Quantification of Absolute Myocardial Blood Flow by Magnetic Resonance Perfusion Imaging. *JACC Cardiovasc. Imaging* 2009;2:761–770.

92. Wang L, Jerosch-Herold M, Jacobs DR, Shahar E, Detrano R, Folsom AR. Coronary Artery Calcification and Myocardial Perfusion in Asymptomatic Adults: The MESA (Multi-Ethnic Study of Atherosclerosis). *J. Am. Coll. Cardiol.* 2006;48:1018–1026.

93. Patel AR, Antkowiak PF, Nandalur KR, et al. Assessment of Advanced Coronary Artery Disease: Advantages of Quantitative Cardiac Magnetic Resonance Perfusion Analysis. *J. Am. Coll. Cardiol.* 2010;56:561–569.

94. Salerno M, Sica CT, Kramer CM, Meyer CH. Optimization of spiral-based pulse sequences for first-pass myocardial perfusion imaging. *Magn. Reson. Med.* 2011;65:1602–1610.

95. Salerno M, Sica C, Kramer CM, Meyer CH. Improved first-pass spiral myocardial perfusion imaging with variable density trajectories: Variable Density Spiral Myocardial Perfusion Imaging. *Magn. Reson. Med.* 2013;70:1369–1379.

96. Adluru G, McGann C, Speier P, Kholmovski EG, Shaaban A, DiBella EVR. Acquisition and reconstruction of undersampled radial data for myocardial perfusion magnetic resonance imaging. *J. Magn. Reson. Imaging* 2009;29:466–473.

97. Sharif B, Dharmakumar R, LaBounty T, et al. Towards elimination of the dark-rim artifact in first-pass myocardial perfusion MRI: Removing Gibbs ringing effects using optimized radial imaging. *Magn. Reson. Med.* 2014;72:124–136.

98. Fair MJ, Gatehouse PD, DiBella EVR, Firmin DN. A review of 3D first-pass, whole-heart, myocardial perfusion cardiovascular magnetic resonance. *J. Cardiovasc. Magn. Reson.* 2015;17:68.

99. Wang H, Adluru G, Chen L, Kholmovski EG, Bangerter NK, DiBella EVR. Radial simultaneous multi-slice CAIPI for ungated myocardial perfusion. *Magn. Reson. Imaging* 2016;34:1329–1336.

100. Tian Y, Mendes J, Wilson B, et al. Whole-heart, ungated, free-breathing, cardiac-phase-resolved myocardial perfusion MRI by using Continuous Radial Interleaved simultaneous Multi-slice acquisitions at sPoiled steady-state (CRIMP). *Magn. Reson. Med.* 2020;84:3071–3087.

101. Stäb D, Wech T, Breuer FA, et al. High resolution myocardial first-pass perfusion imaging with extended anatomic coverage. *J. Magn. Reson. Imaging* 2014;39:1575–1587.

102. Sharif B, Dharmakumar R, Arsanjani R, et al. Non–ECG-gated myocardial perfusion MRI using continuous magnetization-driven radial sampling. *Magn. Reson. Med.* 2014;72:1620–1628.

103. Naresh NK, Haji-Valizadeh H, Aouad PJ, et al. Accelerated, first-pass cardiac perfusion pulse sequence with radial k-space sampling, compressed sensing, and k-space weighted image contrast reconstruction tailored for visual analysis and quantification of myocardial blood flow. *Magn. Reson. Med.* 2019;81:2632–2643.

104. McElroy S, Ferrazzi G, Nazir MS, et al. Combined simultaneous multislice bSSFP and compressed sensing for first-pass myocardial perfusion at 1.5 T with high spatial resolution and coverage. *Magn. Reson. Med.* 2020;84:3103–3116.

105. Bella EVRD, Parker DL, Sinusas AJ. On the dark rim artifact in dynamic contrast-enhanced MRI myocardial perfusion studies. *Magn. Reson. Med.* 2005;54:1295–1299.

106. Cauley SF, Polimeni JR, Bhat H, Wald LL, Setsompop K. Interslice leakage artifact reduction technique for simultaneous multislice acquisitions. *Magn. Reson. Med.* 2014;72:93–102.

107. Wang J, Yang Y, Zhou R, Jacob M, Weller DS, Salerno M. SMS Slice L1-SPIRiT: auto-calibrated image reconstruction for spiral simultaneous multi-slice first-pass perfusion imaging with 1.25 mm resolution and whole heart coverage at 3T. In: Proceedings of the SCMR 23rd Annual Scientific Sessions, Orlando, Florida, USA, 2020. Abstract 714001.

108. Sun C, Yang Y, Cai X, et al. Non-Cartesian slice-GRAPPA and slice-SPIRiT reconstruction methods for multiband spiral cardiac MRI. *Magn. Reson. Med.* 2020;83:1235–1249.

109. Gottbrecht M, Kramer CM, Salerno M. Native T1 and Extracellular Volume Measurements by Cardiac MRI in Healthy Adults: A Meta-Analysis. *Radiology* 2018;290:317–326.

110. Kanal E, Maravilla K, Rowley HA. Gadolinium Contrast Agents for CNS Imaging: Current Concepts and Clinical Evidence. *Am. J. Neuroradiol.* 2014;35:2215–2226.

111. Yang Y, Meyer C, Epstein F, Kramer C, Salerno M. Single-shot spiral first-pass perfusion imaging: full heart coverage with high temporal resolution. In: Proceedings of the 21st Annual Meeting of ISMRM, Salt Lake City, Utah, USA, 2013. p 4556.

112. Yang Y, Robinson A, Mathew R, Kramer C, Salerno M. Optimization of 3T ultra-high resolution first-pass spiral perfusion imaging. In: Proceedings of the SCMR 22nd Annual Scientific Sessions, Bellevue, Washington, USA, 2019. Abstract 549312.

113. Chow K, Kellman P, Spottiswoode BS, et al. Saturation pulse design for quantitative myocardial T1 mapping. *J. Cardiovasc. Magn. Reson.* 2015;17:84.

114. Zhou R, Huang W, Yang Y, et al. Simple motion correction strategy reduces respiratory-induced motion artifacts for k-t accelerated and compressed-sensing cardiovascular magnetic resonance perfusion imaging. *J. Cardiovasc. Magn. Reson.* 2018;20:6.

115. Scannell CM, Villa ADM, Lee J, Breeuwer M, Chiribiri A. Robust Non-Rigid Motion Compensation of Free-Breathing Myocardial Perfusion MRI Data. *IEEE Trans. Med. Imaging* 2019;38:1812–1820.

116. Feng L, Grimm R, Block KT, et al. Golden-angle radial sparse parallel MRI: Combination of compressed sensing, parallel imaging, and golden-angle radial sampling for fast and flexible dynamic volumetric MRI. *Magn. Reson. Med.* 2014;72:707–717.

117. Weller DS, Ramani S, Fessler JA. Augmented Lagrangian with Variable Splitting for Faster Non-Cartesian L1-SPIRiT MR Image Reconstruction. *IEEE Trans. Med. Imaging* 2014;33:351–361.

118. Zhang T, Pauly JM, Vasanawala SS, Lustig M. Coil compression for accelerated imaging with Cartesian sampling. *Magn. Reson. Med.* 2013;69:571–582.

119. Noll DC, Pauly JM, Meyer CH, Nishimura DG, Macovskj A. Deblurring for non-2D fourier transform magnetic resonance imaging. *Magn. Reson. Med.* 1992;25:319–333.

120. Walsh DO, Gmitro AF, Marcellin MW. Adaptive reconstruction of phased array MR imagery. *Magn. Reson. Med.* 2000;43:682–690.

121. Zhou Wang, Bovik AC, Sheikh HR, Simoncelli EP. Image quality assessment: from error visibility to structural similarity. *IEEE Trans. Image Process.* 2004;13:600–612.

122. Bush MA, Ahmad R, Jin N, Liu Y, Simonetti OP. Patient specific prospective respiratory motion correction for efficient, free-breathing cardiovascular MRI. *Magn. Reson. Med.* 2019;81:3662–3674.

123. Lu W, Pauly KB, Gold GE, Pauly JM, Hargreaves BA. SEMAC: Slice encoding for metal artifact correction in MRI. *Magn. Reson. Med.* 2009;62:66–76.

124. Demirel OB, Weingärtner S, Moeller S, Akçakaya M. Multi-Band SPIRiT Strategies for Improved Simultaneous Multi-slice Myocardial T1 Mapping. In: Proceedings of the 27th Annual Meeting of ISMRM, Montréal, QC, Canada, 2019. p 2126.

125. Yang Y, Kramer C, Salerno M. Whole heart First-pass spiral perfusion imaging with 1.25mm resolution at 3T. In: Proceedings of the 26th Annual Meeting of ISMRM, Paris, France, 2018. p 3321.

126. Wang J, Yang Y, Zhou R, et al. High resolution spiral simultaneous multi-slice first-pass perfusion imaging with whole-heart coverage at 1.5 T and 3 T. In: Proceedings of the 28th Annual Meeting of ISMRM, 2020. p 1313.

127. Çiçek Ö, Abdulkadir A, Lienkamp SS, Brox T, Ronneberger O. 3D U-Net: Learning Dense Volumetric Segmentation from Sparse Annotation. *ArXiv160606650 Cs* 2016.

128. Ronneberger O, Fischer P, Brox T. U-Net: Convolutional Networks for Biomedical Image Segmentation. In: Navab N, Hornegger J, Wells WM, Frangi AF, editors. Medical Image Computing and Computer-Assisted Intervention – MICCAI 2015. Cham: *Springer International Publishing*; 2015. pp. 234–241.

129. Hammernik K, Schlemper J, Qin C, Duan J, Summers RM, Rueckert D. Σ-net: Systematic Evaluation of Iterative Deep Neural Networks for Fast Parallel MR Image Reconstruction. *ArXiv191209278 Cs Eess* 2019.

130. Zhou R, Huang W, Yang Y, et al. Simple motion correction strategy reduces respiratory-induced motion artifacts for k-t accelerated and compressed-sensing cardiovascular magnetic resonance perfusion imaging. *J. Cardiovasc. Magn. Reson.* 2018;20.

131. Demirel ÖB, Weingärtner S, Moeller S, Akçakaya M. Improved Regularized Reconstruction for Simultaneous Multi-Slice Cardiac MRI T1 Mapping. In: 2019 27th European Signal Processing Conference (EUSIPCO). ; 2019. pp. 1–5.

132. Demirel ÖB, Weingärtner S, Moeller S, Akçakaya M. Improved Simultaneous Multi-Slice Imaging for Perfusion Cardiac MRI Using Outer Volume Suppression and Regularized Reconstruction. In: 2020 IEEE 17th International Symposium on Biomedical Imaging (ISBI). ; 2020. pp. 1954–1957.

133. Knoll F, Schwarzl A, Diwoky C, Sodickson D. gpuNUFFT - An Open-Source GPU Library for 3D Gridding with Direct Matlab Interface. In: Proceedings of the 23th Annual Meeting of ISMRM, Milan, Italy, 2014. p 4297.

134. Wang J, Weller D, Salerno M. DESIRE: DEep learning-based rapid Spiral Image REconstruction for high-resolution spiral first-pass myocardial perfusion imaging with whole-heart coverage. In: Proceedings of the SCMR 24th Annual Scientific Sessions. 2021.

135. Walsh DO, Gmitro AF, Marcellin MW. Adaptive reconstruction of phased array MR imagery. *Magn. Reson. Med.* 2000;43:682–690.

136. Cole E, Pauly J, Vasanawala S, Cheng J. Complex-Valued Convolutional Neural Networks for MRI Reconstruction. In: Proceedings of the 27th Annual Meeting of ISMRM, Montréal, QC, Canada, 2019. p 4714.

137. Cole E, Cheng J, Pauly J, Vasanawala S. Analysis of deep complex-valued convolutional neural networks for MRI reconstruction and phase-focused applications. *Magn. Reson. Med.* 2021;00:1–17.

138. Tran D, Wang H, Torresani L, Ray J, LeCun Y, Paluri M. A Closer Look at Spatiotemporal Convolutions for Action Recognition. In: 2018 IEEE/CVF Conference on Computer Vision and Pattern Recognition. Salt Lake City, UT: *IEEE*; 2018. pp. 6450–6459.

139. Zhao H, Gallo O, Frosio I, Kautz J. Loss Functions for Image Restoration With Neural Networks. *IEEE Trans. Comput. Imaging* 2017;3:47–57.

140. Kellman P, Hansen MS, Nielles-Vallespin S, et al. Myocardial perfusion cardiovascular magnetic resonance: optimized dual sequence and reconstruction for quantification. *J. Cardiovasc. Magn. Reson.* 2017;19:43.

141. McElroy S, Ferrazzi G, Nazir MS, et al. Combined simultaneous multislice bSSFP and compressed sensing for first-pass myocardial perfusion at 1.5 T with high spatial resolution and coverage. *Magn. Reson. Med.* 2020;84:3103–3116.

142. Yaman B, Hosseini SAH, Moeller S, Ellermann J, Uğurbil K, Akçakaya M. Self-supervised learning of physics-guided reconstruction neural networks without fully sampled reference data. *Magn. Reson. Med.* 2020;84:3172–3191.

143. Chen X, Salerno M, Yang Y, Epstein FH. Motion-compensated compressed sensing for dynamic contrast-enhanced MRI using regional spatiotemporal sparsity and region tracking: Block low-rank sparsity with motion-guidance (BLOSM): BLOSM: Block Low-rank Sparsity with Motion-guidance. *Magn. Reson. Med.* 2014;72:1028–1038.

144. Feng L, Srichai MB, Lim RP, et al. Highly accelerated real-time cardiac cine MRI using k–t SPARSE-SENSE. *Magn. Reson. Med.* 2013;70:64–74.

145. Cole E, Cheng J, Pauly J, Vasanawala S. Analysis of deep complex-valued convolutional neural networks for MRI reconstruction and phase-focused applications. *Magn. Reson. Med.* 2021;86:1093–1109.

146. Xue H, Davies RH, Brown LAE, et al. Automated Inline Analysis of Myocardial Perfusion MRI with Deep Learning. *Radiol. Artif. Intell.* 2020;2:e200009.

147. Scannell CM, Veta M, Villa ADM, et al. Deep-Learning-Based Preprocessing for Quantitative Myocardial Perfusion MRI. *J. Magn. Reson. Imaging* 2020;51:1689–1696.